

POLITECNICO DI TORINO

Corso di Laurea Magistrale in Ingegneria Energetica e
Nucleare



ASSESSMENT OF OPTICAL PERFORMANCE OF A COMPACT LINEAR FRESNEL COLLECTOR IN THE BUILT-ENVIRONMENT.

Relatori:

Prof. Massimo Santarelli

Dr/Eng. Alaric Christian Montenon

Candidato:

Roberto Garofalo

S257784

Anno Accademico 2020/2021

Ai miei genitori Anna e Filippo

Abstract

In this thesis a Linear Fresnel Reflector (LFR), one of the major concentrating solar technologies, is studied from the energetic and optic points of view. Generally speaking, the Concentrated Solar Technologies (CST) systems are of particular interest in sunny regions of the world for both electricity generation and heat processing. More specifically, the thesis examines the LFR installed at the Cyprus Institute (Nicosia, Cyprus), using Ray tracing and Flux Analysis software tools to evaluate its behaviour and performance. The study is divided into 7 major sections:

- ***Introduction:*** The study starts by analysing the meaning of sustainability and its outcomes on energy transition following the implementation of new technologies able to develop a natural equilibrium between the emission of Greenhouse gases (GHGs) by human settlements or activities and their absorption by natural and artificial sinks. Starting from a description of the European Commission's environment and energy policies (*2020 Climate & Energy Package, 2030 Climate & Energy Framework and European Green Deal*), the energy situation in Cyprus is then outlined, showing the different energy indicators of Total Primary Energy Supply (TPES), Total Final Consumption (TFC) and Energy Intensity and emphasizing on the electricity production and energy imports into the island.
- ***Solar Energy:*** The second part of the thesis considers the Solar Energy as a renewable energy source. After describing its main characteristics, the advantages and disadvantages of its exploitation are considered. The major solar technologies are described highlighting their differences based on the type of energy produced (electricity or thermal energy).
- ***Concentrating Solar Technologies:*** The third chapter of the thesis introduces the Concentrating Solar Technologies, considering their general characteristics in terms of energy efficiency and the sites where they could be installed. Then the main differences between CST and photovoltaic systems (PV) are set out. A comparison between the several types of

concentrating solar systems – the Parabolic Trough Collector (PTC), Solar Power Tower (SPT) and Solar Parabolic Dish (SPD) – is made, taking into account their specificity.

- ***Linear Fresnel Reflector:*** The fourth chapter opens with a description of the characteristics of the Linear Fresnel Reflector (LFR) plant, which is the principal focus of the study. Its main applications are discussed here considering its power and heat generation purposes. The plant installed at The Cyprus Institute is presented technically afterwards. The principal components of the LFR (*Primary Reflector, Tracking System and Receiver*) are presented along with their functions and their composition. Thanks to the energy equation concerning the thermal behaviour of the receiver, the Incidence Angle Modifier (IAM), which is the final objective of the thesis, is introduced. Two plants based on LFR (*Existing plant and LFR with Non-Imaging Optics NIO*) are introduced for the study of their optical performance.
- ***Direct Solar Energy in Nicosia:*** The fifth chapter of the thesis outlines the incoming solar energy received at the Cyprus Institute based on data measured thanks to a locally installed pyrheliometer. DNI plots from three different days (Summer Solstice, Winter Solstice and Autumn Equinox) are exposed highlighting the duration of the days and the energy balance. In addition, the daily average solar energy month by month is represented.
- ***Method to compute IAM values using Tonatiuh:*** The sixth chapter is the core of the thesis, introducing the methodology used to calculate the Incidence Angle Modifier (IAM) of the two plants by considering the large set of sun positions defined by the azimuth and elevation angles. Considering as input the DNI registered over the previous years reported in the previous fifth chapter, the collectable energy from the LFR plants is evaluated with Matlab and represented also taking into account the optical performance of the plants expressed by the IAM in order to compare them in terms of energy.
- ***Flux Analysis Distribution:*** In the seventh and last chapter of the thesis, flux analyses in the receiver are carried out for the two different plants. After

a short description of the methodology underpinning Tonatiuh software, flux analyses are performed for three different positions of the sun in order to understand how the solar power is distributed on the absorber surface. The major differences between the two plants according to the flux analysis are highlighted to extract the best flux distribution.

INDEX

Abstract.....	3
<i>Index of figures</i>	9
1. Introduction	14
1.1 Sustainability	14
1.2 European Energy Strategy	15
1.2.1 2020 climate & energy package	15
1.2.2 2030 climate & energy framework	16
1.2.3 European Green Deal	17
1.3 Energy Balance of the Republic of Cyprus	17
2. Solar Energy	26
2.1 Solar Technologies	27
2.1.1 Solar Thermal Technology	28
2.1.2 Solar Power Technology	28
3. Concentrating Solar Technologies	30
3.1 Types of CSP systems	32
3.1.1 Parabolic Trough Collector	34
3.1.2 Solar Power-Tower (SPT) / Central Receiver	35
3.1.3 Solar Parabolic Dish (SPD) System	38
4. Linear Fresnel Reflector	40
4.1 LFR Main Applications.	40
4.1.1 Power Generation Applications	41
4.1.2 Thermal Applications	41
4.1.3 Linear Fresnel facility at Cyprus Institute	42
4.2 Components of an LFR	44
4.2.1 Primary Reflector	45
4.2.2 Tracking system	49

4.2.3	<i>Receiver</i>	50
4.3	<i>Plants modelled within Tonatiuh</i>	52
4.3.1	<i>Existing LFR Plant</i>	52
4.3.2	<i>LFR Plant with Non-imaging Optics</i>	54
5.	<i>Direct Solar Energy in Nicosia</i>	57
5.1	<i>Solar Energy Measurement</i>	57
6.	<i>Method to compute IAM values using Tonatiuh++</i>	61
6.1	<i>Incidence Angle Modifiers</i>	61
6.2	<i>The Tonatiuh++ Process</i>	62
6.2.1	<i>Ray Tracing Analysis for the Existing LFR plant (ASB).</i>	64
6.2.2	<i>Ray Tracing Analysis for the improved LFR plant with NIO.</i>	65
6.3	<i>Matlab Processing</i>	66
6.4	<i>Results of the IAM Analysis.</i>	67
6.4.1	<i>IAMs and Energy received by the existing LFR plant (ASB)</i>	67
6.4.2	<i>IAMs and Energy received by the upgraded LFR plant (NIO)</i>	71
6.4.3	<i>IAMs and Energy received by the improved LFR plant with insertion of glass surface in the aperture of the receiver.</i>	74
7.	<i>Flux Analysis</i>	79
7.1	<i>Description of the Flux Analysis tool</i>	79
7.2	<i>Convergence Analysis</i>	80
7.2.1	<i>Convergence Analysis on ASB plant.</i>	80
7.2.2	<i>Convergence Analysis on NIO plant.</i>	83
7.3	<i>Flux Analysis in existing LFR plant.</i>	84
7.4	<i>Flux Analysis in existing LFR plant without Glass pipes.</i>	87
7.5	<i>Flux Analysis with Non-imaging Optics.</i>	89
8.	<i>Conclusions</i>	91
	<i>Bibliography</i>	93
	<i>Appendix</i>	97

1. Description of Tonatiuh	97
2. Description of the design of the Fresnel Facility	99
2.1 Receiver	100
2.2 Structure	107
2.3 Primary Reflector	111
3. Environment Settings	113
4. Ray Tracing Simulations	114
5. Script Tool	115
5.1 Definition of position and construction function for each component	116
5.2 Construction of the CYI Fresnel	119
5.3 Scene Settings	122
6. Matlab Scripts	123
6.1 DNI Energy Yearly Plot	123
6.2 DNI Power Plot	129
Ringraziamenti	130

Index of figures

Figure 1: Cyprus' TPES [ktoe] [10].....	19
Figure 2: Cyprus' TFC by sector [ktoe] [10].....	20
Figure 3: Cyprus' TFC by source [ktoe] [10].....	20
Figure 4: Cyprus' Net Imports [10].....	21
Figure 5: Imports and Exports of Oil in Cyprus [10].....	21
Figure 6: Electricity production by fuel in Cyprus [GWh] [10].....	22
Figure 7: Low-carbon electricity generation by source in Cyprus [GWh] [10].....	23
Figure 8: Cyprus' Energy Intensity [MJ/\$2011] [14].....	24
Figure 9: Cyprus' GDP (current US\$) [14].....	24
Figure 10: Cyprus' Energy Trilemma [15].....	25
Figure 11: Performances in the three core dimensions of the Energy Trilemma [15].	25
Figure 12: How the Solar Energy reaches the Earth's Surface [16].....	26
Figure 13: Solar spectrum [17].....	27
Figure 14: World's DNI map [18].....	31
Figure 15: Cyprus' DNI map [18].....	31
Figure 16: Schematic representation of light concentration process [20].....	33
Figure 17: Parabolic Trough Collector [22].....	34
Figure 18: Example of a Steam Solar Power Tower [22].....	35
Figure 19: Solar Power Tower [22].....	36
Figure 20: Schematic representation of the energy flow in PFF [25].....	37
Figure 21: Structure of PFF's Cogeneration Power Plant. (1) Heliostat Field, (2) Receiver, (3) Thermal Energy Storage, (4) Rankine Cycle and (5) MED desalination unit [25].....	38
Figure 22: SG4 system [26].....	38
Figure 23: Example of LFR [27].....	40
Figure 24: Dunhuang Dacheng 50 MW Molten Salt LFR [29].....	41
Figure 25: LFR plant installed in Sardinia for Heat processing for a cheese industry [33].....	41
Figure 26: LFR plant installed in Johannesburg for cooling purposes [34].....	42
Figure 27: LFR placed at The Cyprus Institute [36].....	42
Figure 28: Layout of the entire process placed at The Cyprus Institute [36].....	43
Figure 29: How a tracking system of LFR works [38].....	44

Figure 30: Parabolical Mirror vs Fresnel Mirror [28].....	45
Figure 31: Optical losses of the mirror [28].....	46
Figure 32: Longitudinal and transversal axis of a LFR [28].....	47
Figure 33: Difference in the actions of a perfect mirror against to an imperfect one [28].....	47
Figure 34: Costs per kWe produced as a function of the number of rows [39].....	48
Figure 35: Costs per kWe produced as a function of the gap between rows [39].	49
Figure 36: Costs per kWe as a function of the ratio between Focus Length of the mirrors composing a row and its distance from the receiver [39].....	49
Figure 37: Possible solutions of a tracking system in a LFR plant [28].....	50
Figure 38: Two possible shape of Secondary Optic [28].....	51
Figure 39: How a vacuum glass tube behaves in terms of heat transfer [28].....	51
Figure 40: Existing LFR plant created using Tonatiuh viewed from the South.	53
Figure 41: Receiver of the existing LFR plant.....	54
Figure 42: Improved Receiver with Non-imaging Optics.	55
Figure 43: LFR plant with optimized receiver with non-Imaging Optics viewed from the South.	56
Figure 44: LP Pyrheliometer 16 AC placed at The Cyprus Institute.....	58
Figure 45: DNI plotted during Summer Solstice, Winter Solstice and Autumn Equinox.	58
Figure 46: Daily Solar Energy at The Cyprus Institute.	59
Figure 47: Average Daily Solar Energy per month at the Cyprus Institute.....	59
Figure 48: Representation of how the sun position could be expressed.....	61
Figure 49: General view of the LFR at CyI with Tonatiuh++ with solar Azimuth of 60° and Elevation of 45°.	63
Figure 50: Script run for achieving the optical efficiency of LFR at zenith.	64
Figure 51: Second Part of the Script run for achieving the IAM.	64
Figure 52: Script run for achieving the optical efficiency and the IAM for the improved LFR plant.	66
Figure 53: IAM values depending on longitudinal and transversal angle for the existing LFR plant.....	68
Figure 54: Transversal and Longitudinal IAM for ASB plant.....	68
Figure 55: DNI available by day vs Energy collected by the Receiver of the existing LFR by day.....	69
Figure 56: Daily average available and collectable energies (left axis) and	

corresponding optical efficiency of the existing LFR (right axis).....	70
Figure 57: IAM values depending on longitudinal and transversal angles for the upgraded LFR plant.	71
Figure 58: Difference between the IAM achieved with the NIO plant compared to the existing plant.	72
Figure 59: Daily average available and collectable energy (left axis) and optical efficiency of the upgraded LFR (right axis).....	73
Figure 60: DNI available by day vs Energy collected by the Receiver of the improved LFR by day.....	73
Figure 61: Modification of the improved LFR with NIO with the glass surface in the aperture.....	74
Figure 62: Difference of the IAM values depending on longitudinal and transversal angle between the two different NIO plants weighted by optical efficiency at zenith.	75
Figure 63: IAM values depending on longitudinal and transversal angle for the upgraded LFR plant (NIO) with glass surface at the aperture.	75
Figure 64: DNI available by day vs Energy collected by the Receiver of the LFR improved with glass by day.....	76
Figure 65: Daily average available and collectable energy and corresponding optical efficiency of the improved LFR with glass.....	77
Figure 66: Daily Average Solar Energy Comparison between the three plants.....	78
Figure 67: Flux Analysis Parameters view for the existing LFR plant.....	80
Figure 68: Flux Distribution at 90°, 60° and 30° of elevation.	85
Figure 69: Power Received by the absorber by varying the Elevation angle and fixing the Azimuth angle.	86
Figure 70: Flux Distribution without Glass pipes at 90°, 60° and 30° of Elevation. .	87
Figure 71: Flux distribution for the two absorbers of the LFR plant with NIOs. The top figure is at 90° of elevation, the middle is at 60° and the bottom one is at 30°....	89
Figure 72: Comparison Flux Distribution of the two plants.....	90
Figure 73: Tonatiuh Main Interface.....	97
Figure 74: Mirror tree composition.	98
Figure 75: LFR Tree.....	99
Figure 76: Receiver Tree.....	99
Figure 77: Structure Tree.	99
Figure 78: Receiver Parameters.	100

Figure 79: Absorber Node.....	100
Figure 80: Absorber Shape.	101
Figure 81: Absorber Parameters.....	101
Figure 82: Glass Pipe Parameters.	101
Figure 83: Glass Pipes Tree.....	101
Figure 84: Glass Pipes Node.....	101
Figure 85: Inner Parameters.....	102
Figure 86: Outer Parameters.....	102
Figure 87: Inner/Outer Glass Pipe Shape.....	102
Figure 88: Connections Node.....	102
Figure 89: Connections Tree.....	103
Figure 90: Outer Shape.	103
Figure 91: Seal Shape.	103
Figure 92: Seal Parameters.	103
Figure 93: Outer Parameters.....	103
Figure 94: Secondary Reflector Parameters.	104
Figure 95: Secondary Optic Pattern with its equation of the fourth order.	104
Figure 96: Secondary Reflector Node.	104
Figure 97: Mirror Parameters.....	105
Figure 98: Mirror Shape.	105
Figure 99: Cover Tree.	106
Figure 100: Cover Parameters.....	106
Figure 101: Top Rectangle Shape.....	106
Figure 102: East Rectangle Parameters.....	106
Figure 103: East/West Rectangle Shape.	107
Figure 104: East Edge Parameters.....	107
Figure 105: Structure Tree.	107
Figure 106: Inlet/Outlet Node.....	108
Figure 107: Part1 Node.	108
Figure 108: Part1 Parameters.....	108
Figure 109: Part1 Shape.....	108
Figure 110: Part2 Node.	109
Figure 111: Part2 Parameters.....	109
Figure 112: Part3 Node.	109
Figure 113: Part3 Parameters.....	109

Figure 114: West Beams Node.	110
Figure 115: Beams Node.	110
Figure 116: Motor Boxes Node.	111
Figure 117: Primary Reflector Node.	111
Figure 118: Primary Reflector Tree.	111
Figure 119: Tracker Setting Parameters.	112
Figure 120: Shape Parameters of the mirrors.	112
Figure 121: World Tree.	113
Figure 122: Sun Parameters.	113
Figure 123: Disabled Nodes.	113
Figure 124: Ray Tracing Setting (1).	114
Figure 125: Ray Tracing Setting (2).	114
Figure 126: Position and material script part for CYI LFR facility.	116
Figure 127: Mirror Function.	117
Figure 128: Flange Function.	117
Figure 129: Pipe Function.	118
Figure 130: Outlet/Inlet Function.	118
Figure 131: Motor Boxes, Inlet, Outlet and Primary Reflector Node.	119
Figure 132: Receiver and Absorber Nodes.	120
Figure 133: Glass Pipes and Connections Nodes.	120
Figure 134: Cover Node.	121
Figure 135: Secondary Reflector Node.	121
Figure 136: West and West Edge Nodes.	122
Figure 137: Beams Node.	122

1. Introduction

1.1 Sustainability

One of the greatest challenges facing humanity in the 21st Century is the need to supply reliable sustainable energy, which can be defined as an energy source that "meets the needs of the present without compromising the ability of future generations to meet their own needs" [1]. The sustainability is the solution to world-wide Climate Change, resulting from Greenhouse gas emission, which has led to an unstoppable increase in the global average temperature, triggering a series of catastrophic environmental events. In response, the nations of the world have accepted to act together within the United Nations Framework Convention on Climate Change (UNFCCC). Within the egis of the UNFCCC, the Paris Agreement was developed in 2015 with the goal of keeping the increase in global average temperatures to well below 2 °C above pre-industrial levels and of pursuing efforts to limit the increase to 1.5 °C. This target can be achieved, as discussed within the agreement, by striking a balance between cutting back anthropogenic emissions at their sources and removing the greenhouse gases via sinks by adopting three different behaviours: Adaptation to the adverse impacts of climate change, Mitigation efforts with the development and deployment of low carbon energy technology and the creation of "finance flows consistent with a pathway towards low greenhouse gas emissions and climate-resilient development". The definition of sustainability appeared for the first time in 1987 in the book "Our Common Future", produced by the World Commission on Environment and Development, which set out four key elements of sustainability regarding the energy world:

- Ability to increase the energy supply in order to satisfy growing human needs.
- Energy Efficiency.
- Public Health and Safety.

- Protection of the biosphere.

The single path that can be pursued in order to meet the sustainability challenge is that of energy transition: in brief, the transformation of the energy system from fossil based to zero carbon. In this scenario, the renewable energies play a significant role.

1.2 European Energy Strategy

The European Energy Strategy can be summarized by considering three different policies: 2020 Climate & Energy Package, 2030 Climate & Energy Framework and the European Green Deal [2].

1.2.1 2020 climate & energy package

The 2020 Climate & Energy Package is a collection of laws introduced in order to guarantee the achievement of Energy and Climate Targets for the European Union. It aims to reach three different goals:

- 20% of reduction of emission of CO₂ (from 1990 levels).
- 20% of EU energy from renewables.
- 20% improvement in energy efficiency.

These targets were fixed by EU leaders in 2007 but adopted in legislation only in 2009. The achievement of those targets is designed to increase EU energy security and generate jobs in the green energy sector. To do so, different tools are necessary:

1. Emissions trading system (ETS): the world's first major carbon market. It aims to limit emissions from more than 11,000 heavy energy-using installations and airlines operating between EU countries. Covering around 45% of the EU's greenhouse gas emissions, EU ETS works with the "Cap and Trade" principle. A "cap" or maximum amount is fixed on greenhouse gases emissions for each installation of a defined system. This threshold is decreased over time to reduce emissions. In order to comply with the threshold, companies "trade" i.e. receive or buy emission allowances. In the case of non-compliance, hefty economic sanctions are inflicted.

2. National emission reduction targets: Covering the sectors that are not included in ETS (i.e. Housing, Agriculture, Transport and Waste disposal), the EU Commission fixed until 2020 the carbon emission limits for each country that must not be surpassed.
3. Renewable energy: National targets for the share of Renewables are set for the different EU countries. The share can vary in order to make provision for the various starting points of renewable energy production (ranging from 10% for Malta to 49% for Sweden).
4. Innovation and financing: With the NER300 programme and Horizon 2020, the EU encourages the growth of innovative low-carbon technologies.

1.2.2 2030 climate & energy framework

The 2030 Climate and Energy Framework covers EU targets and policy objectives for the period from 2021 to 2030. This plan is really only an update of the previous one because it is based on the same principles, regarding the reduction of greenhouse-gas emission and the development of green technologies. The objectives for 2030 are:

- Reduction by 40% (1990 levels) of Greenhouse gas emissions.
- Renewable energy share of 32% of the total energy consumption.
- Energy Efficiency increased by 32.5%.

As in the previous plan, the EU ETS and non-ETS sectors must meet the new objectives. Therefore, the ETS sector must cut greenhouse gas releases by 43% (compared to 2005), whereas the non-ETS sector must decrease its emissions by 30% (compared to 2005). The EU government has assumed an “an integrated monitoring and reporting rules to guarantee a development upon its 2030 climate and energy targets” [2]. The scope of the framework is to support the EU member countries in building a global energy system that:

- Ensures Energy Security providing affordable energy for all consumers.
- Reduces the dependences on energy imports.
- Fosters Innovation and competitiveness.

- Improves Energy Efficiency in order to decrease the total energy consumption.

1.2.3 European Green Deal

The European Green Deal is a law that ensures the long-term transformation of the European Union into “a modern, resource-efficient and competitive economy” based on the development of an economy uncoupled from resource use and on the achieving of zero net emissions in 2050. This target could be achieved through different actions:

- Decarbonising the energy sector, which accounts for 75% of the EU’s greenhouse gas emissions.
- Renovating buildings to help people cut their energy bills and energy consumption, which represent 40% of the total energy use.
- Providing support industry to innovate and to become important leaders within a green economy.
- Developing new, cleaner and healthier ways of mobility.

The European Union offers economic support to the member countries, regions, industrial sectors and workers, affected by this transition. This policy, called the “Just Transition Mechanism”, aims “to ensure that the transition towards a climate-neutral economy happens in a fair way, leaving no one behind”. Therefore, the financial support (at least 150 billion of euros) will be allotted to the countries, industries and sectors which are at present the most carbon-intensive [3] [4].

At this point, therefore, it would be appropriate to review the situation of Cyprus regarding its past and future energy strategy as well as its reference energy system.

1.3 Energy Balance of the Republic of Cyprus

In this section, Cyprus’s Energy Balance is described by considering a very detailed set of energy indicators. It must be underlined that *Cyprus* here refers only to the areas under the Republic of Cyprus (ROC), as data are not available for the entire

island of Cyprus [for obvious political reasons].

Before discussing in detail the main energy indicators, it is necessary to have a clear picture of the ROC energy context. The Cypriot state has suffered from energy isolation due the total absence of electricity and gas interconnections. However, in recent years, various energy projects have been implemented in order to solve this problem. Two of them are the EastMed Project and the EuroAsia Interconnector Project.

The EastMed project is based on the construction of a natural gas pipeline, directly connecting East Mediterranean energy resources to Greece via Cyprus and Crete. The pipe will have a total length of 1,900 km and will transport 10 billion cubic meters per year of natural gas from the off-shore gas reserves in the Levantine Basin, eventually as far as Italy [5]. The EU Commission has contributed to this project with financing to the tune of €34.5 million, a sum which is justified, considering the established key European goal of diversifying its gas suppliers and decreasing its dependence on Russian natural gas supplies [6]. The EuroAsia project, on the other hand, relies on an HVDC interconnector between the Greek, Cypriot and Israeli power grids via a long submarine power cable (310 kilometres from Israel to Cyprus and 898 kilometres from Cyprus to Greece, for a total of 1,208 kilometres) [7] [8]. For ROC this is an important step forward, which will end its electricity isolation from the EU countries [9].

To return to the study of the main energy indicators after this necessary digression: the total primary energy supply (TPES) of Cyprus in 2018 was 2218 ktoe, which is similar to the value before the oil crisis. The trend of TPES is represented by the

following chart [10]:

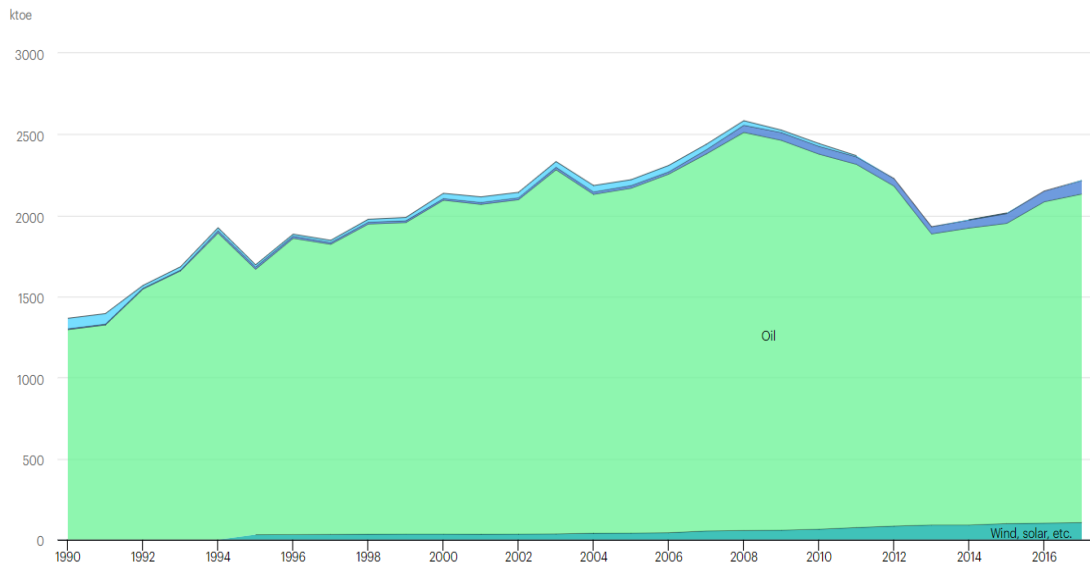


Figure 1: Cyprus' TPES [ktoe] [10].

The TPES peak value was in 2008 (2584 ktoe), followed by a steady decrease, bottoming out in 2013. The trend then reversed, with a steady increase in Oil and Renewable energies which has continued up to the present date. Cyprus's energy sources consist principally of oil (91%), while Biofuels and waste (3.7%), Renewable Energies (4.7%) and Coal (0.6%) account for the remaining percentage. The key challenge for Cyprus is, therefore, to reverse its high dependency on fossil fuels and it is crucial for the country to develop both its hydrocarbon (discovering and tapping Exclusive Economic Zone – EZZ - reserves [11]) and renewable energy sources.

Cyprus's total final consumption (TFC) amounted to 1565 ktoe in 2018. TFC accounts for around 70% of TPES; the residual part is transformed by the power generation sector to produce electrical energy. The TFC trend is almost similar to that of TPES, thus showing the close interdependency between these two indicators, as can be seen in the following chart [10]:

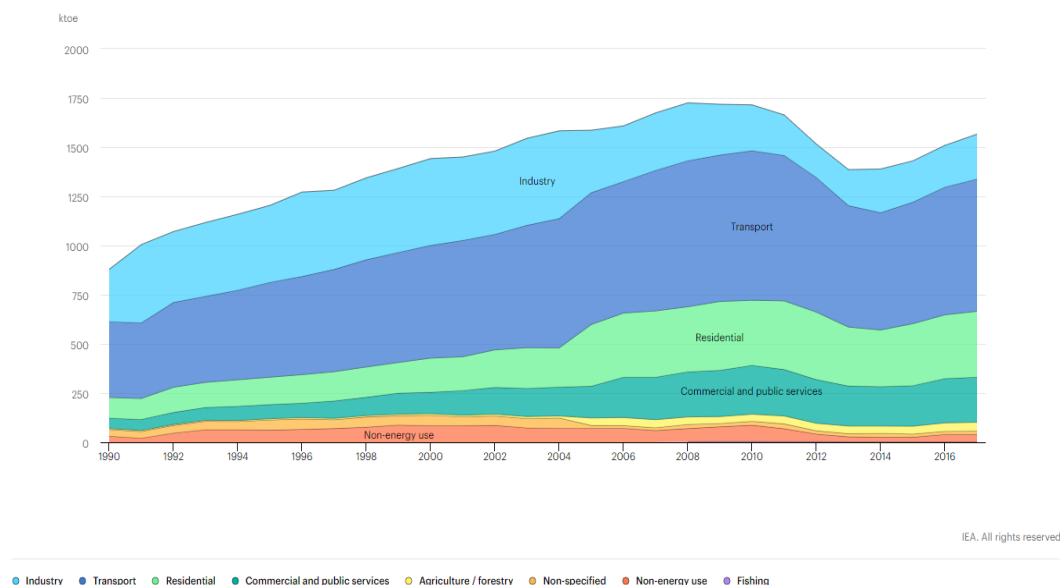


Figure 2: Cyprus' TFC by sector [ktoe] [10].

The transport sector and other sectors (such as Agriculture, Commercial & Public Services, and Households) constitute the largest consuming sector with 43% and 41% of the TFC respectively, whereas only 16% is consumed by the Industrial Sector. The main fuel used is the oil at 65%, while electricity accounts for 25%. The remaining part is supplied by Renewable energies (including Biofuels and Waste) and coal. This situation is clear in the next chart [10]:

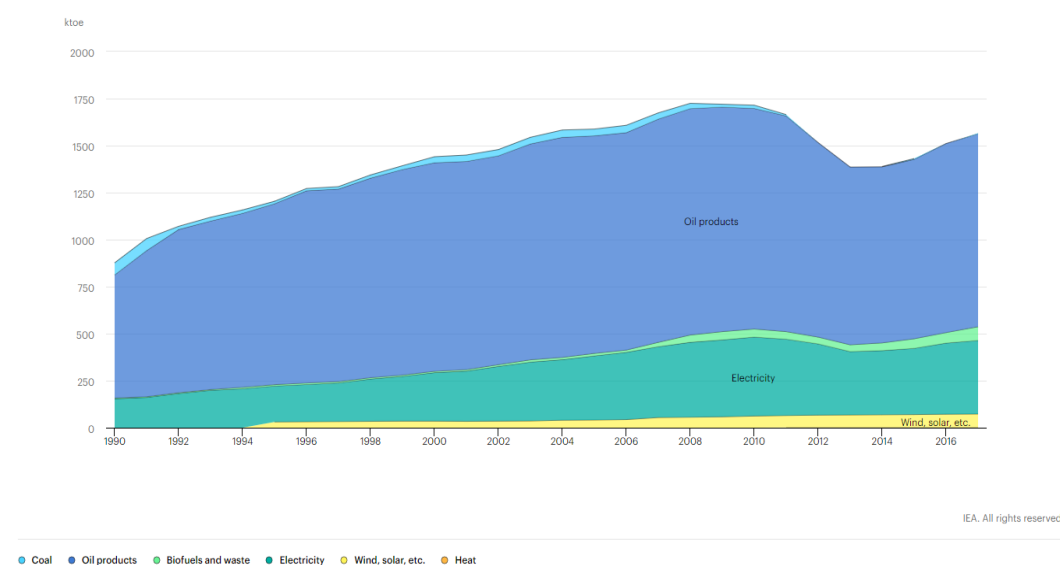


Figure 3: Cyprus' TFC by source [ktoe] [10].

The production from domestic sources is not sufficient to meet this demand because it contributes only to 144.7 ktoe, which is mainly generated by renewable sources and Biofuels [12]. As a matter of fact, the country imports the equivalent of 2712 ktoe, 97% of which is based on Oil and petroleum products, while the tiny remaining part comes from renewable sources, other fossil fuels and non-renewable waste. The following graphs illustrate this [10]:

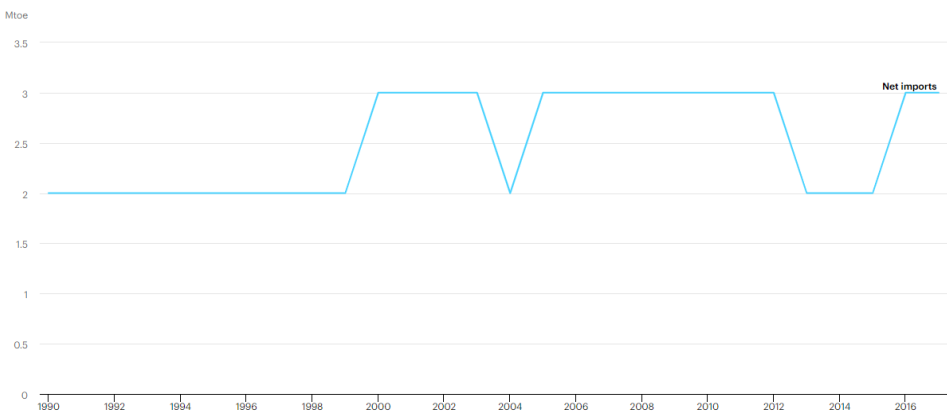
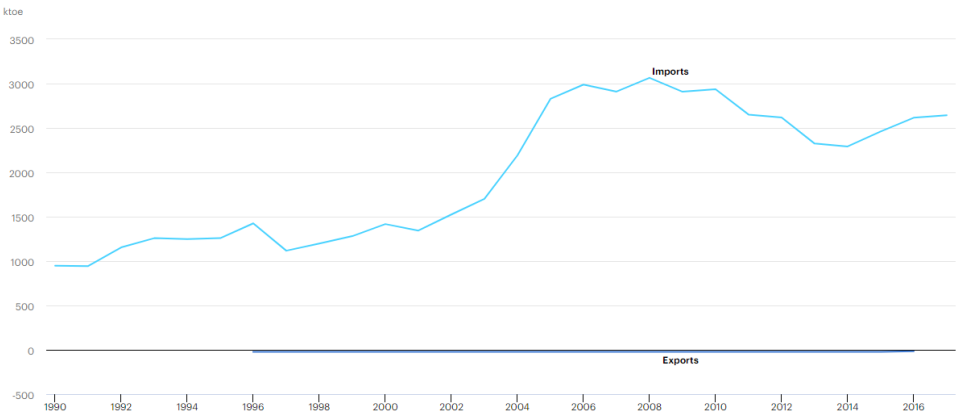


Figure 4: Cyprus' Net Imports [10].



IEA. All rights reserved.

Figure 5: Imports and Exports of Oil in Cyprus [10].

In the light of these data, it is clear that the Republic of Cyprus (ROC) is highly dependent on the international energy market, thus in the recent years ROC has pushed for a greater exploitation of renewable resources. Since the electricity cannot be imported to Cyprus in the immediate future, the country's present demand is being faced by its internal production, which, as mentioned above, largely relies on oil-fired power plants by 91%, whereas 9% is obtained from green energy sources (Solar plants, Wind farms and Biofuels):

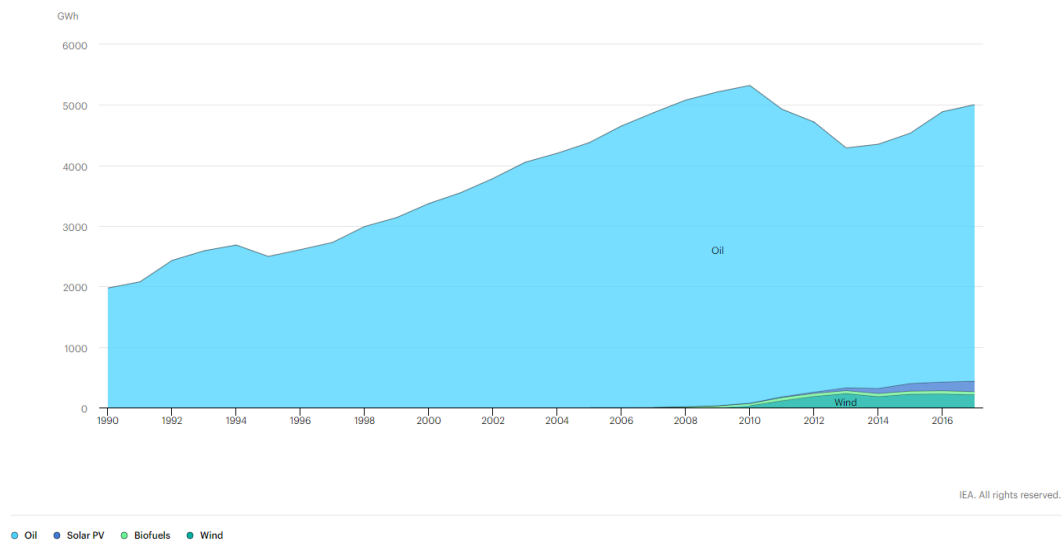


Figure 6: Electricity production by fuel in Cyprus [GWh] [10].

Since 2007 the amount of “clean” electricity production has grown as a consequence of the 2020 Climate & Energy target, whereas electricity produced by Oil-fired power plants decreased from 2010, due to the Cypriot economic crisis (see the next paragraph), until 2013, when values began to steadily increase. In 2017, at least 435 GWh of electricity was produced by low-carbon electricity generation systems: in detail 172 GWh by Solar PV, 211 GWh by Wind Farms and 52 GWh by Biofuels. Solar PV and Wind Farm production has also increased since 2010, (apart from a brutal arrest in 2013) whereas Biofuels steadily increased until 2011 after which production levelled out [10]:

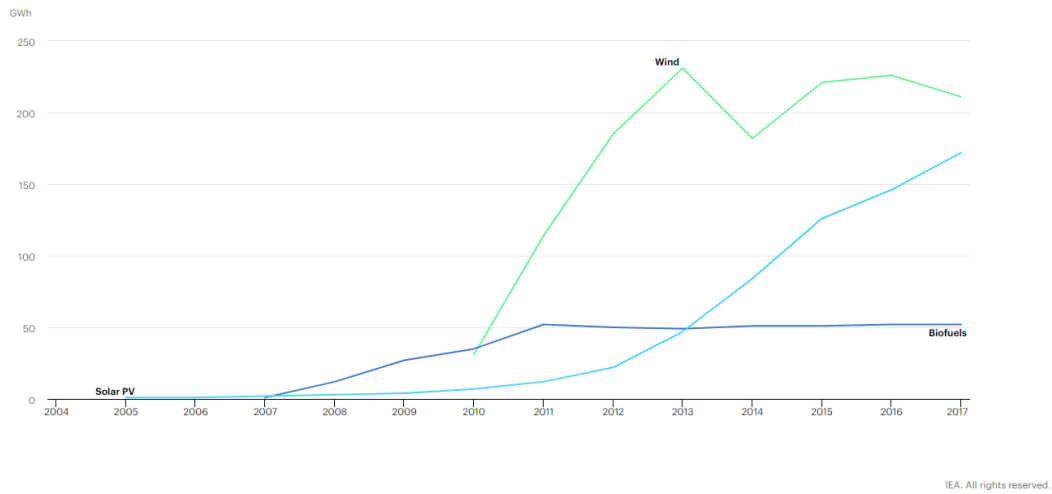


Figure 7: Low-carbon electricity generation by source in Cyprus [GWh] [10].

Within the Reference Energy System of ROC, the Solar Hot Water (SHW) Technologies must be taken into account, considering their high heat production and therefore the great savings they offer in terms of CO₂ emissions. As a matter of fact, it is estimated that the number of SHWs installed in Cyprus exceeds 80,000 units for residential buildings, consisting of the thermo-syphon type or the forced circulation type. This number of units represents around 96% of the total installed collector area in Cyprus (560,000 m²). Indeed, 70% of the households in Cyprus have a SHW system installed. [13].

Another important indicator of the performance of the national energy system is a country's energy intensity defined by the ratio between the energy supply and the gross domestic product measured at purchasing parity. It indicates how much energy is used in order to produce one unit of economic output. As shown in the following graph, since 2005 the energy intensity of Cyprus has been decreasing, which means that less energy is being used to produce one economic unit. This trend is a consequence of the development of new technologies and thus to the improvement in energy efficiency of the systems used [14]:



Figure 8: Cyprus' Energy Intensity [MJ/\$2011] [14].

As mentioned above, in 2010 the Cypriot economy found itself facing an important crisis that caused a fall in its GDP, as portrayed in the next chart [14]:

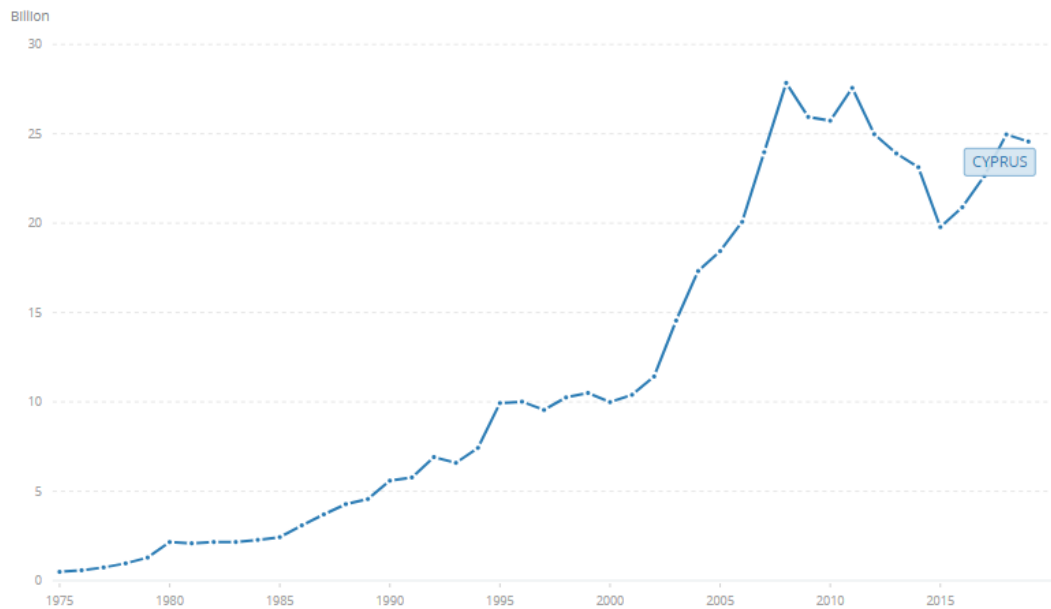
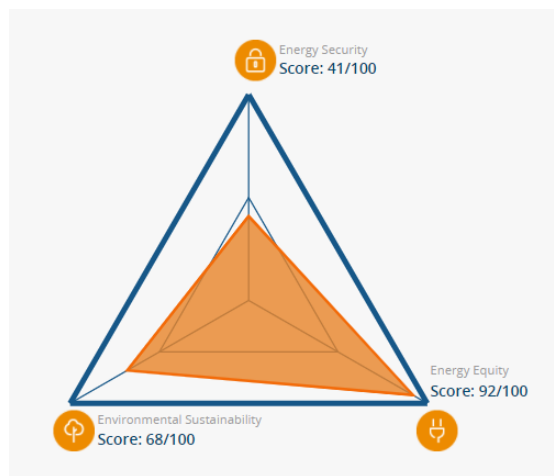


Figure 9: Cyprus' GDP (current US\$) [14].

Finally, in order to globally assess the Energy panorama of Cyprus, the Energy Trilemma can be used. It is a concept that pools three different core dimensions



regarding environment sustainability, energy security and energy equity. The Republic of Cyprus is ranked 54th out of 120 countries in a special ranking which explains how well a country manages the trade-offs of the Trilemma, with "A" corresponding to the best mark. Here the Security grade is D due to the low diversity and weak

energy independence, whereas Environmental sustainability and Energy equity are grade B, due to the increasing share of green energies and high access to electricity [15].

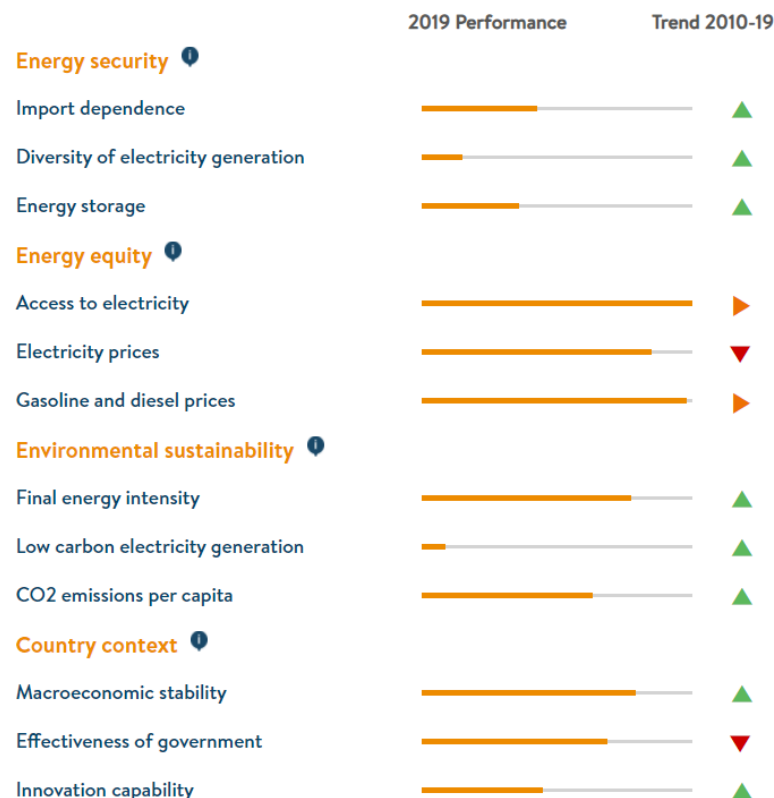


Figure 11: Performances in the three core dimensions of the Energy Trilemma [15].

2. Solar Energy

Solar Energy is the energy related to the solar radiation that is exploited by a variety of constantly evolving technologies, such as solar heating, photovoltaics, solar thermal energy, solar architecture and molten salt power plants. It may be the most promising energy source on Earth, with 174 PW of annual incoming solar radiation in the upper atmosphere. 51% of this amount reaches the ground and oceans, while roughly 35% is reflected back into space and 14% is absorbed by the atmosphere [16].

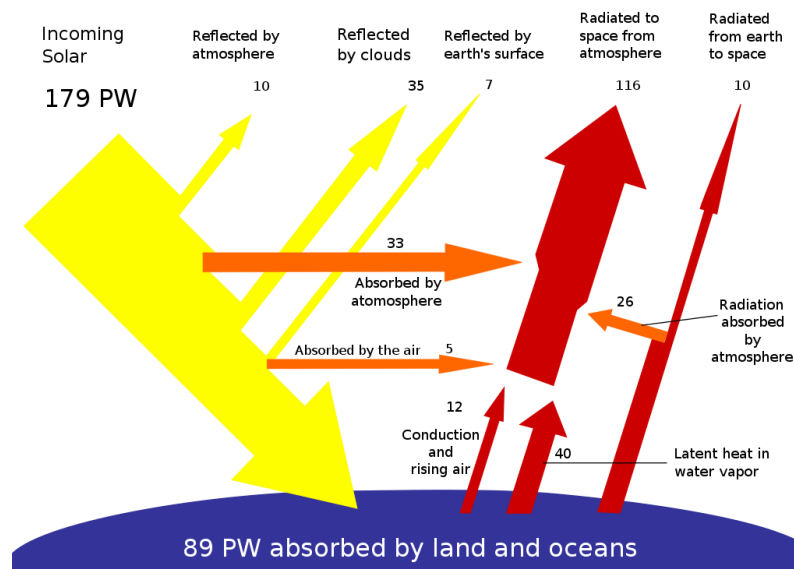


Figure 12: How the Solar Energy reaches the Earth's Surface [16].

In the visible light range (400 to 700 nm), the atmosphere is mostly transparent, whereas it is opaque to IR radiation. This stabilizes the Earth's medium temperature at 20 °C. The recapture of radiation on the Earth causes a temperature increase. This happens, for instance, because of the growing amount of greenhouse gases emitted into the atmosphere, which increases its capacity to recapture the radiation which ought to be reflected back into the universe [17].

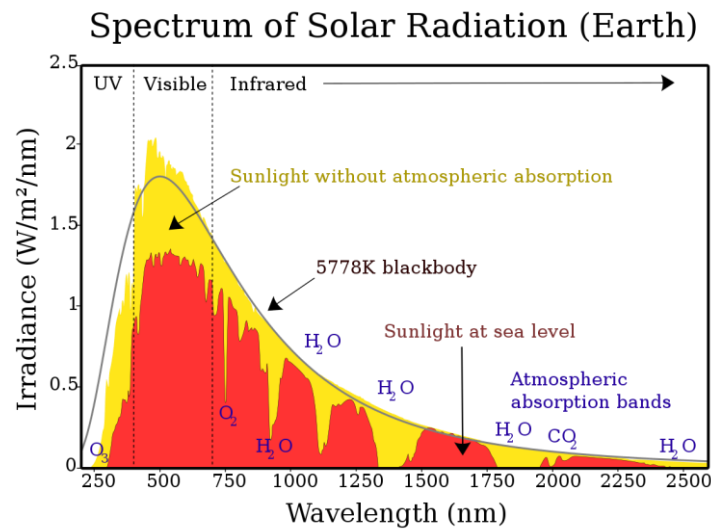


Figure 13: Solar spectrum [17].

The yellow shading represents the solar radiation reaching the top levels of the atmosphere before absorption and scattering. The red colour represents the radiation that eventually impinges on the Earth's surface, which is a substantial amount. This potential resource cannot be fully exploited by humans due to a set of factors including:

- Time variation: During the night, obviously any solar radiation cannot be absorbed. It limits the capability of the solar panels to absorb in one day.
- Cloud cover/Weather: It can affect because clouds are able to block the incoming light from the sun (5th Chapter).
- Land availability: Only a certain area are suitable for the installation of solar panels. Obviously, the solar plants can't be installed everywhere.
- Seasonal variations: It affects hardly the daytime length during a year.

2.1 Solar Technologies

Solar technologies are systems transform solar energy for different uses. They can be ranked from different points of view: they can be active or passive systems depending on the way they capture, convert and distribute sunlight. Active solar technologies are photovoltaic, concentrated solar power and solar thermal

collectors to convert sunlight into useful outputs whereas passive solar technologies (such as selecting materials with advantageous thermal properties, designing spaces that naturally circulate air and referencing the position of a building to the Sun) are employed to optimize the energy consumption of a user. To be more precise, the active ones represent different ways in order to produce energy from a solar source as a supply side technology, while passive ones are considered demand side technologies. From the active solar technology perspective, the sunlight can be processed in two useful energies, which are thermal and electrical one.

2.1.1 Solar Thermal Technology

Solar Thermal Technologies convert the solar radiation to thermal energy, which can be used to heat fluid for micro-, meso- or macroscale energy users or can be post-processed in a connected cycle for electricity generation. Solar thermal collectors are classified as low-, medium-, or high-temperature collectors. Low-temperature collectors are unglazed and are used to heat swimming pools or to heat ventilation air, therefore they are generally designed for micro-scale energy systems. Medium-temperature collectors are usually flat plates but are used for heating water or air for residential and commercial uses. High-temperature collectors concentrate sunlight using mirrors or lenses and operate at temperatures higher than 150°C and to pressure level reaching 20 bar (or higher depending on HTF) in industries and for electric power production (CSP).

2.1.2 Solar Power Technology

Solar Power Technology is a particular system that is able to convert solar energy into electricity, either directly with PV systems or indirectly using CSP technologies (to be discussed later). Solar Power Technology is predicted to be the system which will contribute most to energy production in 2050, covering 27% of worldwide electricity consumption [10]. Many industrialized nations have chosen to install significant solar power capacities into their grids to ensure an alternative to conventional energy sources, while an increasing number of developing nations

have turned to solar energy to reduce their dependence on expensive imported fuels. PV systems directly produce electricity in DC and their power is dependent on sunlight intensity. Different solar cells are combined together within modules, which are connected in series by strings. Multiple strings are linked in parallel coupling in order to create an array. PV plants require inverter for providing electricity in AC with a specific frequency.

3. *Concentrating Solar Technologies*

The Concentrated Solar Technology harnesses the Solar Energy, concentrating it on a line/point receiver with the aim of generating thermal energy or electricity. The overall energetic conversion can be divided into two steps:

- Firstly, direct sunlight is exploited by concentrating it into a focal point or line (Point Concentration or Linear Concentration), where a HTF (Heat Transfer Fluid) passes and receives the thermal energy of the concentrated sunlight. The HTF can be synthetic oil, molten salts, air, particles, CO₂... or simply water.
- Finally, if the plant is designed for power generation (CSP), via either Steam Rankine Cycle (or Organic Rankine Cycle) or Brayton Cycle, the thermal energy feeds a turbine for the electricity generation. For some of CSTs systems (e.g. Solar Parabolic Dish), the possible conversion from Solar Energy to Electricity could be done directly through Stirling engines (cf. *3.1.3 Solar Parabolic Dish SPD*).

This procedure is consequently completely different from a traditional thermoelectric power station since its thermal source is provided by the Sun. CSP systems can only benefit from the direct beam radiation and these systems are therefore best suited to regions with a high percentage of clear sky days and where a very high DNI can be measured. In the next picture, World DNI map is presented

[18]:

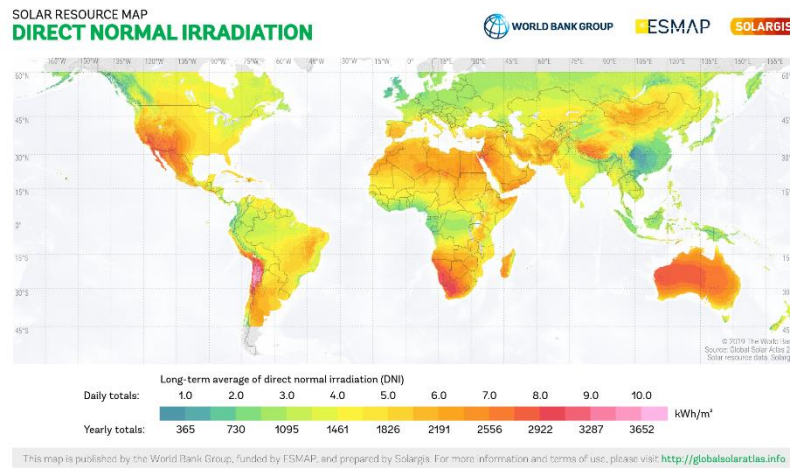


Figure 14: World's DNI map [18].

As it can be seen in the previous figure, the most suitable places for CSP installations are the western area of North America, the south-west of the South America (Andean plateau), the southern area of the Africa, Gobi Desert, Tibet and Australia. In Cyprus the situation is quite good, especially in Nicosia where the compact linear Fresnel reflector (CLFR) of the present study is located. Here the estimated annual DNI is between 2,045 and 2,191 kWh/m² thanks to Solargis method based on long-term average of yearly/daily sum of direct normal irradiation (DNI) from atmospheric and satellite data with 10, 15 or 30-minute time step. This can be visualized in the next figure [18]:

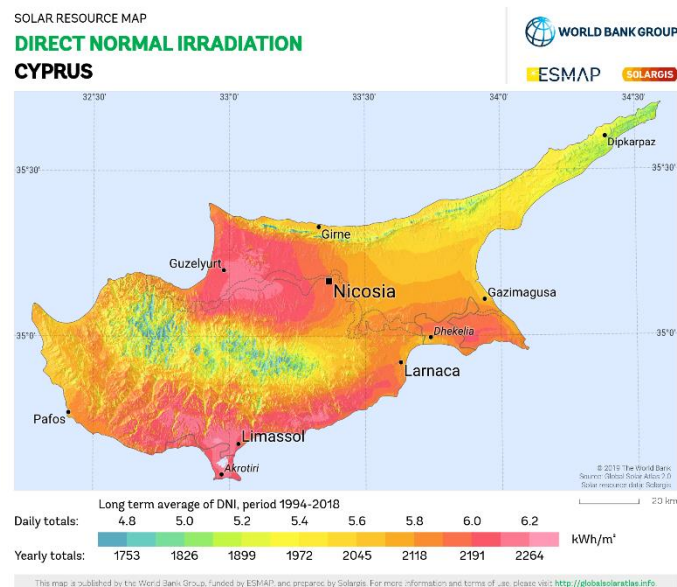


Figure 15: Cyprus' DNI map [18].

A CSP system, if coupled with a thermal storage unit, is able to produce electricity when there is no sunlight due to time variations or bad weather conditions. Considering aspects such as the electricity dispatching as well as the possible disequilibrium between energy produced and consumed into an electrical grid, the opportunity of coupling the system with a storage system could be interesting. The thermal energy storage can rely either in the form of sensible heat or as latent heat, using Phase-change material (PCM). As discussed before, there are two ways to concentrate the direct sunlight:

- Linear Focus Collectors such as the Parabolic Trough and Linear Fresnel Collectors.
- Point Focus Collectors such as the Parabolic Dish and Solar Power Tower.

CSP is often compared to photovoltaic solar power (PV) since they both use solar energy to produce electricity. While solar PV has grown immensely in recent years due to falling prices, Solar CSP growth has been slowed due to technical difficulties and high investment costs. Nonetheless, CSP systems are the study focus of several research activities all over the world whose aim is to improve its components and make them economically viable. In fact, although there are zero fuel costs, acquiring the CSP technology itself normally requires a significant initial capital investment. In 2017, CSP represented less than 2% of the worldwide installed capacity of solar electricity plants. In 2008, CSP Technology had a global installed electric capacity of 5,500 MW. Almost an half of that capacity (2,300 MW) is installed in Spain, followed by the United States with 1740 MW [19].

3.1 Types of CSP systems

CSP technologies include four optical types, specifically parabolic trough collectors (PTC), solar parabolic dishes (SPD), compact linear Fresnel reflector (CLFR), and solar power tower (SPT). These technologies can be classified by their Concentration Factor. This is a ratio that renders how an incident energy flux I_0 is focused on the receiver surface with a flux I_r ; This definition is easily understood with the following figure [20]:

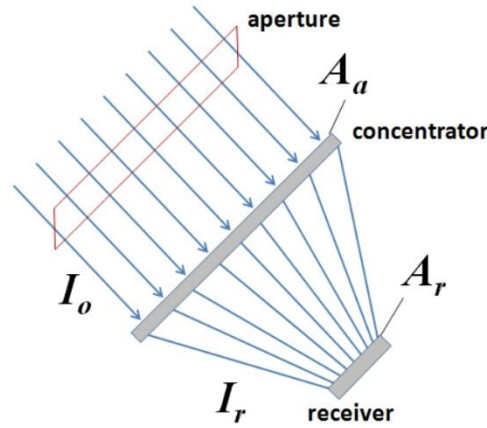


Figure 16: Schematic representation of light concentration process [20].

This parameter can be obtained by two different ways:

- Geometric Concentration Ratio C_{geo} : Defined simply as the ratio between A_a Area of Aperture over A_r Area of the Receiver. In most cases, a uniform radiation flux does not occur over the aperture. Therefore, this ratio is global. The resulting unit is usually referred to as the number of suns reproduced.
- Optical Concentration Ratio C_{opt} : More widely used than the previous one and more precise, it is defined as the ratio between the energy flux ratio at the aperture and at the receiver. It can be equal to the geometric ratio if the insolation (energy flux over the aperture) and irradiance (energy flux over the receiver) fluxes are uniform on those areas [20].

Linear focus collectors achieve medium concentration (>25 suns), and point focus collectors achieve higher concentration (>500 suns) factors. These values are far below from the theoretical ones, which relies on, for linear and point concentrations, 215 and 46248 suns respectively [21]. According to their tracking, the different types of concentrators produce different peak temperatures and correspondingly varying thermodynamic efficiencies. In the next paragraphs, three different CSP technologies are described, while the Linear Fresnel Reflector will be discussed in the next chapter.

3.1.1 Parabolic Trough Collector

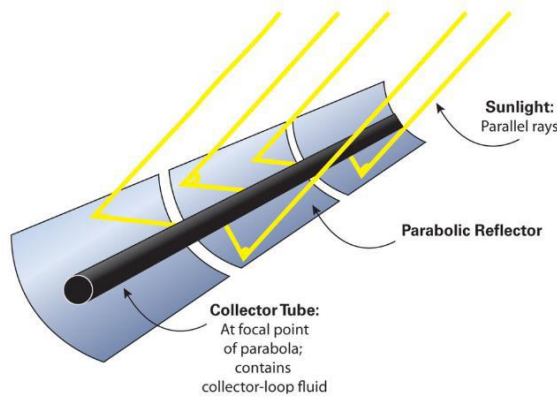


Figure 17: Parabolic Trough Collector [22].

The parabolic trough collector is the most widespread of the CSP technologies. It consists in a series of parabolic U-shaped reflectors that focus the solar direct beam onto a linear receiver located at the reflector's focal line, which could be aligned to the North-South direction but generally an East-West one is preferred for a better yield. The

receiver enclosing the absorber is a tube positioned directly above the middle of the parabolic mirror and filled with a working fluid, which could be oil, molten salt or another material. To improve that task, the receiver is coloured in order to achieve maximum absorption of the solar irradiation and a reduction in heat losses. A tracking system allows the primary optic to be constantly aligned in the direction of the sun. Depending upon different parameters (such as the concentration ratio, solar intensity and working fluid flow rate), the temperature of the working fluid can reach almost 400-600°C. Among the various solar harvesting technologies, this system ensures the best land use. Some parabolic-trough plants use a fossil fuel based back-up to supplement energy production during low solar radiation, and often the trough system can be integrated into a conventional natural-gas-fired or coal-fired plant. Compared to other CSP technologies, the parabolic-trough system is the most advanced with its nominal power of 15-100 MW at solar-to-electric conversion efficiency of 14-16% [22].

3.1.2 Solar Power-Tower (SPT) / Central Receiver

SPTs are CSP power generation systems that use a field of flat mirrors (heliostats) to reflect sunlight onto a solar receiver, usually placed on top of a central tower, although sometimes there are multi-towers as for example in the Ivanpah Solar Power Facility (California, USA) which, connected to the grid in September 2013, has a gross capacity of 392 MW [23]. The field can be composed of several thousands of heliostats, which have the task of maintaining the targeting from sunrise to sunset. The tracking of the heliostats is based on two possible strategies [24]:

- Spinning-Elevation Tracking: One of the two axes (Spinning axis) of the Heliostat points towards the target, whereas the other axis (Elevation axis) is perpendicular to the previous one and tangent to the heliostat frame.
- Azimuth-Elevation Tracking: One of the two axes (Azimuth axis) of the Heliostat points towards the zenith, while the other axis (Elevation axis) is perpendicular to the previous one and tangent to the heliostat frame.

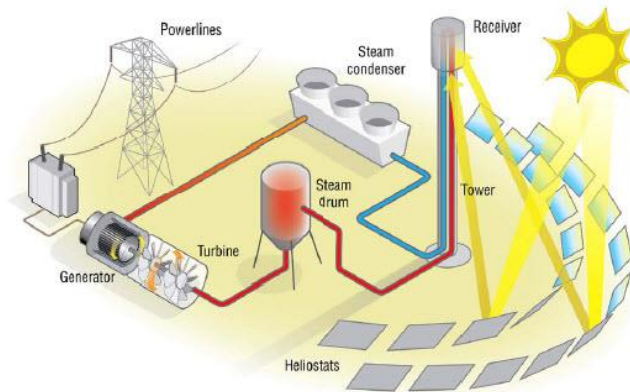


Figure 18: Example of a Steam Solar Power Tower [22].

The strong solar flux impinging the receiver (200 kW/m^2 - 1000 kW/m^2) offers the possibility to achieve a high working temperature, to work at better efficiency, due to high exergy. The objective

of SPTs is to produce high-temperature thermal

energy, which could be used for industrial applications, like solar chemistry, or simply for the production of electricity by the conventional cycle. Such plants may operate with molten salts, supercritical CO_2 , liquid sodium or air as the working fluid. In a steam SPT, like the Ivanpah Solar Power Facility, water is forced onto the receiver in order to be heated up over 500°C : a part of this is stored in a heat storage drum, whereas the majority is used to drive a turbine for electricity production. The stored heat is used in order to continue electricity

production to overcome short-term solar intermittency.



Figure 19: Solar Power Tower [22].

In an SPT with molten salt, the process is different, because two different cycles are present. The cold molten salt (290°C) is pumped to the receiver where it is warmed up by concentrated solar energy via the receiver. After reaching a temperature of around 565°C , it is sent to the hot storage tank. The hot salts then flow inside the heat exchangers to transfer their thermal energy into the water-steam cycle (Rankine Cycle) for electricity generation. The cooled salts are stored in a cold storage unit before being pumped again to the receiver again. Within the Rankine Steam Generator, the water obtained from the condenser is able to begin again the cycle from the heat exchanger with the hot salts [22]. An example of an SPT facility with molten salt is the Pentakomo Field Facility (PFF) located at the south coast of Cyprus where a cogeneration of electricity and desalinated seawater is obtained. The plant contains a heliostat central receiver system, thermal energy storage in molten salts, a Rankine Cycle for electricity production and finally a Multiple Effect Distillation (MED) unit for desalination. In this facility, the steam is generated in a single tank as opposed to the usual two-tank configuration. The diagram below shows a simplified structure, which helps to understand how the desalinated water and electricity are achieved:

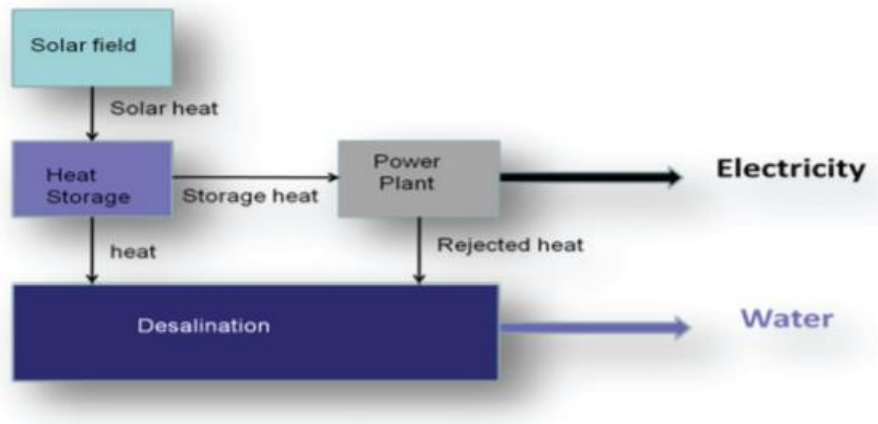


Figure 20: Schematic representation of the energy flow in PFF [25].

The heliostat field is composed of 50 heliostats with a 5 m^2 area for each one. With a reflectivity of 93%, they are able to follow the position of the sun with a proper two-axis (spinning-elevation) tracking device. The central receiver, which is located on a 14 m tower, is a cavity type receiver with a circular aperture of 0.8 m. The concentrated solar radiation generated by the reflection of the heliostat field is centred into the internal surface of the receiver, which includes four cavities in order to improve on the one hand the “capturing efficiency” of the receiver and on the other the performance of the heat transfer between the absorber and working fluid. To exploit heat losses, the hot air produced in the cavity of the receiver is used to pre-heat the seawater of the MED desalination unit. The hot molten salts are channelled to a thermal energy storage (TES). Therefore, in that plant, the molten salts are used not only as a working fluid but also as a thermal storage medium too, thanks to their thermic and chemical characteristics and, to avoid their solidification in case of low temperatures, five electrical heaters are installed. With temperature up to 570°C , the capacity of the TES is around 0.6 MWh. As discussed before, within the TES an immersed coil type heat exchanger connected to a water cycle is utilized for electricity production and water desalination [25]. The entire process can be visualized in the next picture:

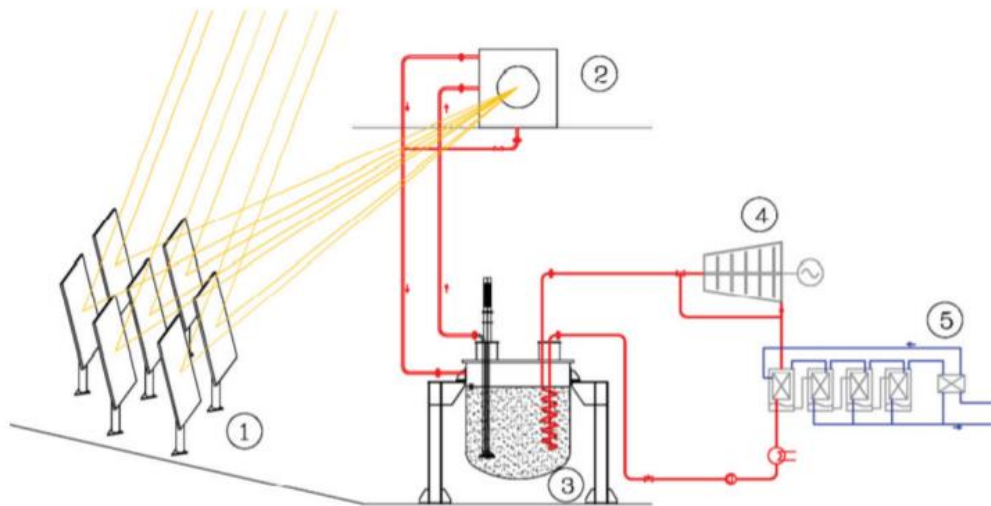


Figure 21: Structure of PFF's Cogeneration Power Plant. (1) Heliostat Field, (2) Receiver, (3) Thermal Energy Storage, (4) Rankine Cycle and (5) MED desalination unit [25].

3.1.3 Solar Parabolic Dish (SPD) System



Figure 22: SG4 system [26].

The Solar Parabolic Dish relies on a parabolic point-focusing concentrator in the form of a dish that is able to concentrate the solar radiation onto a receiver mounted at the focal point. The different mirrors are installed in a structure with a dual-axis (usually azimuth-elevation) tracking system, which is one of the most important advantages of these CSP technologies because it allows the system to be directly aimed at the sun

and therefore not to suffer from cosine losses, as occurs with PTC and SPT. To obtain higher values of reflectance (90-94%), a percentage of iron must be added to the glass-silver surface to the back of the glass. With a diameter varying from 5 to 10 m and therefore with a surface area of 40-120 m², the SPDs are able to generate between 0.01-0.5 MW of electricity power. At the focal point, due to the high concentration, the temperature and the pressure of the working fluid can reach respectively 700°C-750°C and 200 bar, respectively. A Stirling engine is usually installed in this position in these technologies, because it permits a very high solar-to-electric conversion efficiency, specifically around 25% and 30%. The Stirling

Engine is a system that allows the net conversion of the heat energy to mechanical work, operating the cyclic compression and expansion of working fluid at different temperatures. Despite the lack of thermal storage, SPDs are wide-spread solar technologies, thanks to their various characteristics:

- High conversion efficiency.
- Easy to install.
- Opportunity to reduce costs with large scale production [22].

An example of such a system is the SG4, the world's biggest solar power dish with its 494 m² of aperture area. Constructed in 2009, the plant is the result of a design mission aimed at minimizing of the instalment cost and technical risks and at the same time optimizing of its reliability. Its peak concentration reaches a value of 14,000 suns [26].

4. *Linear Fresnel Reflector*



Figure 23: Example of LFR [27].

Linear Fresnel Collectors (LFC) or Linear Fresnel Reflectors (LFR) [27] are an extensive type of CSP technologies for a broad set of applications, of temperature heat processing, air-conditioning, electricity or power generation. It is different from PTC since the sun rays reaching the receiver are

reflected by almost flat mirrors placed in parallel rows. An LFR system is basically made up of primary mirrors, which are managed by a tracking mechanism considering the sun position and a fixed receiver, where the reflected sunlight absorbs thermal energy and it is transferred to a working fluid. The receiver could be equipped with a secondary optic (cf. Paragraphs 4.3.1 and 4.3.2) to recover the reflected sunlight otherwise lost due to spillage or tracking errors. It may be positioned between 5 and 10 m above the primary optic, which is set at a low height to reduce the wind load. Therefore, thanks to its potential light weight and low wind load, an LFR can be installed on a roof for air conditioning-purposes at low operating temperatures (starting from 150°C) with a low thermal capacity (starting from 50 kW), as is the case at the Cyprus Institute. LFR technology can also be used for electricity generation, at a temperature beyond 400°C and with an higher thermal power capacity (>1 MW) [28].

4.1 *LFR Main Applications.*

LFR systems can operate at a wide range of outlet temperatures usually correlated to the reflector dimensions, giving the opportunity to use them for a number of applications.

4.1.1 Power Generation Applications



Figure 24: Dunhuang Dacheng 50 MW Molten Salt LFR [29].

Only a minority of installed LFR plants are involved in power generation, but in future this may be considered the most important application thanks to the high number of research studies in this field. There are various examples of LFR plants

installed for power generation purposes. One of them is the Dunhuang Dacheng 50MW Molten Salt Linear Fresnel CSP, which was connected to the grid on December 31st of 2019. This was the first demonstration CSP plant with LFR in China. Unlike to the usual HTF used in LFR, this plant relies on molten salts that transfer heat to a Steam Rankine Cycle to generate electricity via a 50 MW Turbine. A thermal energy storage system can store energy for 13 hours [29] [30]. The Puerto Errado 2 LFR power plant, which was constructed by the German company Novatec Solar, has been in operation since August 2012. It can produce 49 GWh_{el} yearly with an electric generation capacity of 30 MW and an aperture area of 302,000 m² divided into 28 rows. In contrast with the Chinese plant, the electricity is produced using water, as the HTF is directly channelled to a Steam Rankine Cycle [31] [32].

4.1.2 Thermal Applications



Figure 25: LFR plant installed in Sardinia for Heat processing for a cheese industry [33].

Generally speaking, the LFR plants are built for thermal power production in two main applications: Heat processing, and solar air-conditioning. Heat-processing refers to the solar supply of heat to industrial processes. One example is located in Sardinia (Italy), where

there is an LFR with a yearly thermal output of 600 MWh. It supports a cheese industry saving 150 ton of CO₂ emissions and 50,000 litres of gas oil every year



Figure 26: LFR plant installed in Johannesburg for cooling purposes [34].

[33]. Whereas, for the other thermal applications, an example is the LFR in Johannesburg (South Africa), which, with its 242 solar mirrors covering a total area of 484 m², is able to feed an absorption chiller with pressurized water at 180 °C.

Peak cooling capacity is 330 kW [34]. In the next paragraph, the plant, which is the main subject of this report, is presented.

4.1.3 Linear Fresnel facility at Cyprus Institute



Figure 27: LFR placed at The Cyprus Institute [36].

The solar Fresnel facility, which is the main subject of this report, is located on the roof of a building close to the Novel Technologies Laboratory (NTL) building of The Cyprus Institute. It is one of the four demonstrative plants developed within the framework of the Small scale

Thermal Solar district units for Mediterranean communities (STS-Med) project [35]. The three other pilot plants are located in Italy, Egypt and Jordan. The spirit behind the project was to develop multi-generative small scale concentration systems for the built environment: heating, cooling, electricity and thermal storage adapted to local needs. Although different designs were used for the four plants, the main objective shared all of them is the cooling, which is understandable in view of the geographical position of the four sites. Specifically, in the Cyprus case the facility is mostly exploited to support the cooling demand of the NTL building of

the Cyprus Institute during the summer. In winter the system is utilized to supply hot water and space heating. The Cypriot Fresnel collector is made up of 18 parallel North-South aligned rows of 16 mirrors (0.32m x 2m) with a total reflective area of 184.32 m². They are driven by 72 motors (4 mirrors per motor) supported by magnetic encoders to control their actual position with an accuracy of 0.1°. The absorber, placed at 3.5 m above the mirrors, is 32 m long and includes 8 tubes connected in series. It contains an inner steel pipe called absorber, where the HTF flows, and an outer vacuum glass pipe, employed as a thermal insulation. Its transparency ensures the high transmittance of the reflected sunlight from the reflectors. A small tank of HTF is embedded in the loop in order to buffer the temperatures and as it is wrapped around with electric heaters, it allows the preheating of the oil. The 2 m³ thermal storage system operates with pressurized water. Moreover, it includes a nitrogen expansion vessel to pressurize both HTF (up to 1 barg) and water (up to 5 barg) loops. A third loop of water sends the thermal energy to an absorption chiller and the HVAC (Heating, Ventilation and Air Conditioning). The thermal COP of the absorption chiller is 0.7, with a nominal cooling capacity of 35 kW. As discussed above, the system may be used in winter to supply the space heating system of the NTL building bypassing the absorption chiller and therefore heating two stratified water tanks of 2000 L each one [36]. The entire process is summarized by the next figure:

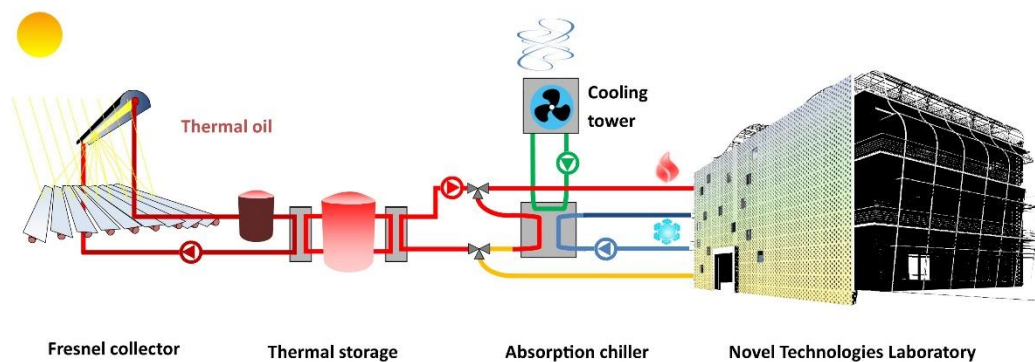


Figure 28: Layout of the entire process placed at The Cyprus Institute [36].

4.2 Components of an LFR

The constant search for cheaper solutions in the solar energy field has led to a greater interest in LFR technology in recent years. As discussed earlier, one of the most important differences from PTC technology is the independence between the primary reflector and the receiver, which allows a higher exploitation of the working fluid with high temperature levels and a larger mass flow-rate. Indeed the absorber is fixed, unlike the PTC, where the absorber rotates. The tracking system of the mirrors, which could be oriented in a North-South or East-West alignment, is optimized in order to reflect the direct solar rays into the receiver during the daytime. The orientation of the field is important since if it is N-S oriented based the different shading losses (discussed later) vary significantly during the day, whereas with an E-W orientation the shading losses change considerably during the year [37]. The reflection of sunshine works as shown in the next picture [38]:

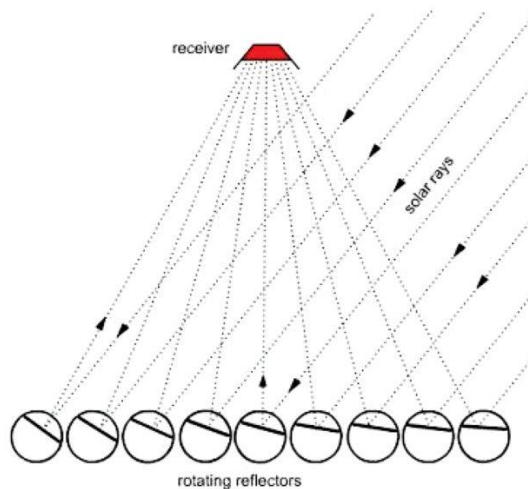


Figure 29: How a tracking system of LFR works [38].

The main components of a Linear Fresnel Reflector are the following:

- Primary Reflector.
- Tracking system.
- Receiver.

4.2.1 Primary Reflector

The primary reflector (or optic) is one of the main components of the LFR since it enables the sunrays to reach the receiver. It is composed of several parallel rows of mirrors, which, thanks to the action of a single axis tracking system (the axis of rotation is parallel to the receiver), track the sun. In most LFR systems, the primary reflector and the receiver are aligned in a North-South direction. The mirrors of the primary reflector could be considered flat, but they are instead moderately curved. The linear Fresnel reflector technology receives its name from the work on optics developed by the French physicist Augustin-Jean Fresnel notably for lighthouses in the 18th century. The principle of the lens developed in lighthouses consisted of multi-faceting of a thick convex glass into an array of thin flat surfaces. In an analogous way, a linear Fresnel mirror can be constructed substituting a parabolic trough by linear parallel segments. Here the very similar performances can be seen:

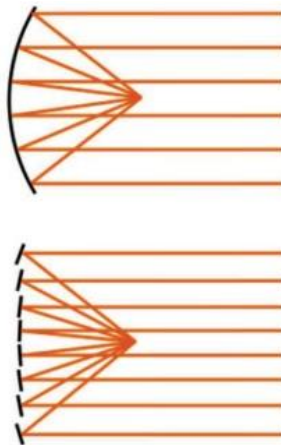


Figure 30: Parabolical Mirror vs Fresnel Mirror [28].

Based on the previous consideration, the focus line of a LFR mirror is the absorber. The nominal capacity of a collector is a function of its reflective area [28]. The collection of the direct sunlight onto the absorber is not perfect. Hence, different optical losses can be found along the process from the DNI up to the aperture of the secondary optic.

There are main three different types of optical losses:

- Blocking losses: they occur when sunrays partially impinge a nearby mirror.
- Shading losses: they occur when a mirror is shaded partially by a nearby mirror, hindering the direct solar radiation from reaching the mirror.
- Cosine losses: due to the angle between the sun, the mirrors and the absorber, spillage occurs unlike for Dish technology as described before.

These losses are depicted here:

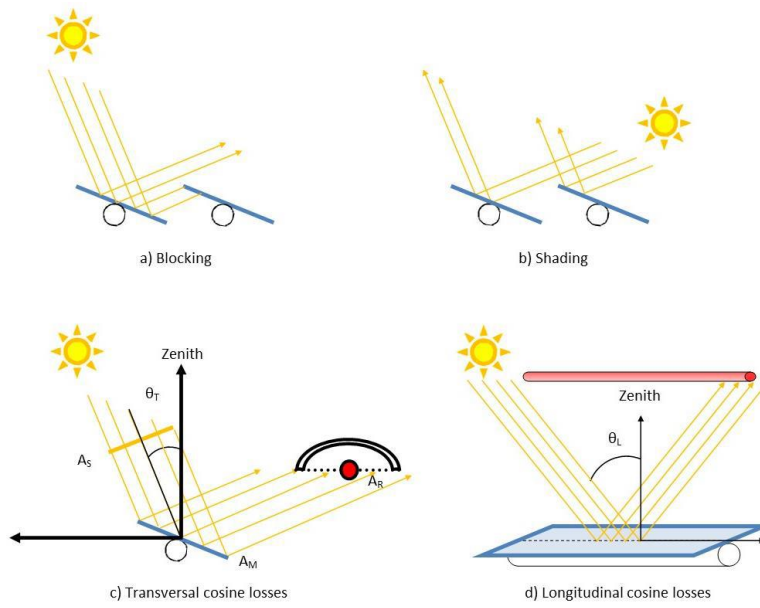


Figure 31: Optical losses of the mirror [28].

As illustrated, there are two types of cosine losses according to the transversal or longitudinal point of view. As a result, perpendicularly to the receiver direction, the transversal losses are referred to the angle θ_T which is formed between the zenith and the sunrays projected onto the transversal plane. They could be easily accounted for by considering the Area A_S defined as the normal surface of the sun rays which hit the mirror. Thereby the orthogonal area A_S to the beams is smaller than the area A_M of the mirror due the angle with the sun. This is not the case with PTC nor SPD because on the transversal plane, mirrors directly track the sun. In the same way, the longitudinal losses are defined considering the angle θ_L between the apparent

angular height of the sun and the zenith. One way to reduce these latter losses could be by minimizing the height of the receiver or the extension of the length of the receiver. Their impact on the optical performance is described in Chapters 6 and 7 [28].

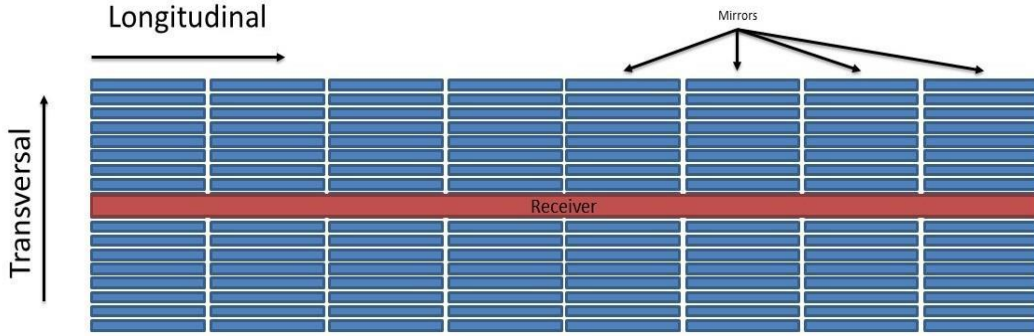


Figure 32: Longitudinal and transversal axis of a LFR [28].

On top of these losses, there are practical losses related to the material and structure of the mirrors. Specifically, the mirrors are not perfect since they present a roughness which modifies the pathway of the reflected sunlight (diffuse reflection not fully specular), therefore it could be a cause of focusing out of the absorber (spillage losses).



Figure 33: Difference in the actions of a perfect mirror against to an imperfect one [28].

Another issue is related to the materials, which compose a mirror. Considering that, the role of a mirror is to reflect the utmost sunlight received, its components must be selected accurately. The behaviour of a mirror with the incident solar radiation (for a given wavelength λ and angle of incidence θ) can be summarized by the following equation:

$$Tr(\lambda, \theta) + Abs(\lambda, \theta) + Ref(\lambda, \theta) = 1$$

Where:

- Tr is related to the transmittance of the glass.
- Abs refers to the absorptance of the glass.
- Ref is the reflectivity of the mirror.

The reflectivity must be maximized close to 1 (in the studied case it is equal to 0.924) in order to reduce the transmittance and absorption. In particular, two materials are combined such as a glass with high transmittance and a material with high reflectivity [28]. Many parameters are considered in the design phase of a primary reflector, such as:

- Width for each row: If on the one hand it must not be too narrow because it could mean a higher number of rows (higher costs due to more gears), on the other, if it is too wide the plant's optical efficiency could be decreased since the sunlight cannot be easily reflected from the last rows. If the width is small, the solar energy captured could be inadequate, whereas in the opposite situation the external rows could have a very low optical efficiency. In a collector with fixed parameters (Tube diameter of 7.5 cm, width mirror of 50 cm and height of the receiver of 7.5 m) the following results in terms of costs per kWe produced by varying the number of rows are obtained [39]:

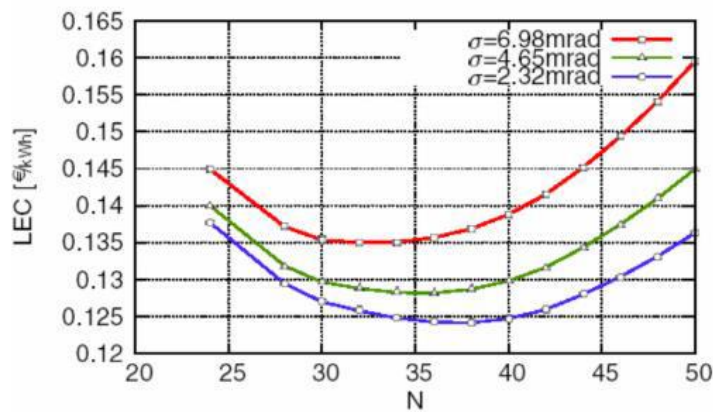


Figure 34: Costs per kWe produced as a function of the number of rows [39].

The lowest cost is obtained with a number of rows of 36 with a sigma of 2.32 mrad which refers to the quality of the mirror.

- The gap between rows: It must not be too large or too small because this can lead to a greater width of the collector (not appropriate in view of the previous consideration) and shading and blocking effects, respectively [39].

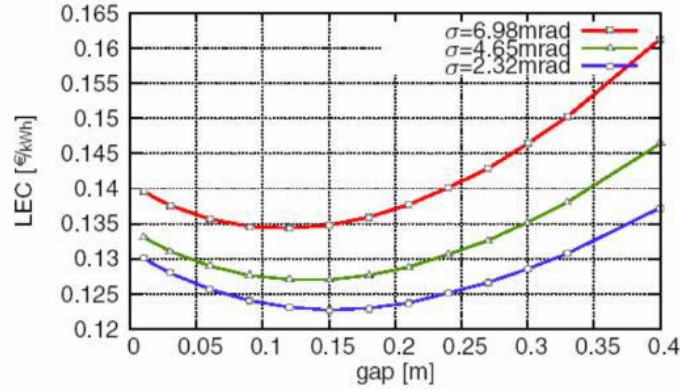


Figure 35: Costs per kWe produced as a function of the gap between rows [39].

- Focus length of the mirrors: It should be very similar to the distance of the mirror from the receiver. Therefore, as discussed in the previous paragraphs even a mild deviation may lead to spillage or local overheating [39].

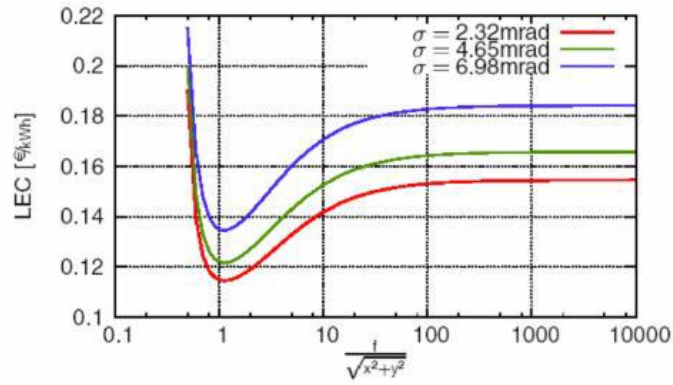


Figure 36: Costs per kWe as a function of the ratio between Focus Length of the mirrors composing a row and its distance from the receiver [39].

4.2.2 Tracking system

The tracking system is another component required within an LFR plant since it enables the tracking of the apparent movement of the sun and therefore, as discussed before, to reduce the different possible optical losses, specifically cosine losses.

Behind the action of the tracking system (by motors), a close loop method is used. It is able to compare after discretization the actual tracking position with the ideal continuous tracking one, therefore if the difference is higher than a fixed value, the mirrors must rotate in order to pursue the motion of the sun in the sky vault. This method is not a perfect one since it relies on a discretized rotation of the mirrors while the solar shift is continuous. There are different types of tracking systems in LFR plants based on the mutualisation of motors. Specifically, either the rows of mirrors are mechanically independent with one motor per row or they are dependent with one motor for a bundle of or a whole set of rows. The first configuration is economically the most expensive but it enables the independence of the mirrors, making cleaning and maintenance easier. The second strategy one is the cheaper one, but if a motor breaks this will lead to shutdown of the plant and mirrors cannot all be flipped together into the same position for cleaning purposes [28].

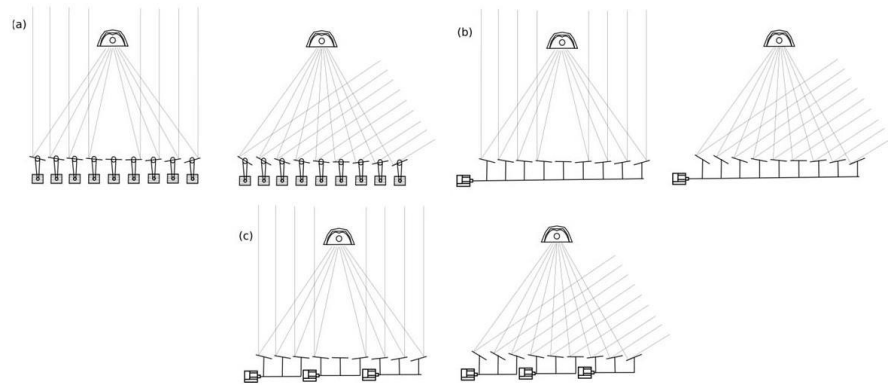


Figure 37: Possible solutions of a tracking system in a LFR plant [28].

4.2.3 Receiver

Above the primary reflector the receiver is placed in the longitudinal direction of the field with the aim of heating up the working fluid. In the most of cases, absorbers are topped with a secondary optic, which is able to redirect the spare solar beams. This is done in order to increase the harvesting by the absorber and to distribute the concentration onto it. Related to a single tubular absorber, the secondary optic may be a U-shaped mirror or a Compound Parabolic Collector (CPC).

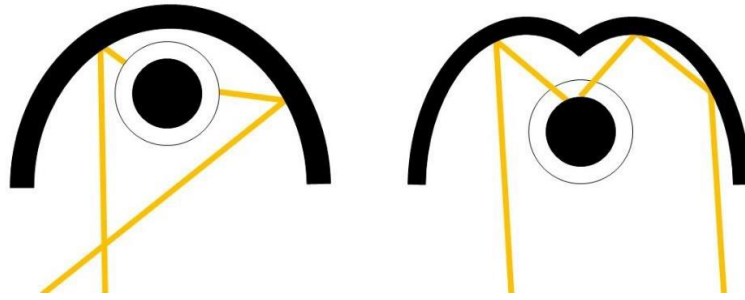


Figure 38: Two possible shape of Secondary Optic [28].

It leads to a lower heat transfer towards the environment since it reduces the forced convection losses and especially the radiative ones as the view factor to the sky vault is limited. A glass vacuum pipe is often installed around the absorber, in order to insulate it. To increase its efficiency, a special coating is applied to enhance the transmittance to the solar spectrum while decreasing reflectivity. The vacuum cuts down the heat conduction losses down [28].

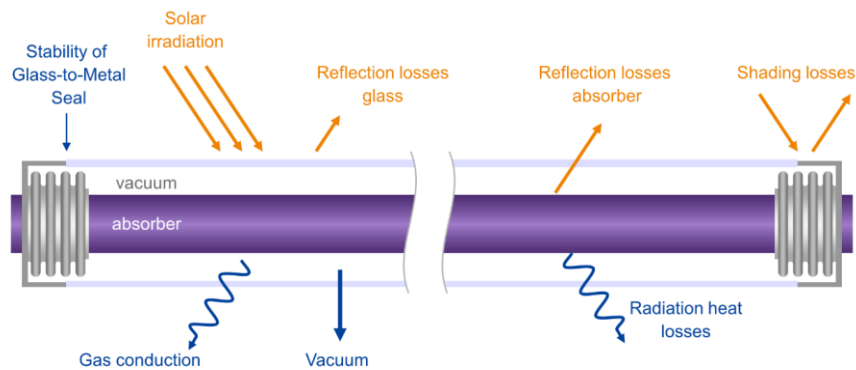


Figure 39: How a vacuum glass tube behaves in terms of heat transfer [28].

The most important part of the receiver is the absorber pipe, which is where the heat received from reflected sunlight is transferred to the working fluid (pressurized water, mineral oil, molten salts...). In most cases, pressurized water is used. Sometimes water is also used for steam generation. The absorber is coated in a special way in order to increase the absorption of low wavelength radiation and to decrease its emission in the infrared region. Absorbers have to withstand high temperatures and, thus, high-pressure levels. The operation of an LFR is usually characterized by the ISO9806 equation as [28]:

$$\frac{\dot{q}_{abs}}{A_{ref}} = \eta_{opt} * IAM(\theta_T, \theta_L) * G_b + \eta_{opt,0} * K_d G_d - c_1 * (T_{HTF} - T_{amb}) - c_1 * (T_{HTF} - T_{amb})^2 - c_5 * \frac{dT_{HTF}}{dt}$$

Where:

- η_{opt} is the global optical efficiency of the reflector,
- A_{ref} is the aperture area of the reflector,
- G_b ($\text{W}\cdot\text{m}^{-2}$) is the DNI,
- K_d is the IAM for diffuse irradiation ($K_d \simeq 0$),
- G_d ($\text{W}\cdot\text{m}^{-2}$) diffuse irradiation,
- c_1 ($\text{W}\cdot\text{m}^{-2}\cdot\text{K}^{-1}$) is the linear heat loss coefficient,
- c_2 ($\text{W}\cdot\text{m}^{-2}\cdot\text{K}^{-2}$) is the quadratic heat loss coefficient,
- c_5 ($\text{J}\cdot\text{m}^{-2}\cdot\text{K}^{-1}$) is effective thermal capacity.

With the previous formula, the thermal power produced by the collector and then absorbed by the working fluid is defined by the sum of heat gains related to direct sunlight evaluated with the optical efficiency of the primary reflector and IAM Incident Angle Modifier (which will be discussed in the next chapters) and thermal losses.

4.3 *Plants modelled within Tonatiuh*

4.3.1 *Existing LFR Plant*

A model of the Fresnel Facility installed at The Cyprus Institute was designed using Tonatiuh (cf. Appendix). All the optically important components of the facility were implemented within the software following the same scales: mirrors, absorber, secondary optic and all shading components such as beams, cover, inlet and outlet tube. All these elements were developed taking into account the optical and geometrical characteristics of the components and also the tracking motion of the mirrors. In the following tables the main important parameters for the design of the existing LFR are presented:

Primary Reflector	
Rows	18
Number of Mirrors per Row	8
Single Mirror Area	0.32 x 4 m ²
Height of Focus Line	4.27541 m

Absorber	
Radius	0.035 m
Length	32.544 m

The plant designed using Tonatiuh is represented in the following picture:

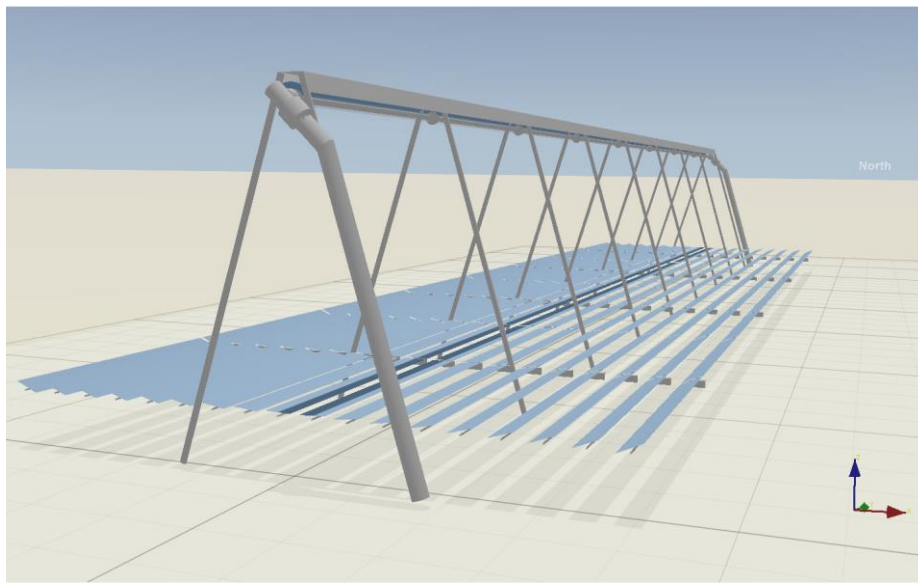


Figure 40: Existing LFR plant created using Tonatiuh viewed from the South.

The receiver is drawn considering all its different parts: Absorber tube, Glass pipes, Flanges, Secondary Reflector and Cover. The Secondary Reflector is developed on the basis of a specific equation evaluated by taking data from the datasheet of the plant (cf. Appendix):

$$y = 26.294 x^4 - 21.347 x^3 + 8.1425 x^2 - 1.54 x - 0.0007$$

In the following image, the receiver is depicted close up:

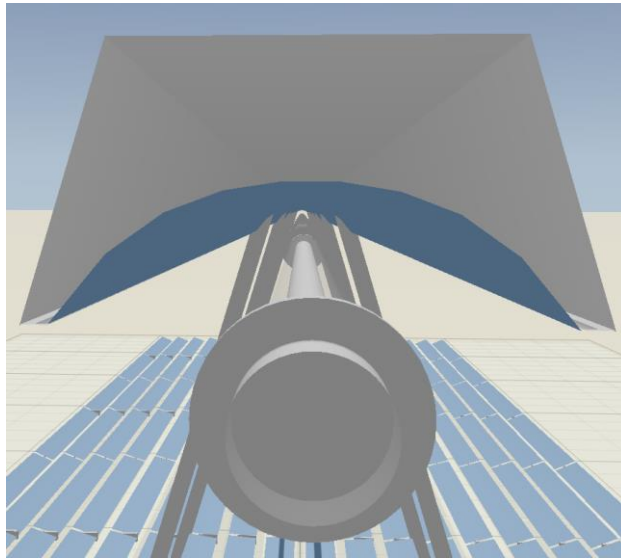


Figure 41: Receiver of the existing LFR plant.

More details about the construction of the existing plant are presented in the Appendix.

4.3.2 LFR Plant with Non-imaging Optics

A second model of the LFR was constructed using Tonatiuh starting from the existing plant but making some important modifications. To be precise, the primary reflector was not modified in terms of the focusing of the mirrors or variations in their dimensions; the main modifications are in the design of the receiver and therefore on the different parts of the plant (for example beams and inlet tubes) connected with it. The receiver itself has a different design from the existing one, as can be seen from the next picture:

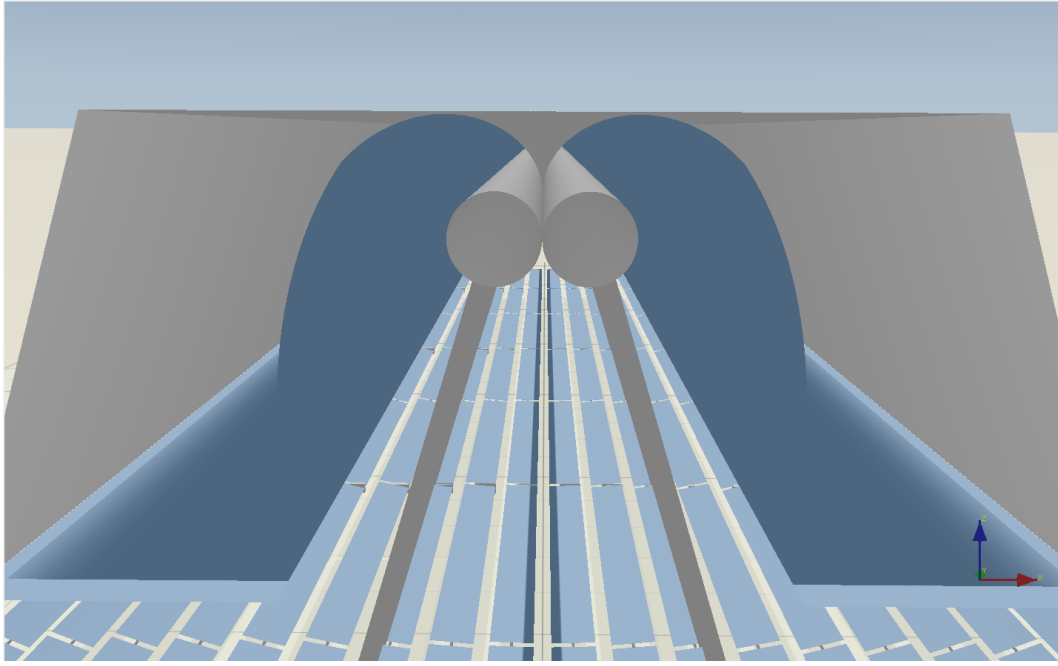


Figure 42: Improved Receiver with Non-imaging Optics.

Instead of one linear absorber tube of 0.035 m radius, there is one U-bent absorber tube of 0.01067 m radius. As the inlet and outlet are located on the same side of the structure, this reduces structural shading. The common inlet and outlet structure is placed on the north-facing side of the plant, leaving the south side without any shading obstacles. It is composed of two symmetric involutes on top and two macrofocal ellipses (MFE) below in order to reflect the spare solar rays to the two absorber pipes. The construction is at the same height but takes into consideration the new size of the receiver. The involutes were constructed using the following equations [40]:

$$X(t) = r (\cos t + (t - a) \sin t)$$

$$Y(t) = r (\sin t - (t - a) \cos t)$$

Where:

- t is a specific angle, which in this case it is used for the range of definition of the Involute,
- a is equal to 90° in our application,
- r is the radius of the pipe.

Proceeding from the extreme bottom point of the involute, the second part of the secondary mirror MFE was evaluated considering the following equations [41]:

$$X(t) = r \sin \vartheta + t \cos \vartheta$$

$$Y(t) = -r \cos \vartheta + t \sin \vartheta$$

Where:

- t is a parametric value obtained from the collector's characteristics.
- r is the radius of the pipe.
- ϑ is the range of the angles used for the definition of the MFE shape.

Therefore, thanks to these equations the shape of the secondary mirror was built by symmetry. Consequently, the cover composed of two oblique sides and one horizontal side (trapezium), was designed in order to be compact as much as possible with the new secondary optics. The most important aspect is the focus height, which is the same as the previous one (4.2751m) but now corresponds to the aperture centre and not to the height of the absorber. The structural beams have been adapted to the new cover and aperture. In the next picture, the entire plant with the optimized receiver is shown:

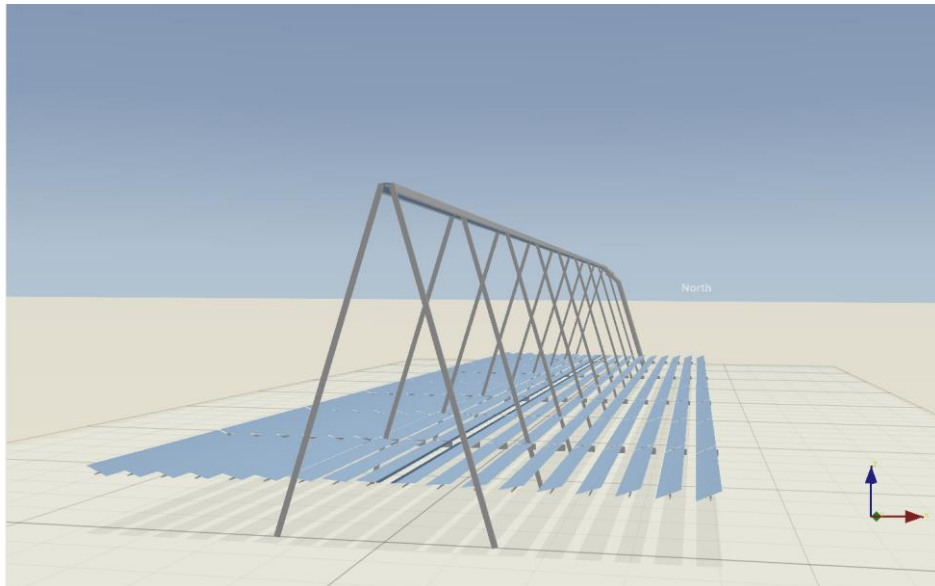


Figure 43: LFR plant with optimized receiver with non-Imaging Optics viewed from the South.

5. *Direct Solar Energy in Nicosia*

This fifth chapter of the thesis describes the incoming solar energy received at the Cyprus Institute where the LFR plant has been installed, in order to show the available energy considered as the input for the energy assessment, which will be performed in Chapter 6.

5.1 *Solar Energy Measurement*

To assess the solar energy received at a specific place on Earth three different parameters can be utilized:

- The DNI [W/m^2], Direct Normal Irradiance, is the amount of solar radiation received per unit area by a surface that is always held perpendicular to the rays that come from the sun at its current position in the sky.
- The DHI [W/m^2], Diffuse Horizontal Irradiance, is the radiation at the Earth's surface from light scattered by the atmosphere. It is measured on a horizontal surface with radiation coming from all points in the sky excluding the radiation from the sun's disk.
- The GHI [W/m^2], Global Horizontal Irradiance, is the amount of direct and diffuse solar radiation received per unit area of an horizontal surface.

As discussed before, for CST installations only DNI is considered, as the diffused light cannot be concentrated. Therefore, the measurement of DNI is required for these systems. For that purpose, on the roof of the NTL at The Cyprus Institute a pyrliometer has been installed which is able to measure DNI each second, tracking the path of the sun.



Figure 44: LP Pyrheliometer 16 AC placed at The Cyprus Institute.

DNI is represented in the next figure for three different days in 2019 (Winter Solstice, Summer Solstice, Autumn Equinox):

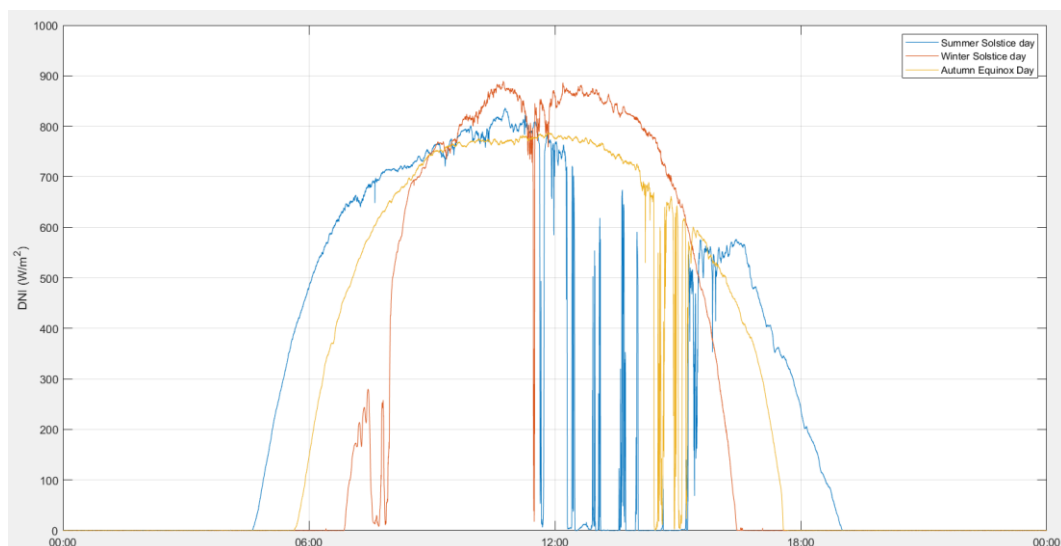


Figure 45: DNI plotted during Summer Solstice, Winter Solstice and Autumn Equinox.

While the duration of the day varies through the year, DNI peaks were close. During the summer solstice, clouds appeared in the afternoon, and the DNI falls to zero. Although global solar radiation might not have been zero, DNI was so low and CST technology systems would not work unlike PVs. The amount of energy received at the Cyprus Institute measured by the pyrheliometer during the entire year 2019 was 1951.4 kWh/m² (the coding script for its calculation is in Appendix “6.1 DNI Energy Yearly Plot”).

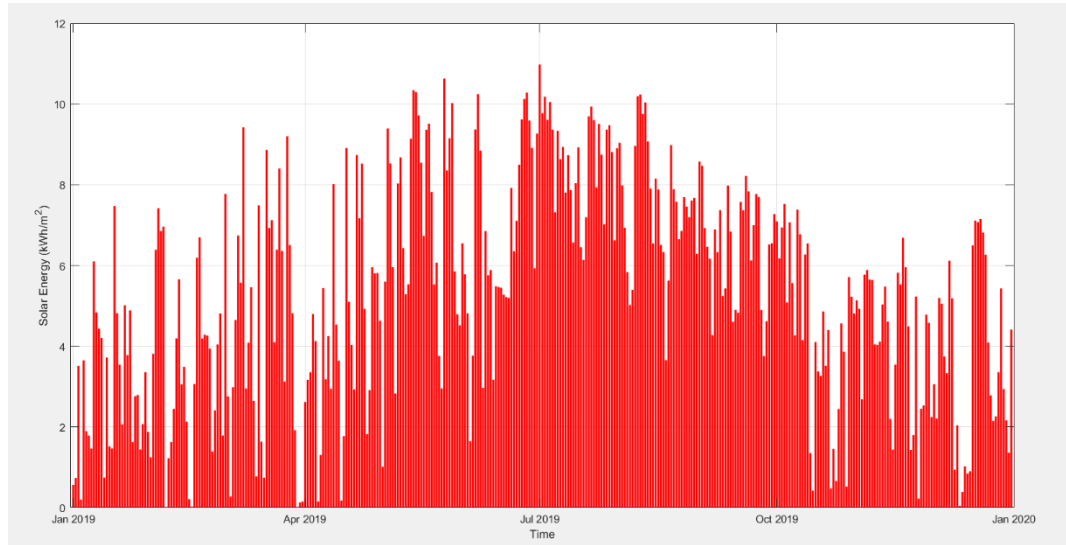


Figure 46: Daily Solar Energy at The Cyprus Institute.

From the previous chart, it can be observed that in winter incoming solar energy is lower than in summer, due to the presence of more cloudy days and for a shorter duration during the days. As expected in Cyprus, the higher density of sunny days in summer is highlighted by the scarcity of “white gaps”, in contrast with the rest of the year. The next graph shows the average daily energy available per month during the year 2019:

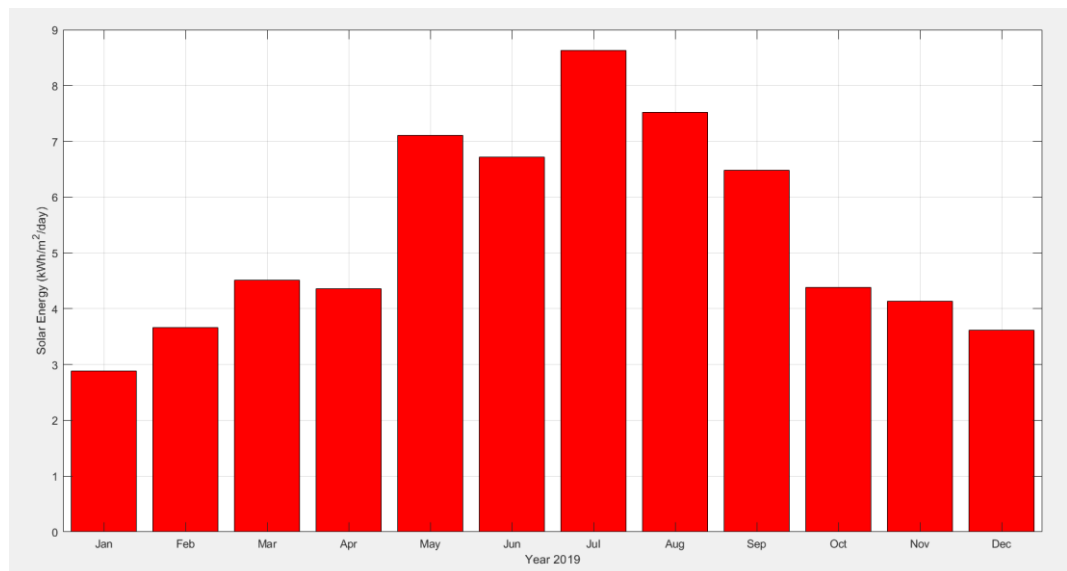


Figure 47: Average Daily Solar Energy per month at the Cyprus Institute.

Therefore, as suggested by the last chart, the daily average of solar energy achieved is higher in the summer months than in the winter for the reason discussed above. In summer, the daily average is less than half of the winter one. Considering the energy resource available, the next sections will focus on the conversion potential of this energy by the existing collector and also with potential upgrades.

6. Method to compute IAM values using Tonatiuh++

6.1 Incidence Angle Modifiers

From the energy equation in Chapter 4 (cf. 4.2.3 Receiver), the Incidence Angle Modifier (IAM) indicates the optical efficiency of the facility and therefore it is possible to evaluate the incoming solar energy that may be absorbed and transferred to the HTF. The IAMs are factors that are used in order to determine the optical efficiency of a system for a given position of the sun, accounting for all losses from the aperture area of the reflector up to the outer surface of the absorber. The IAMs allow the evaluation of the optical efficiency for a given position of the sun defined by the transversal angle θ_T and longitudinal angle θ_L . They are defined as the projections of the solar elevation on the longitudinal plane (north – south axis) and transversal plane (west – east axis). The global $IAM(\theta_L, \theta_T)$ value is sometimes approximated by:

$$IAM(\theta_L, \theta_T) = IAM_T(0, \theta_T) \cdot IAM_L(\theta_L, 0) \quad [1]$$

At zenith, θ_L and θ_T are equal to 0° . The following figure shows these two angles for a specific sun position:

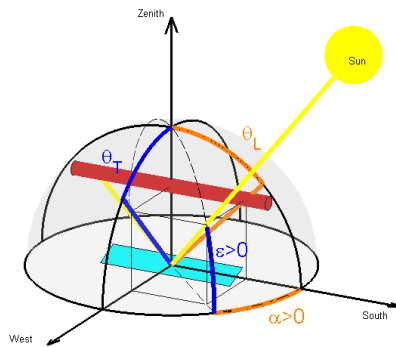


Figure 48: Representation of how the sun position could be expressed.

The optical efficiency $\eta_{opt,0}$ is reached when the sun is at azimuth ($\theta_L=\theta_T=0^\circ$). It is defined by the ratio:

$$\eta_{opt,0} = \frac{\dot{q}_{inc}}{G_b \cdot A_{ref}} \quad [2]$$

Where:

- \dot{q}_{inc} is incoming power [W] reflected by the primary optic of area A_{ref} and reaching the absorber outer surface.
- G_b is the Direct Normal Irradiance (DNI) [$\text{W}\cdot\text{m}^{-2}$].

This value approximates the proportion of energy possible to be absorbed, compared to the energy received by the surface of the mirrors when the sun is at zenith. Considering that during the day the sun changes its position, IAMs are needed to understand how the LFR works (or a solar technology in general). One major aim of this thesis is to study the optical efficiency of the existing facility and to compare it to the efficiency obtained with the LFR improved with Non-imaging Optics. Therefore, the IAMs for all possible combinations of angles were determined with the use of a Monte Carlo ray tracing simulation software, Tonatiuh++, currently under development at the Cyprus Institute (CyI).

6.2 *The Tonatiuh++ Process*

The following figure displays the rays sent on the modelled LFR at CyI with tracking mirrors:

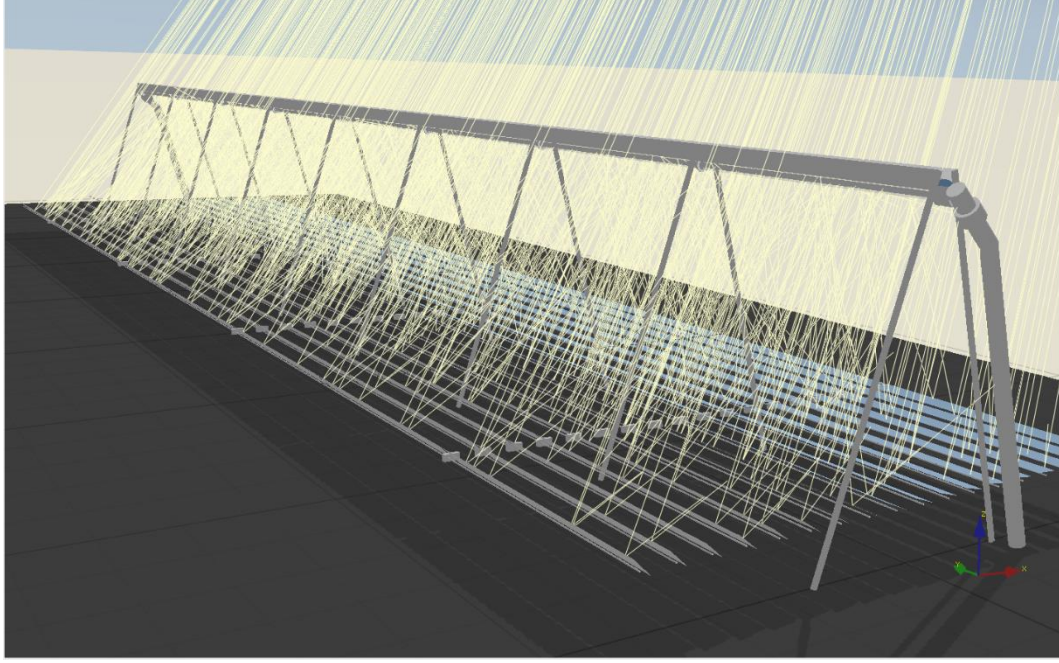


Figure 49: General view of the LFR at CyI with Tonatiuh++ with solar Azimuth of 60° and Elevation of 45°.

To perform the IAMs calculation, the absorber must be studied in terms of the flux received from the reflection of the primary reflector. On Tonatiuh++, specifically in the Environmental settings section, DNI is set to $1 \text{ W} \cdot \text{m}^{-2}$, to permit normalization in the post-processing, especially for the calculation of $\eta_{opt,0}$. Therefore, firstly, it is necessary to evaluate this parameter in order to understand how the system works at the sun's zenith position. Once $\eta_{opt,0}$ determined, IAM are calculated as the ratio between the power received on the absorber for a given (θ_L, θ_T) and the power received at zenith :

$$IAM(\theta_L, \theta_T) = \frac{\dot{q}_{inc}(\theta_L, \theta_T)}{\dot{q}_{inc}(0^\circ, 0^\circ)} \quad [3]$$

In the next paragraphs the scripts used in the two plants to deploy the related calculations are presented.

6.2.1 Ray Tracing Analysis for the Existing LFR plant (ASB).

Firstly, an introduction to the script written within the coding section of Tonatiuh++ for the optical analysis of the existing LFR plant (As Built, ASB) is presented. The script includes two different parts. The first one is presented in the next figure:

```
1 //Loop for obtaining eta_0
2 printTimed("azimuth [deg], elevation[deg], efficiency");
3 var alpha      = 90;
4 var gamma      = 180;
5 var sp = NodeObject().getScene().getPart("world.sun.position");
6 sp.setParameter("azimuth", gamma);
7 sp.setParameter("elevation", alpha);
8 var wmax      = tn.FindInterception("//RootNode/Fresnel_CYI/Receiver/Absorber/Shape", 10000000);
9 print(" " + wmax/184.32);
```

Figure 50: Script run for achieving the optical efficiency of LFR at zenith.

Variables “alpha” and “gamma” are respectively the elevation and azimuth angles of the sun. The first part is used for the calculation of the power received by the absorber when the sun is at zenith with the use of “FindInterception” function that looks for the number of rays received by a specific node with a certain number of rays sent. As the set DNI is $1 \text{ W}\cdot\text{m}^{-2}$, it renders the equivalent useful area of the primary reflector area. When divided by the real surface of the primary reflector, the value obtained is 0.709. In the second part, the calculation of the IAM for the other positions in azimuth and elevation are performed:

```
11 // Loop for the solar positions
12 var sg=1; //Degree for step for Azimuth
13 var sa=1; //Degree for step for Elevation
14 var totstep=(270-180)/sg+1; //Total Number of steps.
15 for (var gamma = 180; gamma <= 270; gamma += sg)
16 {
17   for (var alpha = 0; alpha <= 90; alpha += sa)
18   {
19     // set azimuth and elevation of the sun in degrees
20     var sp = NodeObject().getScene().getPart("world.sun.position");
21     sp.setParameter("azimuth", gamma);
22     sp.setParameter("elevation", alpha);
23
24     // find power intercepted by a node using a given number of rays
25     var w = tn.FindInterception("//RootNode/Fresnel_CYI/Receiver/Absorber/Shape", 10000000);
26     var IAM = w/wmax;
27     print(" " + gamma-180 + " , " + alpha + " , " + IAM);
28   }
29   //print(" " + ((gamma-180)/sg+1)/totstep*100);
30 }
```

Figure 51: Second Part of the Script run for achieving the IAM.

Starting from the definition of the angle variation at each step and the total number of steps, two “for” loops are generated. Specifically, in azimuth and in elevation (namely “gamma” and “alpha”), they are evolving from South to West and from 0° to 90° , respectively. 91×91 steps are therefore required. The “FindInterception”

function is used to extrapolate the power received by the absorber according to the specific position of the sun within the loop and then it is compared to the power achieved at zenith. Considering that huge number of steps, the simulation requires a large computational capacity, as the number of rays sent per step is 10^7 . This specific number of rays was obtained after a convergence analysis (cf. 7.2.1 *Convergence Analysis on ASB plant*), where the convergence of output data was studied for each specific sun position. After the simulation of the second part of the proposed script, the results are achieved in 3 columns as set out in the script with the function “print(“....”)” :

Azimuth	Elevation	IAM
0	0	0
0	1	0
0	2	0
0	20	0.104791034
0
0	90	1.000433861
1	0	0
1
1	90	0.998863652
...
.....
.....
90	90	0.999157861

The IAMs in the third column are the results of the calculation for a given pair of azimuth and elevation. A transformation is required to express them as a function of θ_L and θ_T .

6.2.2 Ray Tracing Analysis for the improved LFR plant with NIO.

Here the script written to calculate the optical analysis of the improved LFR plant with non-Imaging Optics (NIO) is introduced. It is similar to the previous one since it has the same purpose. Actually, considering that the “FindInterception” function works with only one node and in this “new” design of absorber, there are two nodes to consider (the two parts of the U-bend), this specific function must be called twice. Similarly, optical efficiency at zenith is calculated in the first part of the script and IAMs values determined in the second:

```

1 //Loop for obtaining eta_0
2 printTimed("azimuth [deg], elevation[deg], efficiency");
3 var alpha = 90;
4 var gamma = 180;
5 var sp = NodeObject().getScene().getPart("world.sun.position");
6 sp.setParameter("azimuth", gamma);
7 sp.setParameter("elevation", alpha);
8
9 var wmax1 = tn.FindInterception("//Node/Fresnel_CYI/Receiver/Absorber1/Shape", 10000000);
10 var wmax2 = tn.FindInterception("//Node/Fresnel_CYI/Receiver/Absorber2/Shape", 10000000);
11 var wmax = wmax1+wmax2;
12 print(" " + wmax/184.32);
13
14 // Loop for the solar positions
15 var sg=30; //Degree for step for Azimuth
16 var sa=30; //Degree for step for Elevation
17 var totstep=(270-180)/sg+1; //Total Number of steps.
18 for (var gamma = 180; gamma <= 270; gamma += sg)
19 {
20   for (var alpha = 0; alpha <= 90; alpha += sa)
21   {
22     // set azimuth and elevation of the sun in degrees
23     var sp = NodeObject().getScene().getPart("world.sun.position");
24     sp.setParameter("azimuth", gamma);
25     sp.setParameter("elevation", alpha);
26
27     // find power intercepted by a node using a given number of rays
28     var w1 = tn.FindInterception("//Node/Fresnel_CYI/Receiver/Absorber1/Shape", 10000000);
29     var w2 = tn.FindInterception("//Node/Fresnel_CYI/Receiver/Absorber2/Shape", 10000000);
30     var w = w1+w2;
31     var IAM = w/wmax;
32     print(" " + gamma-180 + ", " + alpha + ", " + IAM);
33   }
34   //print(" " + ((gamma-180)/sg+1)/totstep*100);
35 }

```

Figure 52: Script run for achieving the optical efficiency and the IAM for the improved LFR plant.

The efficiency η_0 calculated with NIO is 0.76055. This constitutes an important improvement compared to the 0.709 with the ASB solution. The number of rays sent is the same as in the previous study, since the convergence analysis performed in that plant gave the same value (cf. 7.2.2 *Convergence Analysis on NIO plant*). The output results are given by the script in the same way, and therefore for 91x91 steps for the different positions of the sun.

6.3 Matlab Processing

The conversion from azimuth and elevation angles into longitudinal and transversal angles is as follows:

$$\theta_T = \tan^{-1} \left(\frac{\cos \varepsilon \cdot \sin \gamma_s}{\sin \varepsilon} \right) \quad [4]$$

$$\theta_L = \tan^{-1} \left(\frac{\cos \varepsilon \cdot \cos \gamma_s}{\sin \varepsilon} \right) \quad [5]$$

In that formulas ε and γ_s are respectively the elevation and azimuth angles. The IAMs are represented by a graph using a script developed in Matlab with the following script:

```

%% Reading of Excel File of the Results
filename = 'IAM_RESULTS.xls';
M=xlsread(filename);
M(1,:)=[];
%% Conversion of the Azimuth and Elevation into Longitudinal and
Transversal Angles and Pre-Allocation in vectors.
x = (atand(cosd(M(:,2)).*cosd(M(:,1))./sind(M(:,2)))); %Theta_L
y = (atand(cosd(M(:,2)).*sind(M(:,1))./sind(M(:,2)))); %Theta_T
z=M(:,3); %IAM
%% Definition of the matrix with a Data Pre-Processsing phase.
h=[x y z];
h =h( ~any( isnan( h ) | isinf( h ), 2 ),: );
[C,ia,ic]=unique(h(:,1:2),'rows');
h =h(ia,:);
x=h(:,1);
y=h(:,2);
z=h(:,3);
%% Definition of the function from the data acquired
F = scatteredInterpolant(x,y,z);
[xq,yq] = meshgrid(0:1:90);
vq = F(xq,yq);
%% Plot of the IAMs depending on Theta_L and Theta_T
surf(xq,yq,vq);
grid on
colormap(jet(256));
colormap;
ylabel ('Transversal angle (\theta_{T}^{\circ})')
xlabel ('Longitudinal angle (\theta_{L}^{\circ})')
colorbar('eastoutside')
view(2)
xlim([0 90])
ylim([0 90])
zlim([0 1.2])

```

After the file reading, the conversion is performed using the equations [4] and [5]. Subsequently, three column vectors are embedded with the matrix “h”, which is subjected to a Data Pre-Processing step where the infinities, non-solutions or repeated values are deleted. A new matrix “vq” of 3 columns and 91x91 of lines is created using the function “scatteredInterpolant”. Each value of θ_L and θ_T between 0° and 90° , with a step of 1° , corresponds to one value of IAM. This function allows the reshuffling of IAMs acquired with Tonatiuh++. Therefore, the matrix h is used to extract the function.

6.4 Results of the IAM Analysis.

6.4.1 IAMs and Energy received by the existing LFR plant (ASB)

The graph of the IAM values for the existing LFR plant as a function of θ_L and θ_T is represented:

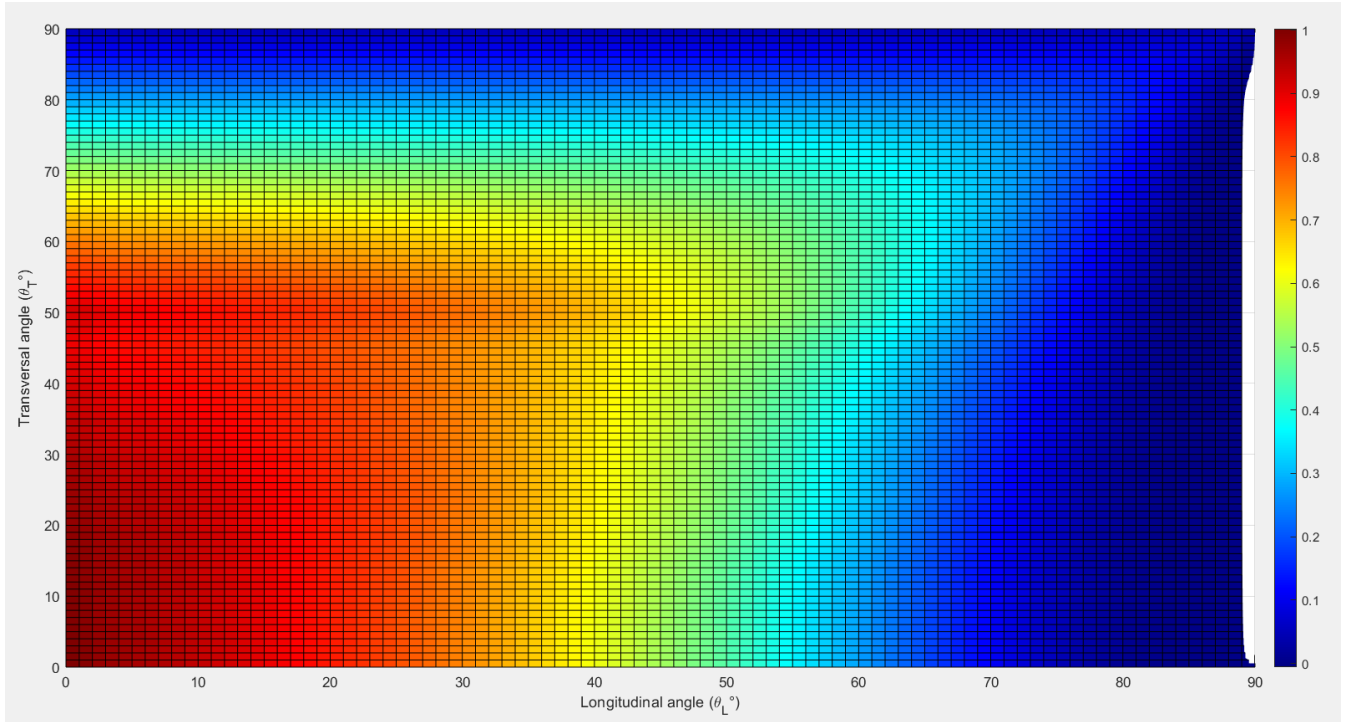


Figure 53: IAM values depending on longitudinal and transversal angle for the existing LFR plant.

Figure 53 helps to understand how the LFR works in terms of optical performance. As can be seen, the IAMs values are very close to 1 when the angles are very close to 0, due to the fact that in these conditions the sun is very near to the zenith. Conversely, when the sun's position changes from the zenith, the IAM decreases and thus optical efficiency as well.

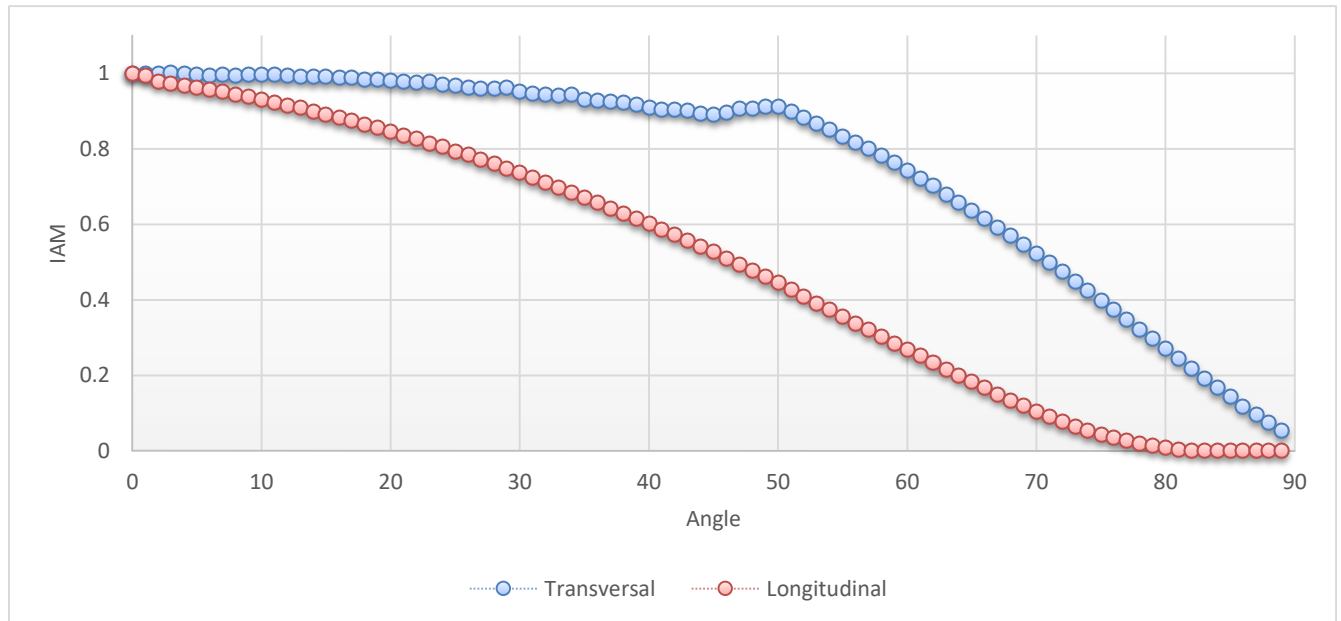


Figure 54: Transversal and Longitudinal IAM for ASB plant.

The IAM is affected mainly by the variation in the longitudinal angle, since fixing 0° of the longitudinal angle, the IAM starts to decrease only after 65 degrees of the transversal angle, whereas fixing 0 degrees of the transversal angle, after 40 degrees of the longitudinal angle it begins to fall to lower values. Actually, the main loss in the variation of the longitudinal angle is the end effect resulting from the partial disuse of the absorber (cf. Chapter 7 Flux Analysis). By contrast, when the transversal angle varies the main losses are the blocking and shading occurring between the mirrors and, for a low transversal angle, the shading of the receiver onto the primary reflector is by no means negligible. In this way, the function that correlates the angles (Longitudinal and Transversal ones) with the IAM is obtained. The same Matlab script was used to process the DNI and the IAM per year, with a time step of 1s (cf. Appendix 6.1 *DNI Energy Yearly Plot*). Following the acquisition and the cleaning processes of the DNI data, a matrix of 7 columns was created. The number of lines, n , corresponds to the number of DNI records. The first 6 columns correspond, in order, to the year, month, day, hour, minute and second. The 7th column corresponds to the DNI records. Afterwards, the DNI can be weighted with the IAM values at a given time of the recording. In the following graphs, the energy absorbed by the receiver is represented and compared with the available energy at The Cyprus Institute outlined in Chapter 5:

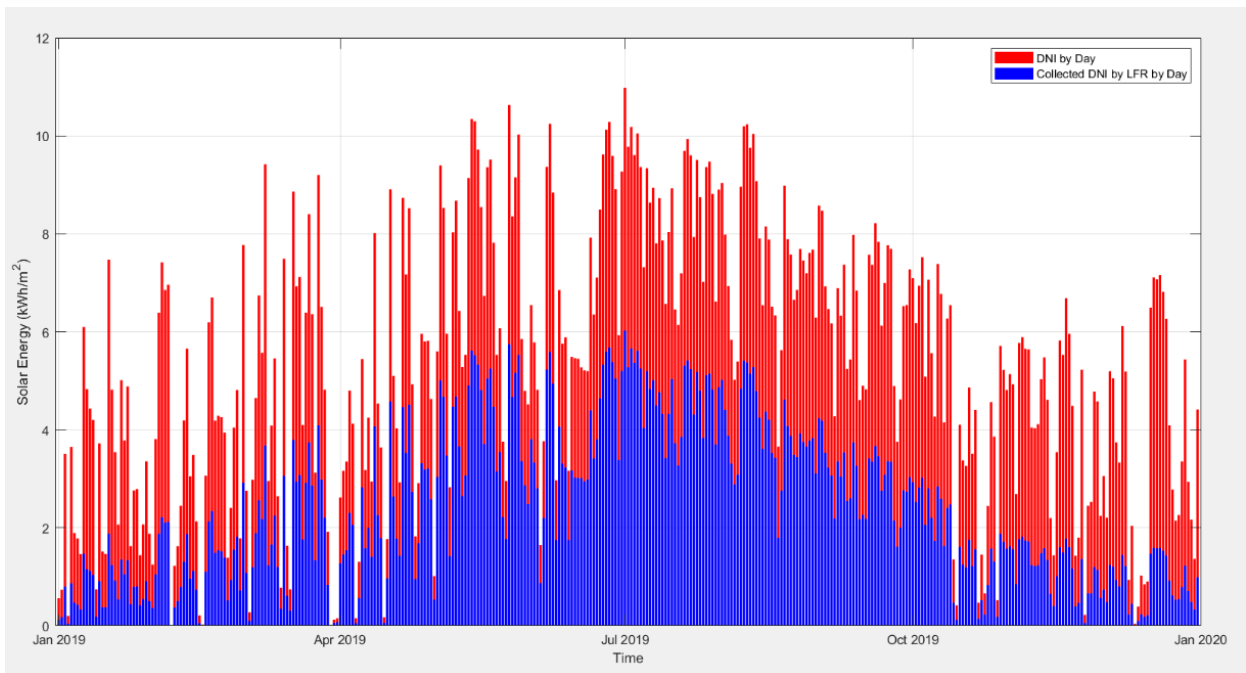


Figure 55: DNI available by day vs Energy collected by the Receiver of the existing LFR by day.

As seen in Chapter 5, the available energy is $1951.4 \text{ kWh}\cdot\text{m}^{-2}$ and after applying the IAMs weighting, $890.22 \text{ kWh}/\text{m}^2$ are possibly collectable by the Fresnel. Therefore, from the annual DNI yield, 45% may be reused. Obviously, two different factors determine the amount of the energy received by the absorber of the LFR:

- The DNI available: as seen in Chapter 5, daily DNI is higher in summer.
- Optical efficiency: which depends on the solar angles during the year, especially the elevation.

This last aspect is underlined in the next graph where, in addition to the daily average DNI and the collectable one, the optical efficiency of the LFR is represented:

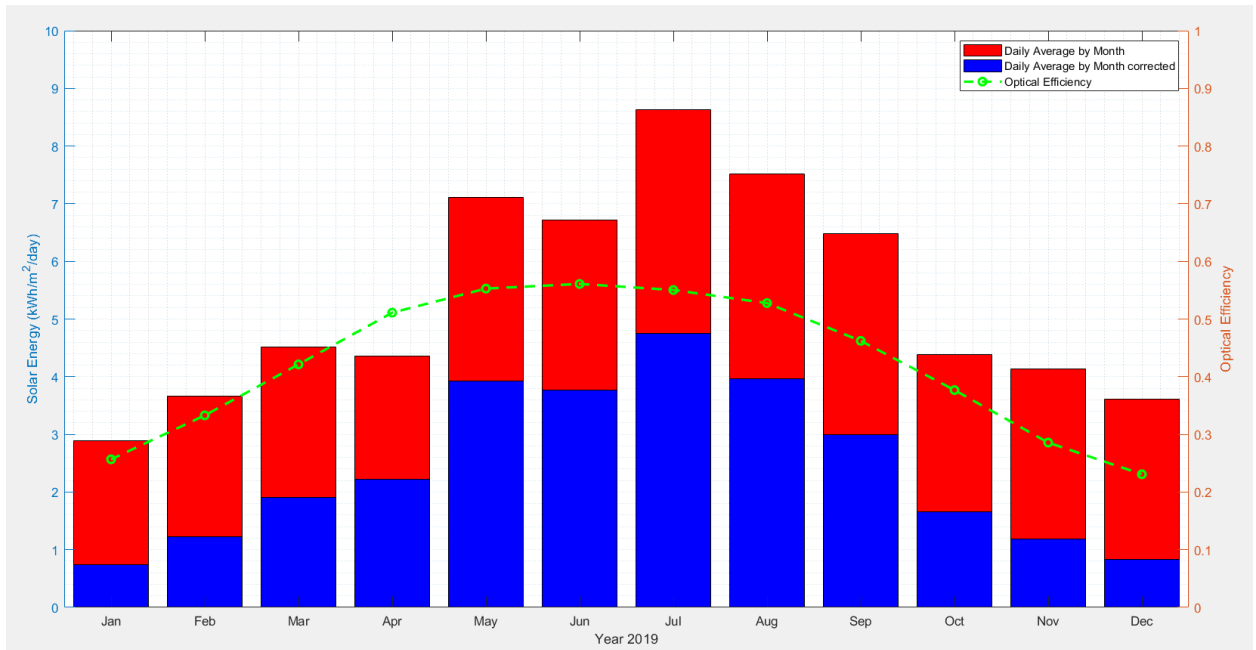


Figure 56: Daily average available and collectable energies (left axis) and corresponding optical efficiency of the existing LFR (right axis).

As previously seen, the daily average DNI energy is higher in summer, reaching almost $9 \text{ kWh}/\text{m}^2$, and with $5 \text{ kWh}\cdot\text{m}^{-2}$ of received energy on the absorber. The situation is not so favourable in winter: a little below $3 \text{ kWh}\cdot\text{m}^{-2}$ in January and with a lower efficiency (less than $1 \text{ kWh}\cdot\text{m}^{-2}$ of energy reached the receiver). Efficiency

varies between 26% in winter and 56% in summer.

6.4.2 IAMs and Energy received by the upgraded LFR plant (NIO)

IAM values with the upgraded optics are illustrated:

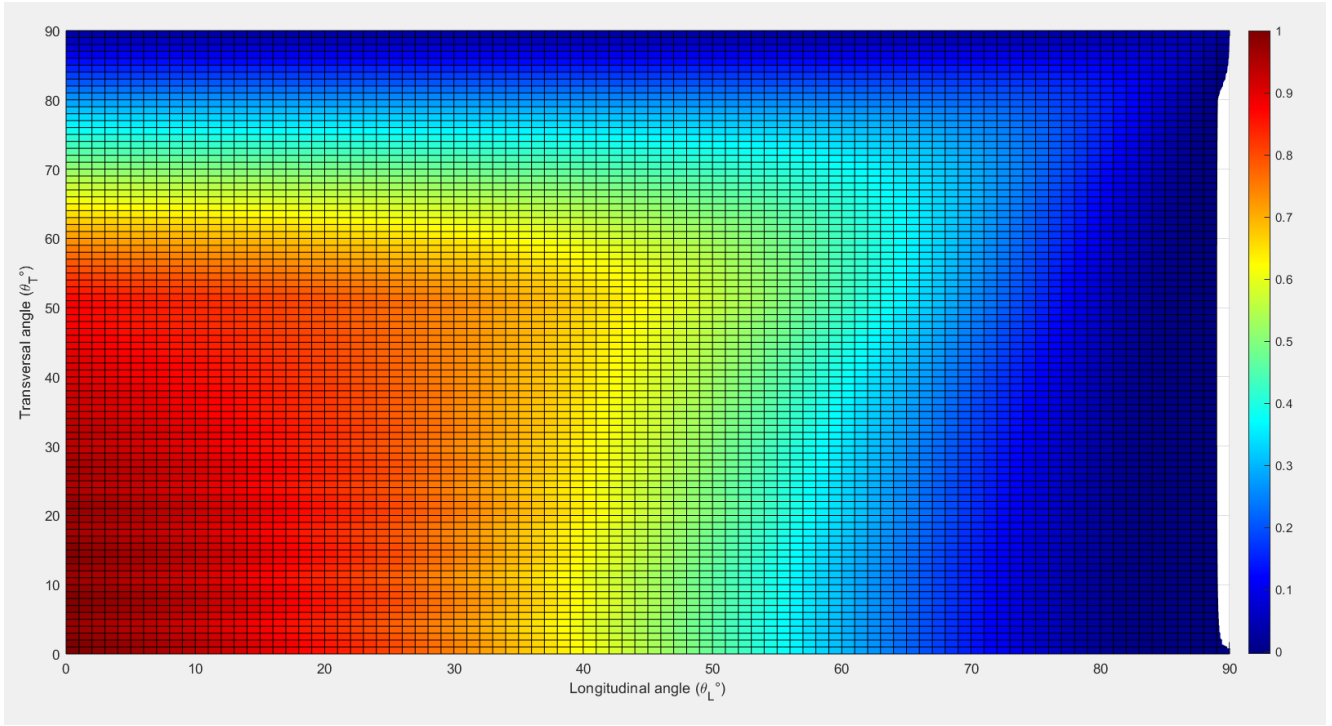


Figure 57: IAM values depending on longitudinal and transversal angles for the upgraded LFR plant.

The plot is similar to the previous one; indeed, the same aspects in terms of IAM variation as the longitudinal and transversal angles can be observed. The optical performance of the upgraded plant with non-Imaging Optics compared with the existing plant is illustrated in the following plot:

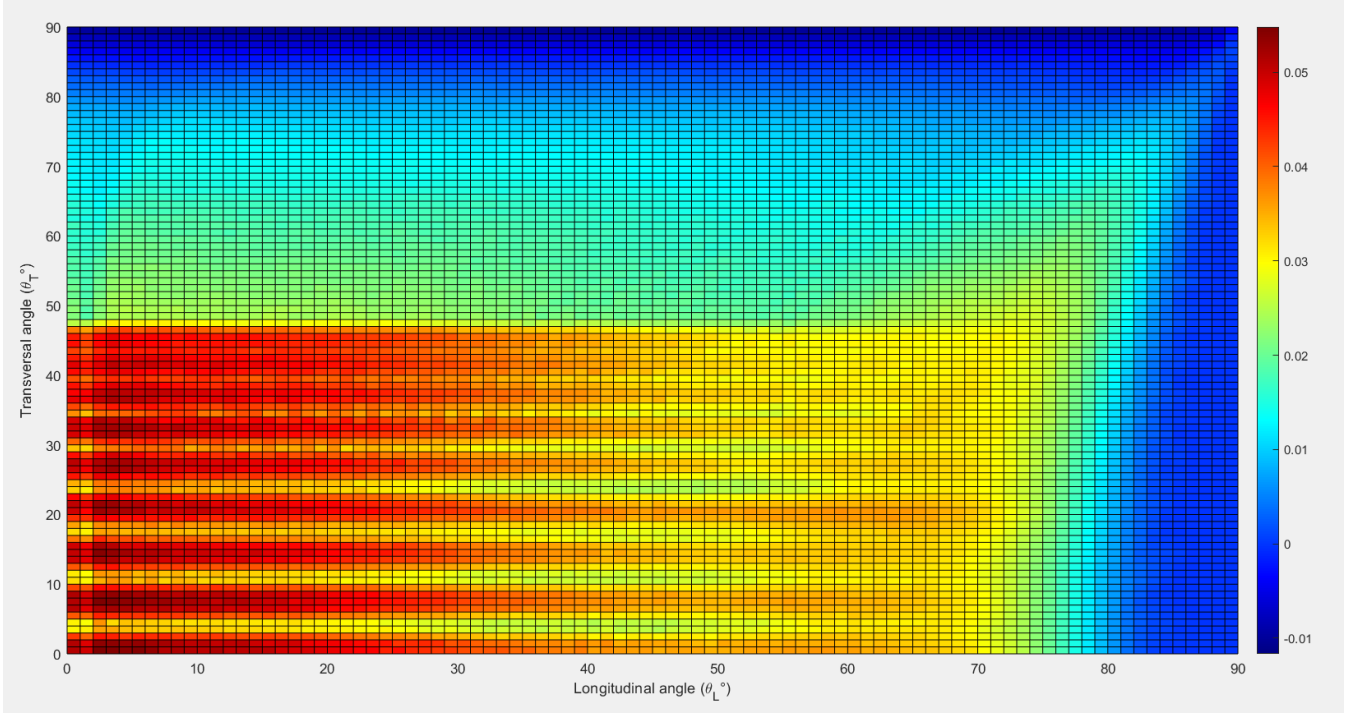


Figure 58: Difference between the IAM achieved with the NIO plant compared to the existing plant.

The previous graph plots the difference between the IAMs obtained with the upgraded plant (NIO) and the existing plant (ASB) after weighting them with their respective efficiencies $\eta_{opt,0}$. The NIO performance is generally better. Indeed, this enhancement is maximum when the sun heads toward zenith, due to the higher $\eta_{opt,0}$ for the NIO plant. The ASB plant works better compared to the NIO one only for very high transversal and longitudinal angles where solar elevation is low. The “zebra” behaviour is due to the lower shading effect of the NIO receiver between the rows. Out of $1951.4 \text{ kWh}\cdot\text{m}^{-2}$, $945.63 \text{ kWh}\cdot\text{m}^{-2}$ may be collected with the NIO LFR, therefore 48% of the DNI available. In the following graphs, the total solar and collectable energies are plotted:

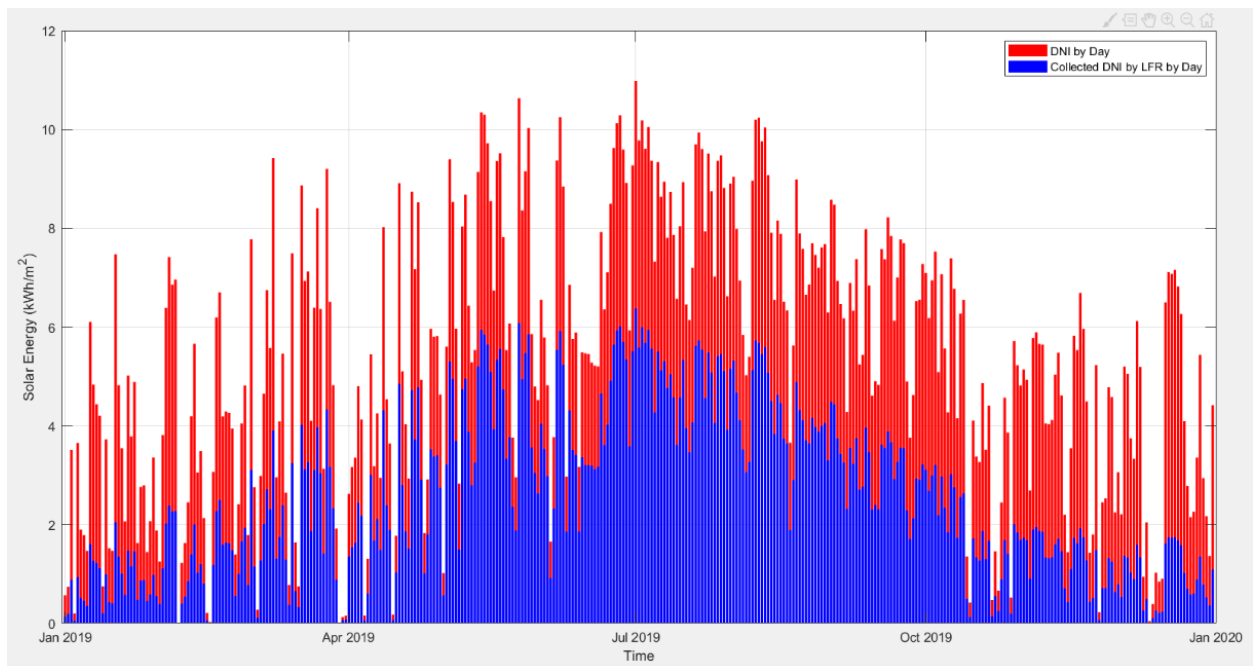


Figure 60: DNI available by day vs Energy collected by the Receiver of the improved LFR by day.

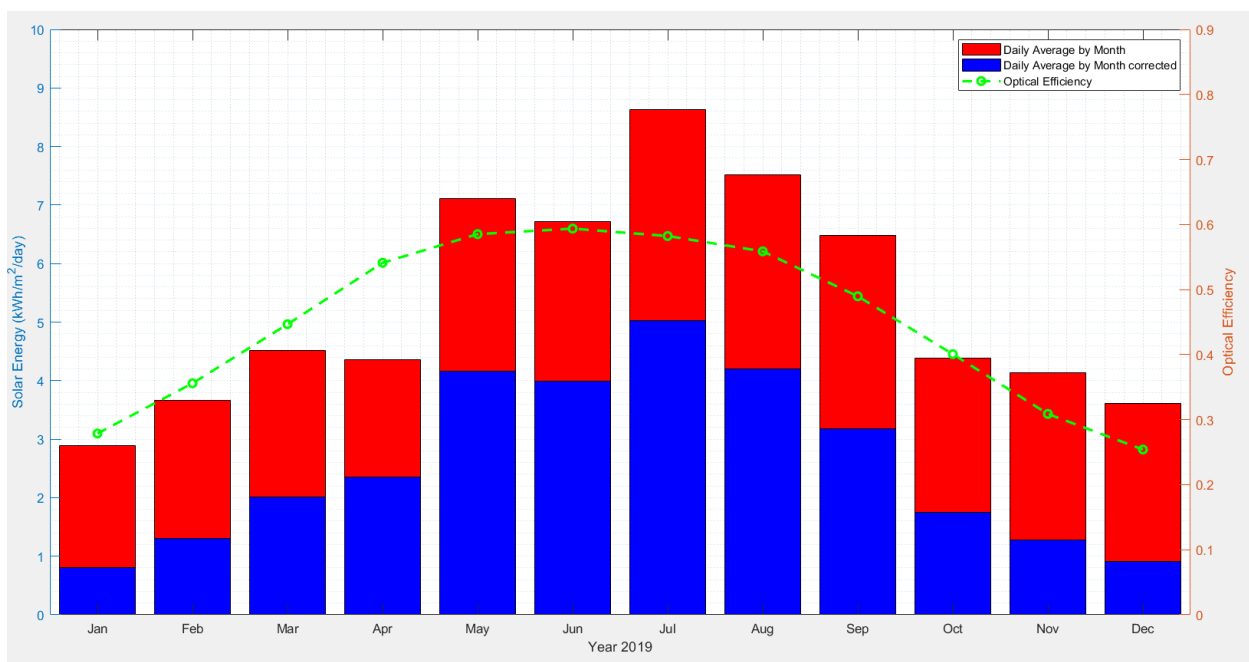


Figure 59: Daily average available and collectable energy (left axis) and optical efficiency of the upgraded LFR (right axis).

Compared to the existing plant, the improved LFR is able to collect 3% more of the available solar energy. Therefore, there is a very small difference in the energy assessment, which is attested by the previous and next charts, which are almost identical to the previous ones for the existing LFR plant. As expected, the

efficiencies are slightly improved thanks to 59% and 27% acquired respectively in summer and in winter.

6.4.3 IAMs and Energy received by the improved LFR plant with insertion of glass surface in the aperture of the receiver.

Paragraph 4.3.2 contains a description of the improvements made to the existing LFR plant at The Cyprus Institute, which illustrates the main important differences. Here in this paragraph, a modification of the improved LFR plant with Non-Imaging Optics (NIO) is introduced, involving the inclusion of a flat glass surface at the aperture of the receiver, placed at 4.2754 m above the ground. The insertion of a flat glass surface is needed to prevent the presence of dust at the U-shaped absorber and Non-Imaging Optics since they can be difficult to clean. Actually, in the existing LFR plant, the absorber is kept under vacuum to reduce thermal losses (cf. 4.2.3 Receiver). Here, in the LFR with Non-Imaging Optics (NIO), a surface glass with a thickness of 3mm is placed in the aperture of the receiver but not under vacuum, as shown in the following figure:

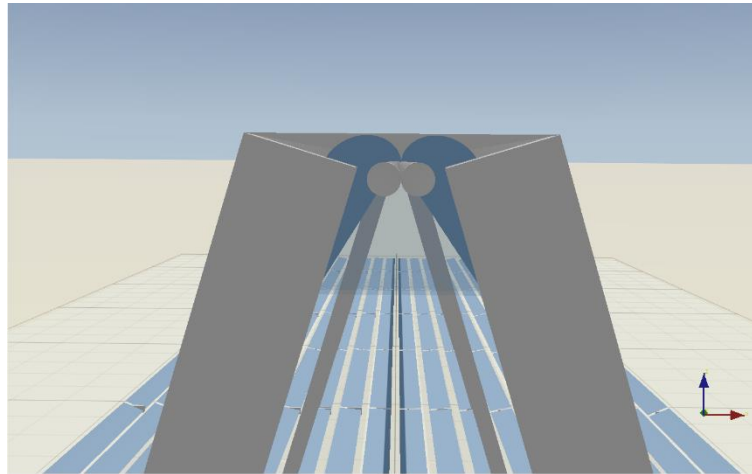


Figure 61: Modification of the improved LFR with NIO with the glass surface in the aperture.

This minor modification generates new losses, although it helps to control soiling by easing cleaning operations. Indeed, part of the reflected rays from the primary optics are either reflected or absorbed. The new IAMs are accordingly plotted as follows:

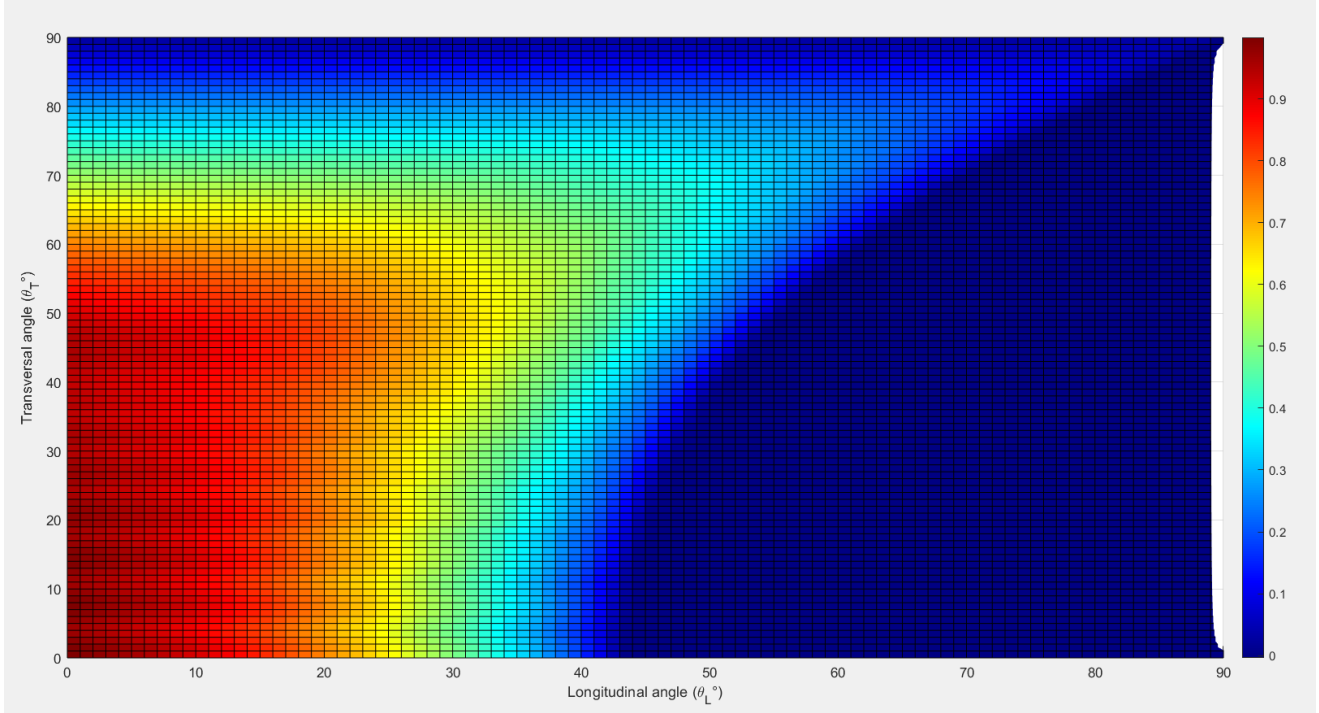


Figure 63: IAM values depending on longitudinal and transversal angle for the upgraded LFR plant (NIO) with glass surface at the aperture.

The comparison between NIO and NIO with glass is illustrated in the next figure:

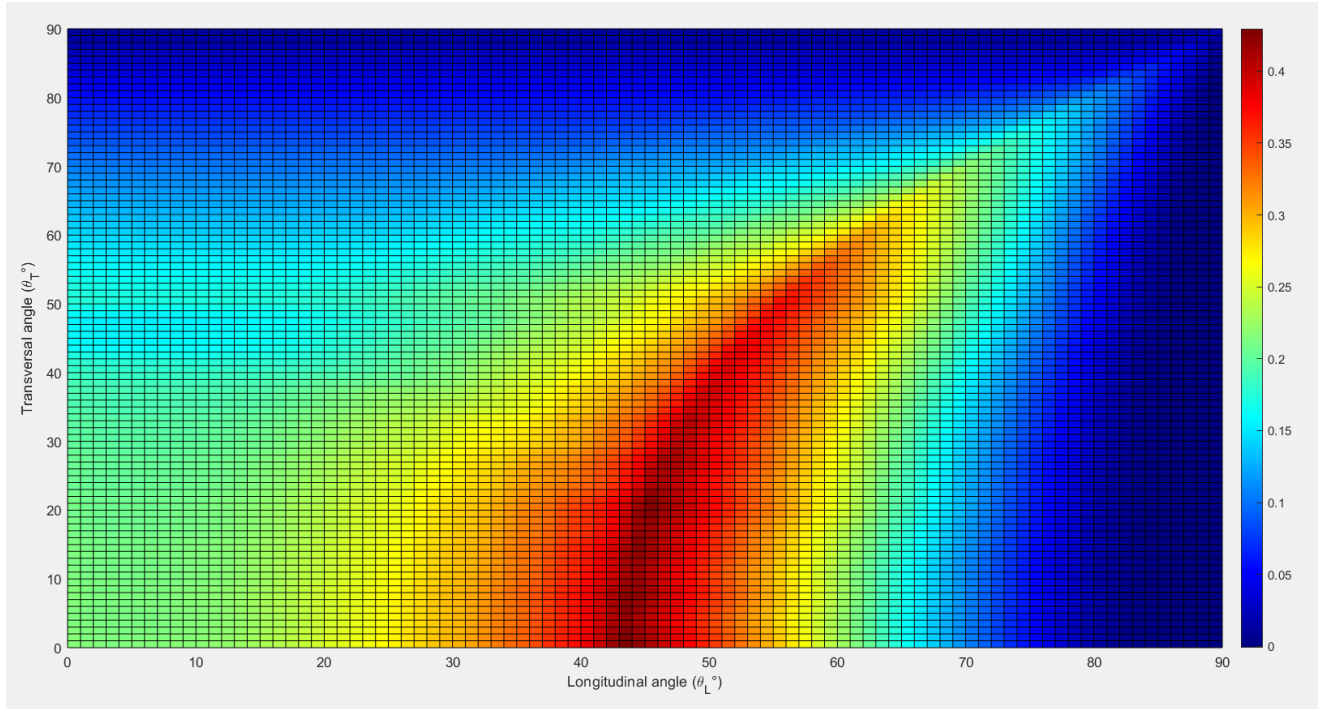


Figure 62: Difference of the IAM values depending on longitudinal and transversal angle between the two different NIO plants weighted by optical efficiency at zenith.

The NIO without glass is always better, except in the cases of very high angles where both behave in the same way. This chart is plotted after weighting the IAMs values with the corresponding efficiencies at zenith position. Actually, the optical efficiency at zenith for the NIO plant with the glass surface is 0.544, which is dramatically worse compared to the original NIO efficiency, which was 0.76055. Therefore, these results show the drawback of mounting a glass surface in the aperture of a receiver designed with NIO. The energy assessment shows that annually, out of 1951.4 kWh/m², only 529.6 kWh/m² are recoverable with the LFR with NIO and glass surface. In the following graphs, the daily solar energy balances are presented:

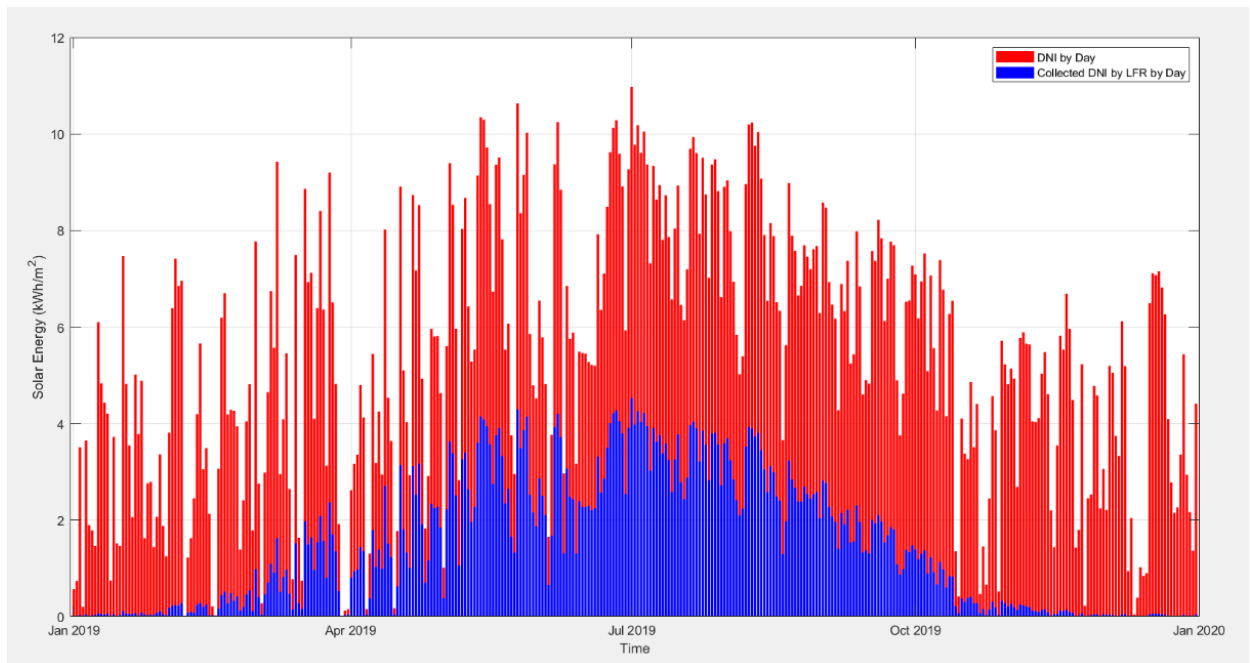


Figure 64: DNI available by day vs Energy collected by the Receiver of the LFR improved with glass by day.

The amount of energy absorbed by the receiver compared to the available energy is very low in this last plant as could be anticipated in view of thanks to the modest IAM values and to the poor efficiency evaluated at zenith.

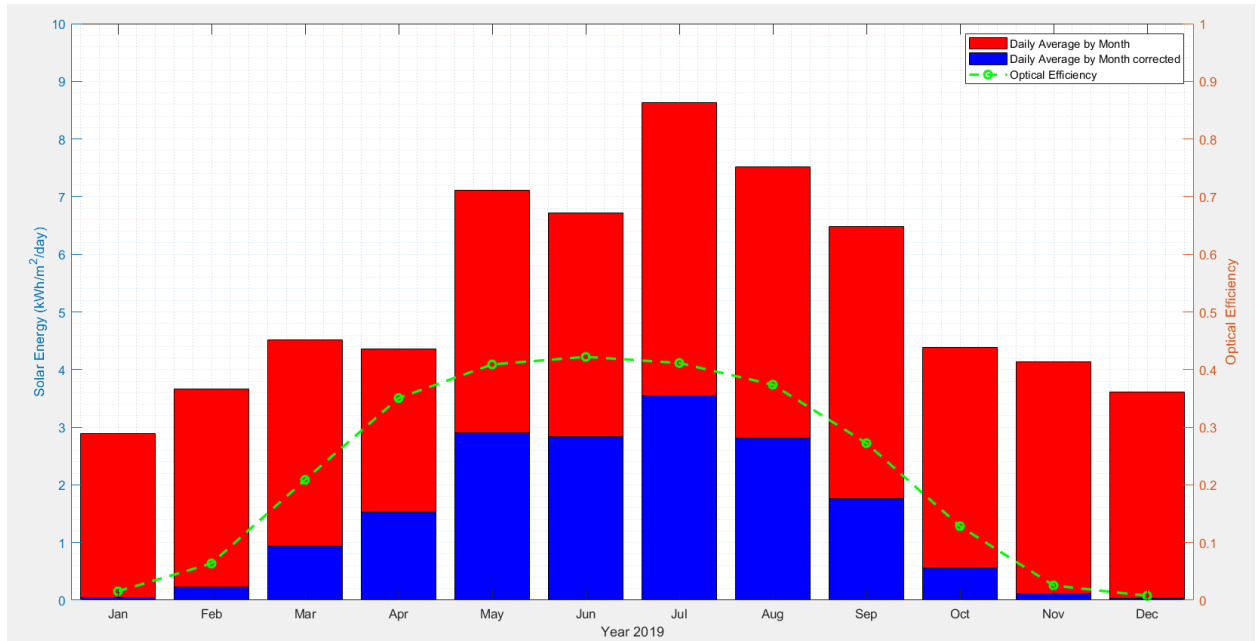


Figure 65: Daily average available and collectable energy and corresponding optical efficiency of the improved LFR with glass.

This plant is so inefficient that, as can be seen from the former graph, in the winter months (January, February, November and December) the Daily Average Solar Energy received was very close to 0 kWh/m²/day while available energy was almost 3-4 kWh/m²/day. Therefore, the efficiency takes the maximum in summer with 42%.

Finally, in order to check that the outcomes obtained for 2019 could be the same for other years, the enormous data set of DNI recorded by the pyrheliometer from July 2016 to September 2020 was used to evaluate the daily energy available and the daily energy absorbed by month for the different three plants. The following table and graph sum up the outcomes for the three plants:

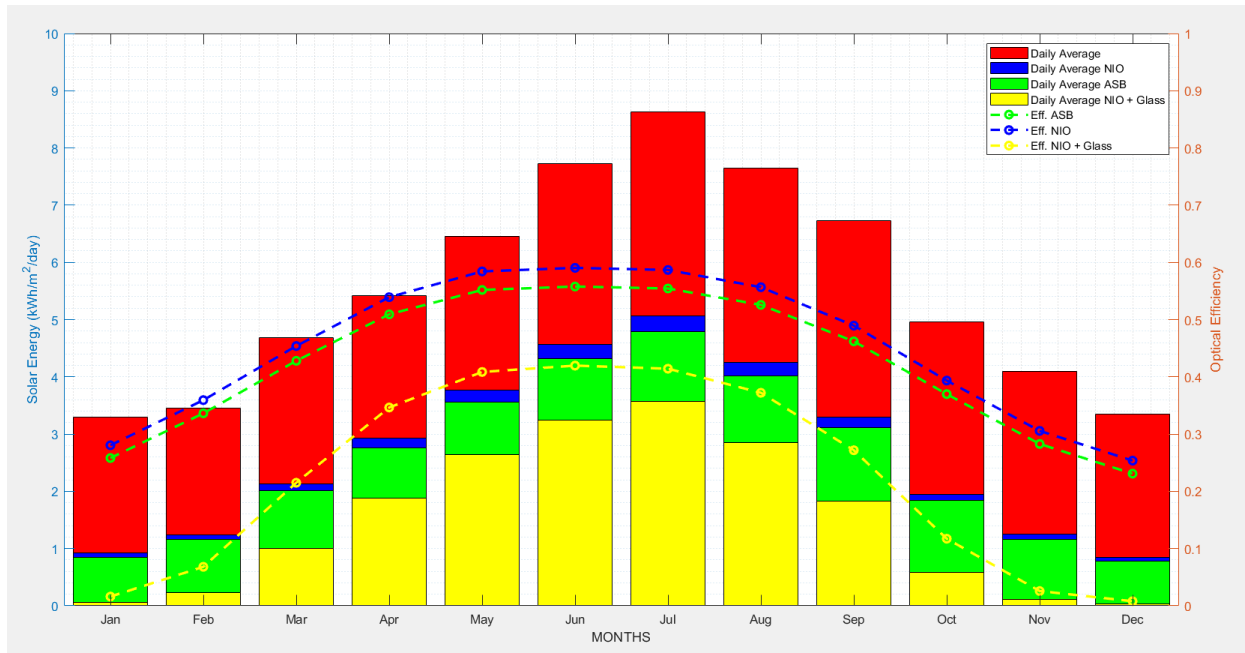


Figure 66: Daily Average Solar Energy Comparison between the three plants.

Month	Jan	Feb	Mar	Apr	May	Jun	Jul	Aug	Sep	Oct	Nov	Dec	YEAR AVE.
Daily Av. Energy [kWh/ m ² /day]	3.29	3.45	4.68	5.42	6.45	7.73	8.63	7.64	6.72	4.96	4.09	3.35	5.55
Daily Av. Energy NIO LFR [kWh/ m ² /day]	0.92	1.24	2.12	2.92	3.77	4.56	5.06	4.25	3.29	1.95	1.25	0.85	2.69
Daily Av. Energy ASB. LFR [kWh/ m ² /day]	0.85	1.16	2.00	2.76	3.56	4.31	4.78	4.02	3.10	1.83	1.15	0.77	2.53
Daily Av. Energy NIO LFR with Glass [kWh/m ² /day]	0.05	0.23	1.00	1.87	2.63	3.24	3.57	2.84	1.82	0.58	0.10	0.02	1.50

From the results outlined in the previous graph and table comparing the three plants, it is clear that while between the ASB and NIO plants there is a certain similarity, the same cannot be confirmed for the improved LFR plant with the insertion of the glass surface. Generally speaking, higher efficiencies (therefore a higher amount of received energy) are achieved during the summer season, whereas in the winter they are low, especially for the NIO plant with glass, which showed a value very near to 0.

7. *Flux Analysis*

Using the Tonatiuh++ software another important analysis can be performed to qualitatively assess the operation of a concentrator, and not only in terms of its energy balance, as done previously. For the scope of this thesis, as discussed above, after the current LFR plant and the enhanced one were constructed, they underwent an energy assessment to evaluate how much thermal energy is concentrated onto the receiver. To do so, via the script tool, IAM analysis was applied. The results acquired thus far do not provide information on how the concentrated solar power is distributed along the absorber. This is performed with the “Flux Analysis” tool. Therefore, in this Chapter, after a brief description of how it works and a short discussion about convergence analysis, Flux Analysis is carried out for the existing LFR and for the upgraded one. Their differences are then analysed.

7.1 *Description of the Flux Analysis tool*

Once the plant is constructed within the software, the “Flux Analysis” tool can be opened thanks to the option present in the “Run” section. A window pops up and the user selects the component to be meshed. The user then chooses the number of cells in the x and y directions. Actually, in the existing LFR plant, 3254 cells are set in the y direction, whereas 22 cells set in the x direction, defining cells of 1cm x 1cm. The user sets the number of rays to be sent from the sun and runs the simulations. The graphical results and metadata can be exported. This first helps to find the convergence by increasing the number of rays (cf. next paragraph). The results are thus directly displayed by the tool directly in three different graphs:

1. one general plot with the flux distribution on the selected node,
2. one plot along a selected x value,
3. one plot along a selected y value.

In the x direction the cells are distributed between “Umin” and “Umax” (cf.

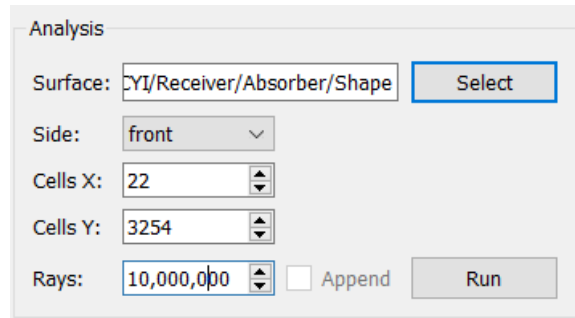
Appendix), -0.5 and 0.5 respectively in the present study. In the meta-data, the total power received by the surface or the minimum/maximum flux received are available on the left side of the window.

7.2 *Convergence Analysis*

In order to carry out simulations in loop within Tonatiuh++, the number of rays required is chosen as a result of a trade-off between the computational time and the accuracy of the results. Here a convergence analysis is performed to determine it. Then the value can be used to lead simulations within loops for the different positions of the sun.

7.2.1 *Convergence Analysis on ASB plant.*

The existing LFR plant installed at The Cyprus Institute was studied, setting as the number of cells on x direction and y direction at 22 and 3254 respectively.

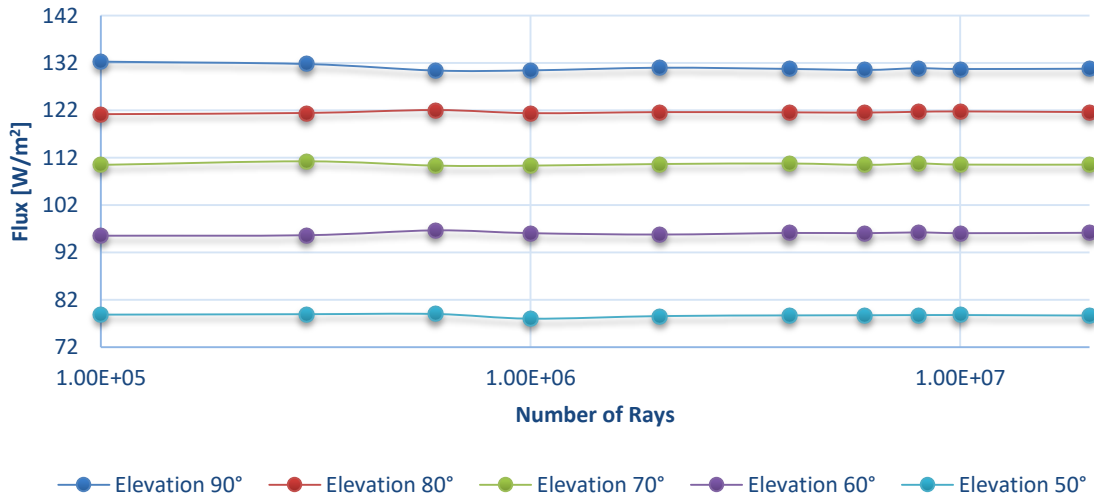


The image shows a software window titled "Analysis". It contains several input fields and buttons. The "Surface" field has the text "CYI/Receiver/Absorber/Shape" and a "Select" button to its right. The "Side" field is a dropdown menu showing "front". The "Cells X" field is a numeric input with "22". The "Cells Y" field is a numeric input with "3254". The "Rays" field is a numeric input with "10,000,000". To the right of the "Rays" field is an unchecked "Append" checkbox and a "Run" button.

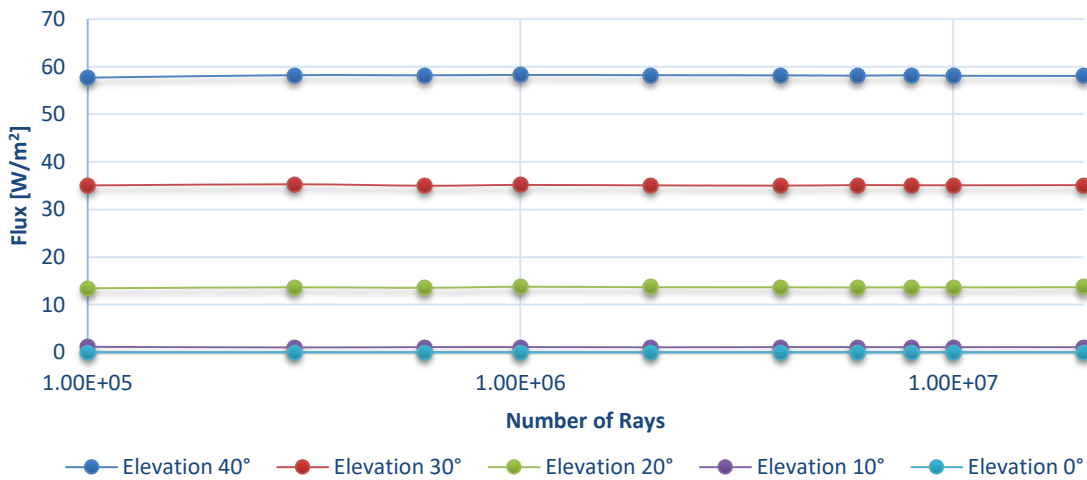
Figure 67: Flux Analysis Parameters view for the existing LFR plant.

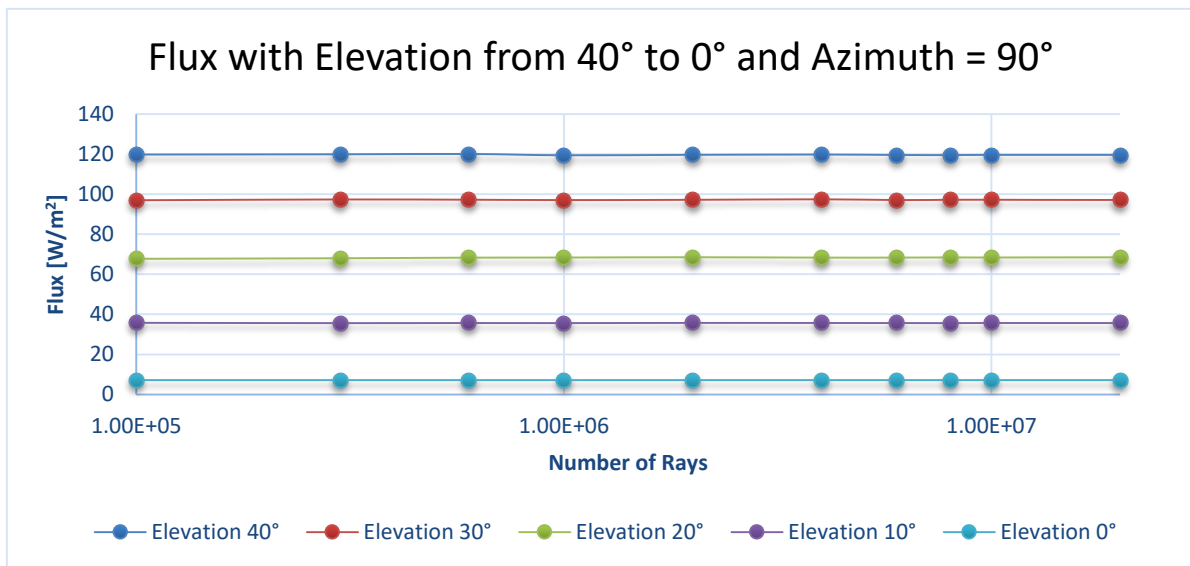
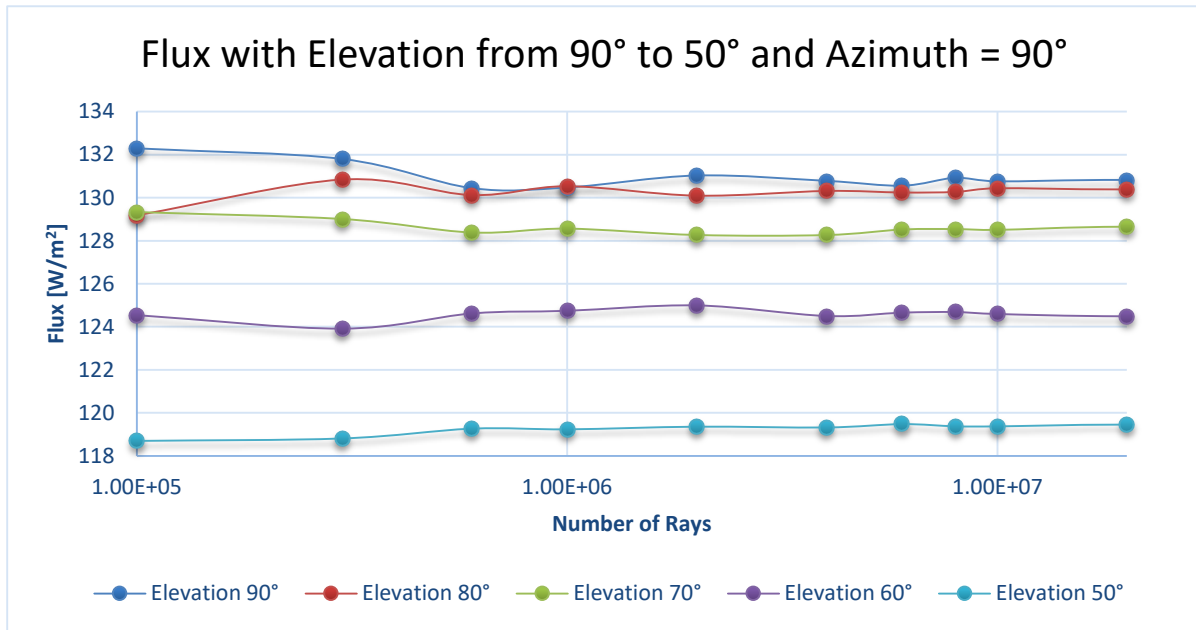
The first 2 sets of convergence analyses are led in azimuth (0° or 90°) and increasing elevations. The number of rays sent is: 10^5 , $3 \cdot 10^5$, $6 \cdot 10^5$, 10^6 , $2 \cdot 10^6$, $4 \cdot 10^6$, $6 \cdot 10^6$, $8 \cdot 10^6$, 10^7 and $2 \cdot 10^7$. The next graphs are obtained:

Flux with Elevation from 90° to 50° and Azimuth = 0°



Flux with Elevation from 40° to 0° and Azimuth = 0°

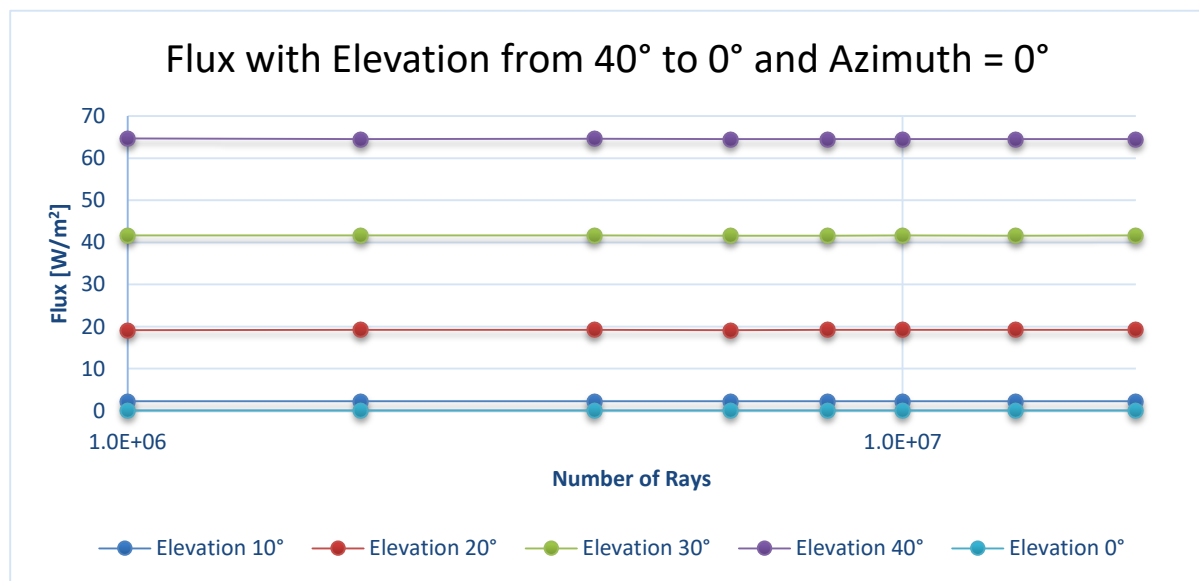
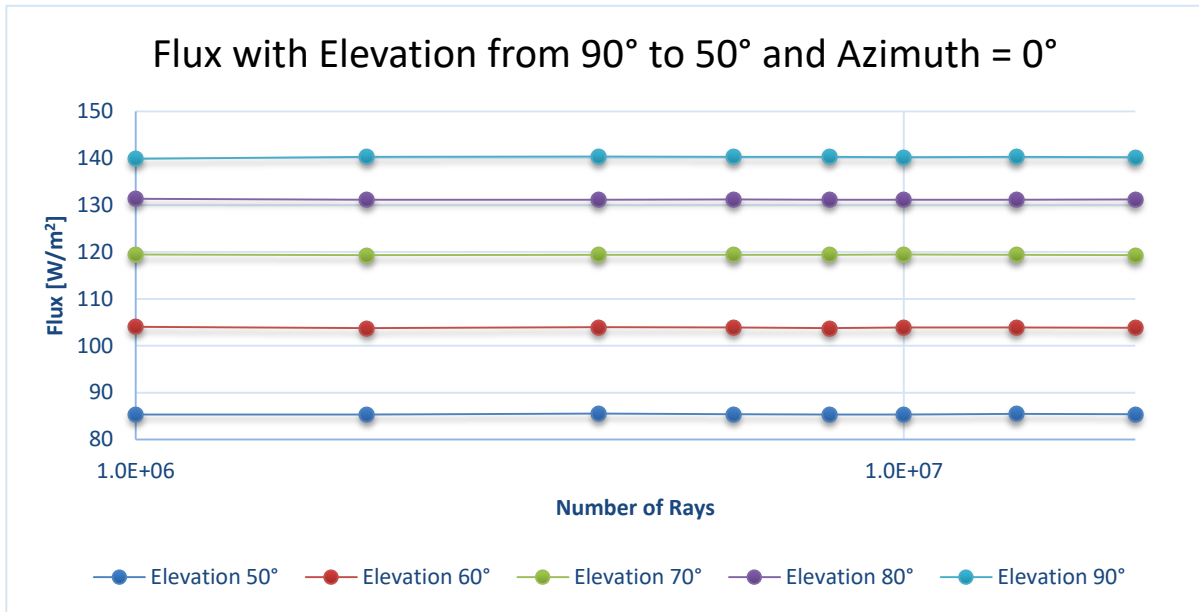




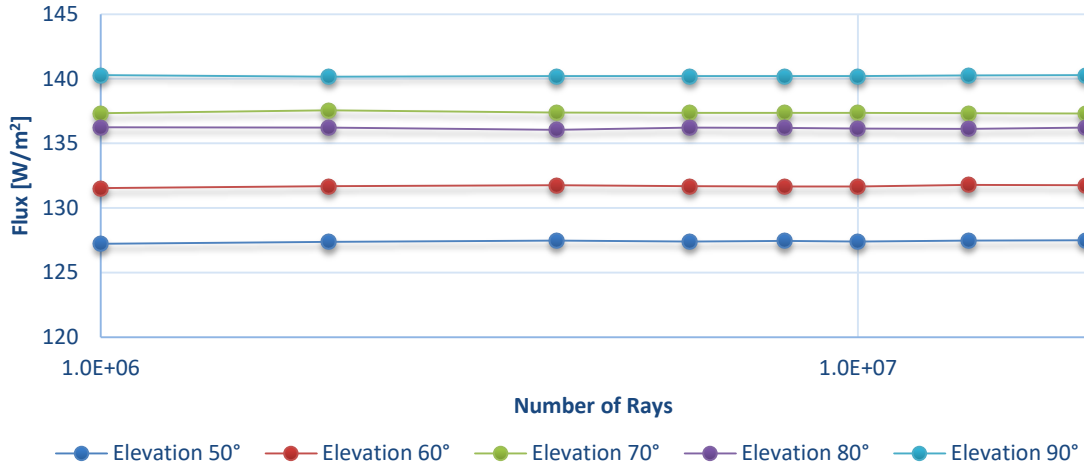
Flux is stabilized at 10^7 rays, therefore for the existing plant the various simulations are carried out with 10^7 solar rays.

7.2.2 Convergence Analysis on NIO plant.

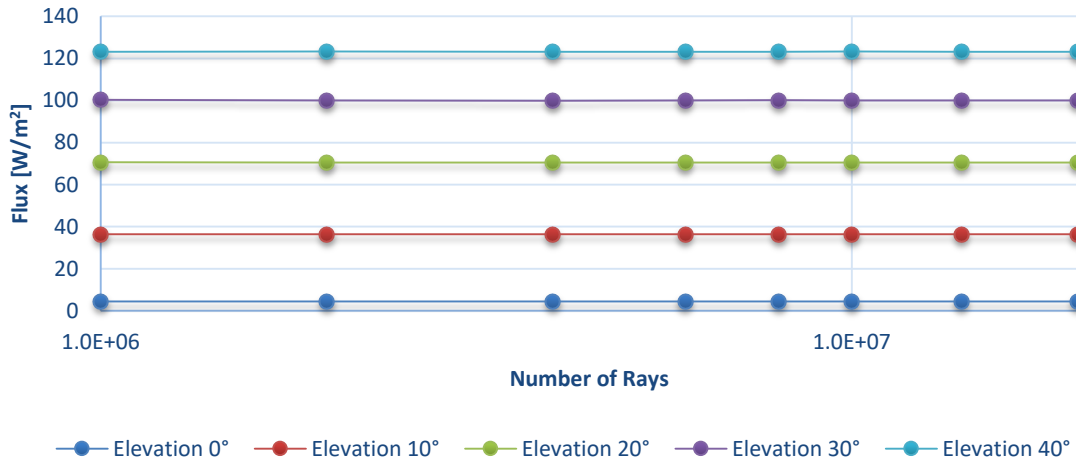
In the same way, the convergence analysis was performed on the plant with a receiver designed with NIO. For the study, 20 and 9763 cells were placed in the x and y directions respectively, while the rays sent were: $2 \cdot 10^5$, $4 \cdot 10^5$, $6 \cdot 10^5$, $8 \cdot 10^5$, 10^6 , $2 \cdot 10^6$, $4 \cdot 10^6$, $6 \cdot 10^6$, $8 \cdot 10^6$, 10^7 , $4 \cdot 10^7$ and $2 \cdot 10^7$. The following graphs were obtained:



Flux with Elevation from 90° to 50° and Azimuth = 90°



Flux with Elevation from 40° to 0° and Azimuth = 90°



As for the existing LFR, in the improved plant the optimum number of rays to obtain a good convergence is 10^7 .

7.3 Flux Analysis in existing LFR plant.

This embedded tool in Tonatiuh++ has been exploited in this thesis in order to understand and extract information about the distribution of the flux around the

receiver for the different positions of the sun. With 10^7 solar rays, different simulations were carried out after fixing the azimuth angle to 0° , therefore facing South, and with varying elevations from 90° to 30° with an angle step of 30° . The flux received was computed accordingly. As for the other simulations of this thesis, DNI was fixed to $1 \text{ W}\cdot\text{m}^{-2}$ in Tonatiuh++. The following graphs present the flux distribution on the absorber for 30° , 60° and 90° in the left column and the flux in the centre of the absorber in the right column:

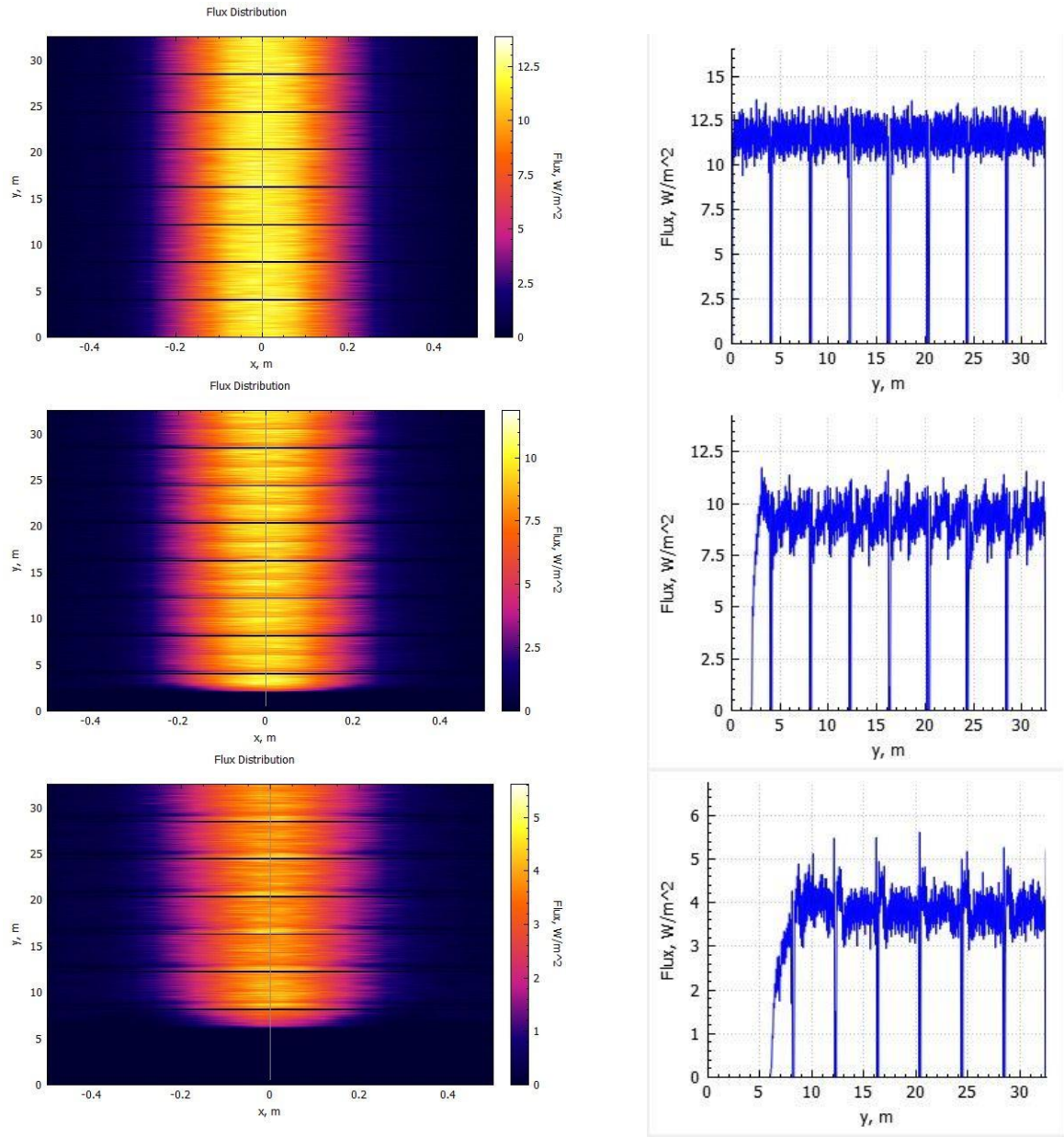


Figure 68: Flux Distribution at 90° , 60° and 30° of elevation.

At zenith, in the top plots, the flux spreads along the whole length, with a peak value of $13 \text{ W}\cdot\text{m}^{-2}$. When the angle of elevation is decreased to 60° , second row of plots, the peak power is slightly reduced to $12 \text{ W}\cdot\text{m}^{-2}$ but the flux is zero from 0 to 2.5 m of absorber pipe as no solar rays are concentrated, due to the end effect. This is amplified with 30° of elevation on the low plots with a lower peak value ($5.5 \text{ W}\cdot\text{m}^{-2}$). The part of the absorber which does not receive any solar concentrated power is between 0 and 6 m. The dark horizontal lines correspond to blocking due to the flanges and seals. In the x direction, the Flux Analysis outlines the malfunction of the secondary mirror since the top half cylinder of the absorber, which thus faces the secondary mirror, is not receiving any rays, and solely the part facing the primary reflector is. The next graph illustrates the correlation between the power concentrated on the receiver and the elevation angle:

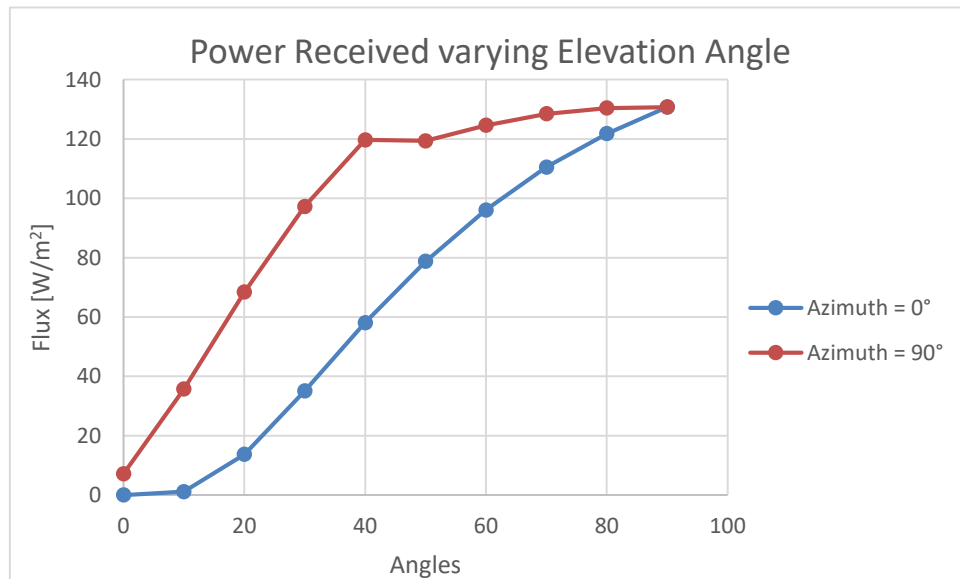


Figure 69: Power Received by the absorber by varying the Elevation angle and fixing the Azimuth angle.

As seen before regarding the IAM results, the power received is affected by the variation in elevation when the azimuth is fixed at 0° , since longitudinal cosine loss increases as a consequence of the partial disuse of the absorber, whereas it is only slightly influenced when the azimuth is at 90° . As matter of fact, if a flux analysis is performed after varying the elevation angle and fixing the azimuth angle at 90° , the main losses are the blocking and shading occurring between the mirrors and the shading of the receiver onto the primary reflector. Here, in terms of flux

distribution, there is only a slight reduction in the flux peak power and a translation of the symmetry of distribution in the x direction from 0 towards positive values.

7.4 Flux Analysis in existing LFR plant without Glass pipes.

The same study was carried out after removing the glass pipes from the absorber tube of the existing LFR plant in order to evaluate the possible differences:

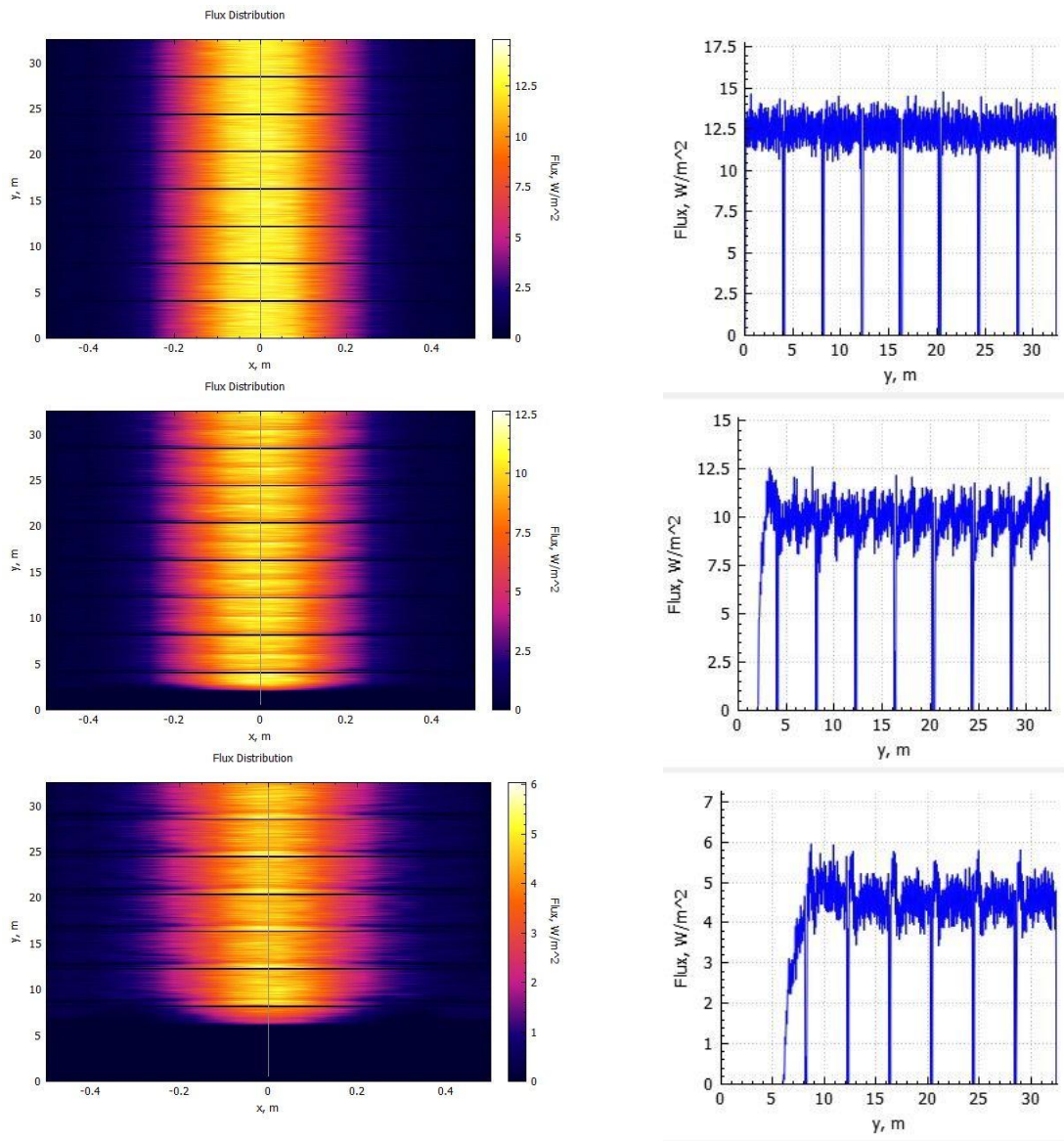


Figure 70: Flux Distribution without Glass pipes at 90°, 60° and 30° of Elevation.

The only difference when compared with the configuration with glass was found in the flux peak value, which were slightly higher for the different elevation angles. In detail, maximum values for 90°, 60° and 30° were respectively 14.7 W·m⁻² (instead of 13 W·m⁻²), 12.5 W·m⁻² (instead of 12 W·m⁻²) and 6 W·m⁻² (instead of 5.5 W·m⁻²). The same effects were also recorded for the blocking of the flux power in the part of the absorber facing North and the reducing of the peak value, as highlighted earlier. This study performed on the existing plant without glass pipes was used as a control comparison for the next study presented in the following paragraph.

7.5 Flux Analysis with Non-imaging Optics.

The same “Flux Analysis” tool was used for the plant with the receiver designed with non-Imaging Optics in order to compare its behaviour with that of the previous receiver without glass. As the software can only deal with one surface node at a time, separate analyses were performed on each of the two legs of the U-shaped absorber. They were then merged together using Matlab with symmetric transformation. The following charts explain the behaviour of the flux distribution after fixing the azimuth angle at 0° and the elevation angle at 90° , 60° and 30° :

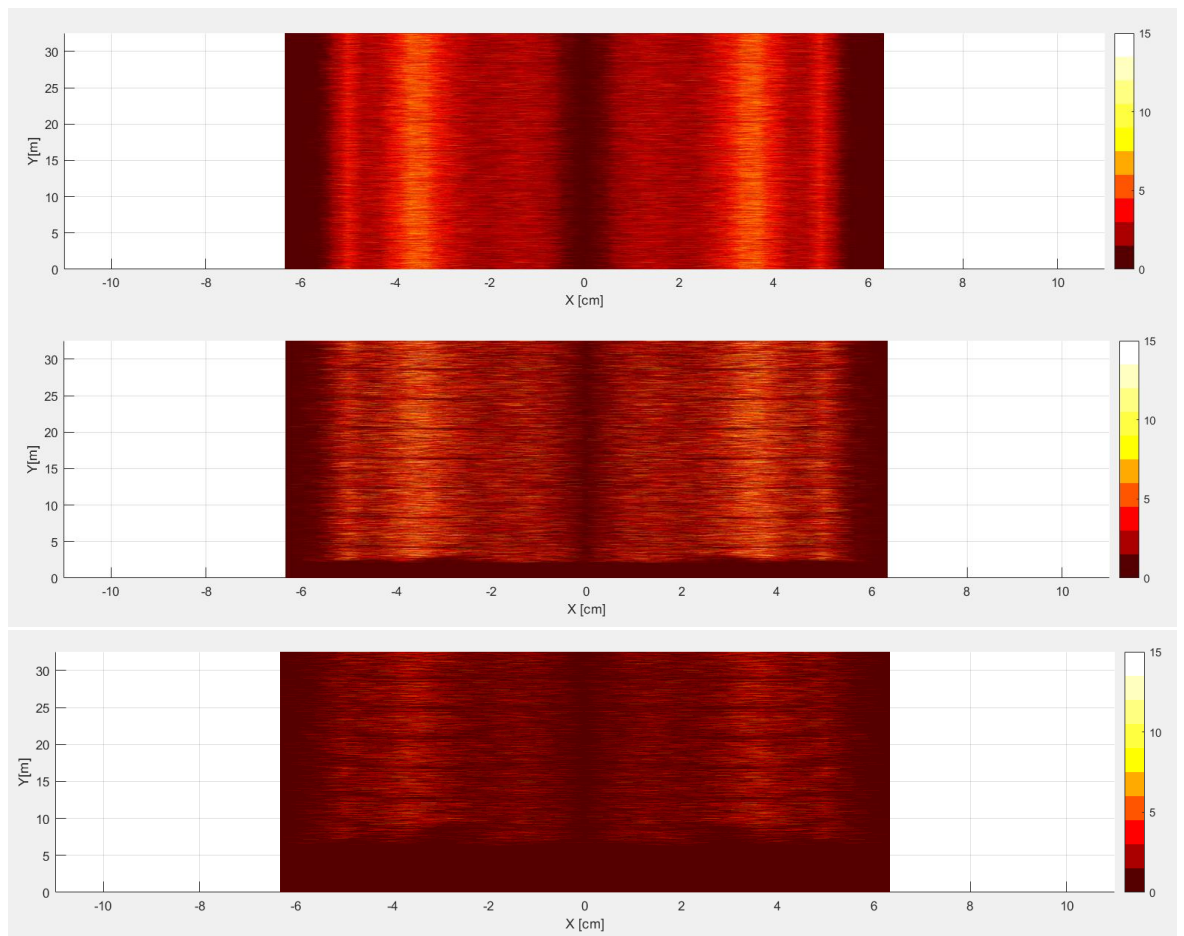


Figure 71: Flux distribution for the two absorbers of the LFR plant with NIOs. The top figure is at 90° of elevation, the middle is at 60° and the bottom one is at 30° .

As for the existing LFR plant, the flux distribution decreases as the elevation angle is reduced: when the sun is at zenith, the flux is more than $5 \text{ W}\cdot\text{m}^{-2}$, but it drops away in the other two sun positions. Obviously, the blocking of the rays at the part of the receiver facing North can be observed here. In the following graph the

improved LFR plant's distribution flux is compared to the previous one in order to identify any differences:

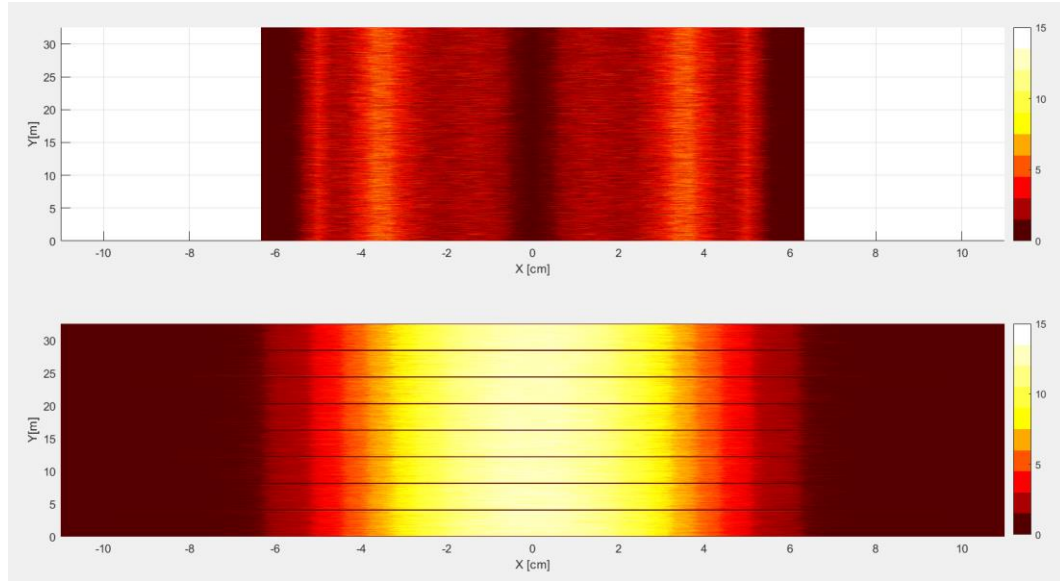


Figure 72: Comparison Flux Distribution of the two plants.

Firstly, in direction x the distribution between the two receivers is different. As a matter of fact, the circumference of the absorber of the existing one (0.2199 m) is higher than the sum of the circumferences of the U-shaped absorber in the upgrade LFR plant (0.134 m). In each figure, $x=0$ corresponds to the bottom part of the receiver, whereas the outer x refers to the top part of the receiver. The existing secondary mirror does not function properly since no rays impinge on the top part of the receiver, unlike the non-Imaging optics, which redistributes the solar flux more smoothly. Therefore, energy assessment with the non-Imaging optics showed a very low enhancement, but there was a considerable improvement in flux distribution with the non-Imaging Optic since it allows a uniform distribution of the solar beams reflected by the primary reflector.

8. *Conclusions*

The present thesis emphasizes a methodology to assess the optical performance of a LFR facility. More specifically, it was carried out for the LFR at The Cyprus Institute using Ray-Tracer Tonatiuh++ Software. After the existing LFR plant (ASB) (cf. Appendix) was constructed in the software, this methodology was applied to perform an IAM analysis considered as a result of all optical losses. At the end of the process, a graphical distribution of the IAM was obtained according to the transversal θ_T and longitudinal θ_L angles. The shape of the Non- Imaging Optics (NIO) was calculated considering the dimensions of the existing plant in order to employ them as a potential secondary reflector. Tonatiuh++ compared the IAM distribution with the different configurations. After the energy available at the Cyprus Institute on a yearly and monthly basis was estimated (see Chapter 5), the energy absorbed by the receivers of the two LFR plants was assessed. The results obtained showed that the amount of energy reaching the absorber in the ASB plant was 45% of the total available energy, based on the data collected in Nicosia in 2019, whereas in the improved plant with NIO the energy collected reached 48%. Therefore, a slight improvement in the second plant was observed, but after the insertion of a flat glass surface at the aperture of the receiver to prevent the accumulation of dust on the U-shaped absorber and Non Imaging Optics, only 27% of the total energy available was captured. Consequently, the model needs to be further developed by adding reflection coating in order to optimize this last value obtained. The results obtained in the energy assessment were tested considering daily average energy available monthly considering addition data provided by pyrliometer from July 2016 to September 2020. The same yearly energy distributions are achieved compared to the 2019's results. Afterwards, Flux Analysis was carried out on the two plants in order to visualize how the solar reflected flux is distributed all over the absorber surface and how it can vary as the polar position changes. Actually, with the decreasing of elevation from 90° to 30° the maximum flux recorded on the receiver is decreasing of 58%. For making a

comparison with the LFR with NIO in terms of Flux Analysis, the flux distribution on the existing LFR was further studied considering it without glass pipes. In this case, the maximum fluxes recorded were slightly better compared to the case with glass pipes with an increasing of 12% in the case of 90° of elevation. Finally, the solar flux distribution in the two plants was compared, which highlighted the greater utility of using the Non-Imaging Optics compared to the existing secondary mirror, since it is able to make the surplus solar rays available to the absorber more efficiently. Indeed, the secondary mirror reflector doesn't reflect the spare solar rays to the absorber adequately, whereas the Non-Imaging Optics, thanks its specified shape composed by an involute and MFE, make the flux distribution uniform along the circumference of the absorber.

Bibliography

- [1] X. Lemaire, “Glossary of Terms in Sustainable Energy Regulation,” *Renew. Energy Energy Effic. Partnersh.*, no. August 2004, pp. 1–11, 2010.
- [2] “EU Climate Action,” *EU*. [Online]. Available: https://ec.europa.eu/clima/policies/strategies/2020_en. [Accessed: 19-Aug-2020].
- [3] E. Commission, “European Green Deal.” [Online]. Available: https://ec.europa.eu/info/strategy/priorities-2019-2024/european-green-deal_en. [Accessed: 13-Oct-2020].
- [4] E. Commission, “The Just Transition Mechanism: making sure no one is left behind.” [Online]. Available: https://ec.europa.eu/info/strategy/priorities-2019-2024/european-green-deal/actions-being-taken-eu/just-transition-mechanism_en. [Accessed: 13-Oct-2020].
- [5] “IGI Poseidon.” [Online]. Available: <http://www.igi-poseidon.com/en>. [Accessed: 09-Oct-2020].
- [6] “Eastern Mediterranean Natural Gas Pipeline – Pre-FEED Studies.” [Online]. Available: <https://ec.europa.eu/inea/en/connecting-europe-facility/cef-energy/7.3.1-0025-elcy-s-m-15>. [Accessed: 09-Oct-2020].
- [7] “The EuroAsia Interconnector,” no. October, pp. 1–41, 2017.
- [8] “The EuroAsia Interconnector.” [Online]. Available: <https://euroasia-interconnector.com/>. [Accessed: 09-Oct-2020].
- [9] Sam Morgan, “Cyprus set to come in from the cold and end energy isolation,” *EURACTIV.com*, 2017.
- [10] “IEA- International Energy Agency.” [Online]. Available: <https://www.iea.org/countries/Cyprus>. [Accessed: 03-Sep-2020].
- [11] Cyprus Profile, “Exploration Race.”
- [12] Eurostat, “CY-Energy-balance-sheets-June-2020-edition.”

- [13] O. O. Bamisile, A. A. Babatunde, M. Dagbasi, and I. Wole-Osho, "Assessment of solar water heating in Cyprus: Utility, development and policy," *Int. J. Renew. Energy Res.*, vol. 7, no. 3, pp. 1448–1453, 2017.
- [14] "The World Bank." [Online]. Available: <https://data.worldbank.org/indicator/EG.EGY.PRIM.PP.KD?end=2015&locations=CY&start=1990&view=chart>. [Accessed: 03-Sep-2020].
- [15] "World Energy Council." [Online]. Available: <https://trilemma.worldenergy.org/#!/energy-index>. [Accessed: 03-Sep-2020].
- [16] the free encyclopedia Wikipedia, "Solar Energy." [Online]. Available: https://en.wikipedia.org/wiki/Solar_energy. [Accessed: 10-Sep-2020].
- [17] the free encyclopedia Wikipedia, "Sunlight." [Online]. Available: <https://en.wikipedia.org/wiki/Sunlight>. [Accessed: 25-Sep-2020].
- [18] "Solargis." [Online]. Available: <https://solargis.com/>. [Accessed: 15-Sep-2020].
- [19] the free encyclopedia Wikipedia, "Concentrated solar power." [Online]. Available: https://en.wikipedia.org/wiki/Concentrated_solar_power. [Accessed: 15-Sep-2020].
- [20] T. P. S. U. Mark V. Fedkin, Ph.D. in Geo-Environmental Engineering / Assistant Teaching Professor in the Renewable Energy and Sustainability Systems (Online Masters and Graduate Certificates Program), "EME 812: Utility Solar Power and Concentration." [Online]. Available: <https://www.e-education.psu.edu/eme812/>. [Accessed: 06-Sep-2020].
- [21] A. Segal, "Optics of Solar Concentrators," Weizmann Institute of Science, 2010.
- [22] M. T. Islam, N. Huda, A. B. Abdullah, and R. Saidur, "A comprehensive review of state-of-the-art concentrating solar power (CSP) technologies: Current status and research trends," *Renew. Sustain. Energy Rev.*, vol. 91, no. April, pp. 987–1018, 2018.

- [23] the free encyclopedia Wikipedia, "Ivanpah Solar Power Facility." [Online]. Available: https://en.wikipedia.org/wiki/Ivanpah_Solar_Power_Facility. [Accessed: 10-Nov-2020].
- [24] T. M. HUI, "DESIGN AND OPTIMIZATION OF HELIOSTAT FIELD USING SPINNING-ELEVATION SUN TRACKING METHOD BASED ON COMPUTATIONAL ANALYSIS," 2011.
- [25] C. N. Papanicolas *et al.*, "CSP cogeneration of electricity and desalinated water at the Pentakomo field facility," *AIP Conf. Proc.*, vol. 1734, no. May 2016, 2016.
- [26] K. Lovegrove, "The SG4 Big Dish." [Online]. Available: <https://bigdishsolar.com/>. [Accessed: 10-Nov-2020].
- [27] U. E. Department, "Compact Linear Fresnel Reflector." [Online]. Available: <https://fineartamerica.com/featured/compact-linear-fresnel-reflector-us-department-of-energy.html>. [Accessed: 15-Sep-2020].
- [28] A. Montenon, "INTRODUCTORY COURSE ON CONCENTRATING SOLAR Support document to the presentation ' Linear Fresnel .'"
- [29] F. L. S. INC., "World's First Utility-Scale Molten Salt Fresnel Concentrated Solar Power Plant Connects to China's Grid," 30/06/2020. [Online]. Available: <https://flsnova.com/2020/06/30/worlds-first-utility-scale-molten-salt-fresnel-concentrated-solar-power-plant-connects-to-chinas-grid/>. [Accessed: 11-Oct-2020].
- [30] China Solar Thermal Alliance, "First in the world, 50MW molten salt Fresnel CSP plant commercially operated." [Online]. Available: <http://en.cnste.org/html/news/2020/0619/752.html>. [Accessed: 11-Oct-2020].
- [31] Novatec Solar, "Puerto Errado 2 in Spain." [Online]. Available: <https://web.archive.org/web/20150402123845/http://www.novatecsolar.com/56-1-PE-2.html>. [Accessed: 11-Oct-2020].
- [32] SolarPACES, "CSP Puerto Errado2 Data." [Online]. Available:

- <https://solarpaces.nrel.gov/puerto-errado-2-thermosolar-power-plant>.
[Accessed: 11-Oct-2020].
- [33] CSP-F, “CSP FRESNEL PER L’INDUSTRIA: PARTE IL PRIMO CANTIERE IN SARDEGNA.” [Online]. Available: <http://www.cspfsolar.it/news/realizzazioni/il-primo-cantiere-in-sardegna/>. [Accessed: 11-Oct-2020].
- [34] South African Builder, “MTN installs Africa’s first concentrating solar power/cooling system.”
- [35] “STS-Med.” [Online]. Available: <http://www.stsmed.eu/>. [Accessed: 10-Nov-2020].
- [36] F. M. Montagnino, F. Paredes, A. Giaconia, and N. Fylaktos, “Solar Multi-Generation in the Mediterranean Area, the Experience of the Sts-Med Project,” pp. 1–9, 2017.
- [37] V. Sharma, “Hourly and monthly variation in shading and blocking of aperture area in a linear fresnel reflector field,” *Energy Procedia*, vol. 48, pp. 233–241, 2014.
- [38] M. Rycroft, “Linear Fresnel systems and the future for Concentrated Solar Power.” [Online]. Available: <http://helioscsp.com/linear-fresnel-systems-and-the-future-for-concentrated-solar-power/>. [Accessed: 10-Sep-2020].
- [39] M. Günther, “Linear Fresnel Technology,” *Adv. CSP Teach. Mater.*, pp. 1–43, 2011.
- [40] the free encyclopedia Wikipedia, “Involute.” [Online]. Available: <https://en.wikipedia.org/wiki/Involute>. [Accessed: 23-Oct-2020].
- [41] Julio Chaves, *Introduction to Nonimaging Optics*. 2010.
- [42] National Oceanic and Atmospheric Administration, “NOAA Solar Calculator.” [Online]. Available: <https://www.esrl.noaa.gov/gmd/grad/solcalc/>. [Accessed: 23-Sep-2020].

Appendix

1. Description of Tonatiuh

The Tonatiuh software is an open source and smart Monte Carlo Ray tracer for the optical simulation of solar concentrating systems. In this appendix, the description of how a Linear Fresnel Reflector can be constructed is discussed. Firstly, it is necessary to discuss Tonatiuh's main characteristics. It is composed of 4 main parts:

- The graphical user interface (GUI), which gives a 3D representation of the site.
- A tree-view of the different objects (or nodes), where the components of the site are shown.
- Node Parameter section, where the current parameters of a selected node are shown and they can be modified.
- Toolbar section, where “Open”, ”Save”, “Copy” and other usual functions are present. Here other specific functions such as the running click of the Ray Trace Analysis or Flux Analysis are introduced.

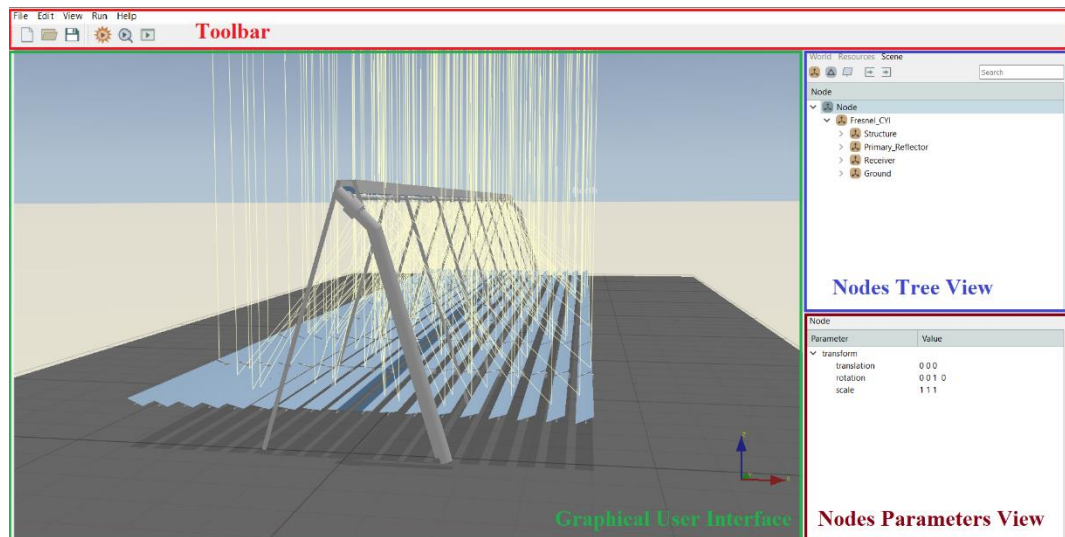


Figure 73: Tonatiuh Main Interface.

A system can be easily constructed in the software using different elements that are called Nodes. They can be ordered hierarchically taking into account the relationship (parents-children) between different nodes. For example, if a component of the system is made up of three different parts, it is considered a parent node of three nodes (one for each part). Therefore, this specific component could be a child node of the entire system. There are three different types of Node:

- **Group Nodes:** contain other child nodes, surface nodes and tracker nodes. Selecting these it is possible to modify its position, rotation and scale in the “Node Parameters” section. Any choice that is made here modifies the spatial properties of the child nodes.
- **Surface Nodes:** define the geometry and material of the parent node. Therefore, the geometry could be easily modified by selecting the shape (Choosing between “Planar”, “Planar N”, “Parabolic”, “Hyperbolic”, “Elliptic”, “Function Z”, “Cylinder”, “Function XYZ”, etc.) and profile (Choosing between “Box”, “Rectangular”, “Circular”, etc.). From the point of view of material, either “Transparent” or “Virtual”, and an “Absorber” or “Specular” tool can be selected in order to choose default values of reflectivity, transparency etc. If required, these parameters can be modified.
- **Tracker Nodes:** define how the parent node is to track the sun, defining different important technical properties (see the next paragraphs).



A new child node can be easily added by selecting the desired parent node and clicking on the corresponding icon in the

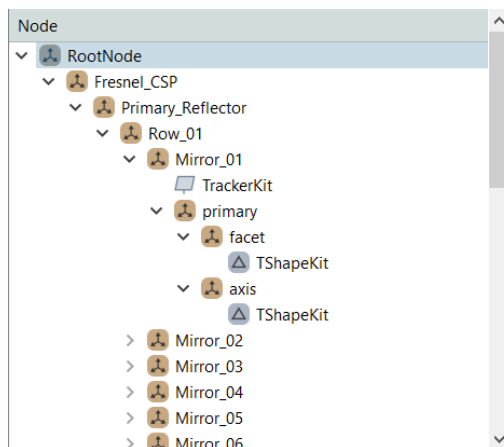


Figure 74: Mirror tree composition.

upper part of the “Nodes tree view” as shown in the figure presented on the left. The construction of the primary reflector is a good example in order to understand this logical scheme. Taking into account a specific row, every mirror is a child node of “Row_” node. Each mirror node is composed of a Tracker node, which is needed for the mirror to track the

sun's movement in the sky, and a Shape node, useful to define its shape in terms of geometrical and optical properties. Later on, the composition of the mirrors will be defined in more detail.

2. *Description of the design of the Fresnel Facility*

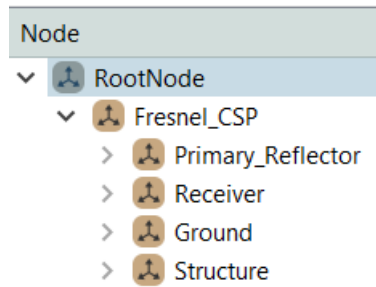


Figure 75: LFR Tree.

As can be easily read in the Figure to the left, the “RootNode” node contains the macro-node “Fresnel_CSP” which includes four different nodes, whose “Ground” one helps the user to better visualize the ground level. The other three nodes are the following:

- Primary Reflector Node: contains the construction of eighteen rows with eight mirrors of 0.32m*4m for each row. Therefore, for each row eight mirrors of the same geometrical and optical properties are fixed.
- Receiver Node: contains five child nodes related to the structure of the receiver. As discussed in the introduction of the thesis, the receiver of a LFR system is made up of the Absorber, Glass Pipes, Connections, Secondary Optic and Cover nodes.


```

graph TD
    Receiver[Receiver] --> Absorber[Absorber]
    Receiver --> Glass_Pipes[Glass_Pipes]
    Receiver --> Connections[Connections]
    Receiver --> Secondary_Reflector[Secondary_Reflector]
    Receiver --> Cover[Cover]
  
```
- Structure Node: A parent node consists in different parts of the LFR that are not included in the primary reflector and receiver (such as the Outlet/Inlet Tube, Beams and Motor Boxes).


```

graph TD
    Structure[Structure] --> Outlet[Outlet]
    Structure --> Inlet[Inlet]
    Structure --> Beams[Beams]
    Structure --> MotorBoxes[MotorBoxes]
  
```

Figure 76: Receiver Tree.

Figure 77: Structure Tree.

All these elements are described individually in order to understand how they are built.

2.1 Receiver

Parameter	Value
▼ transform	
translation	0 -0.034 4.27541
rotation	-1 -0 -0 90
scale	1 1 1

Figure 78: Receiver Parameters.

The receiver node consists five child nodes, as described above. After creating the group node and renaming it as “Receiver”, it is possible to define its position, rotation and scale. Considering the vector of position in

this specific order x y z, the height can be defined by putting 4.27541 m into the third number corresponding to the z axis, whereas a transition toward the y direction is needed in order to be -0.034 m respect to the primary reflector. A rotation is needed in order to position the element in the horizontal plane parallel to the ground.

2.1.1 Absorber

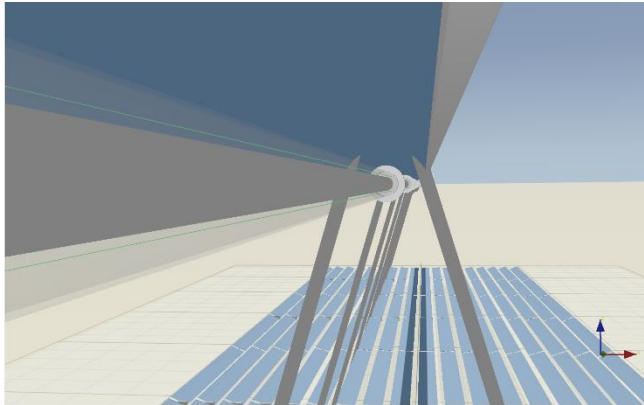


Figure 79: Absorber Node.

The main part of the receiver is the absorber. It is a cylinder with a radius of 0.035 m and 32.544 m long. Given that in the receiver node the position and rotation have already been defined, after the definition of the scale in x and y to fix the radius of the cylinder, a shape

node is added as visualized in the next figure to the left:

Absorber	
Parameter	Value
▼ transform	
translation	0 0 0
rotation	0 0 1 0
scale	0.035 0.035 1

Figure 81: Absorber Parameters.




Parameter	Value
▼ shapeRT	 Cylinder
caps	none
▼ profileRT	 Rectangular
uMin	-0.5
uMax	0.5
vMin	0
vMax	32.544
materialRT	 Absorber

Figure 80: Absorber Shape.

“uMin” and “uMax” are defined if a section of the cylinder is required. In this case, a total section of cylinder is needed, therefore it is necessary to fix the values present in the left figure. The “vMin” and “vMax” are used for setting the length of the cylinder, whereas for the selection of the material, the “absorber” type must be chosen, indeed the task of this component is to absorb the reflected sunrays arriving from the primary reflector. The caps are not needed and therefore “none” is fixed.

2.1.2 Glass Pipes

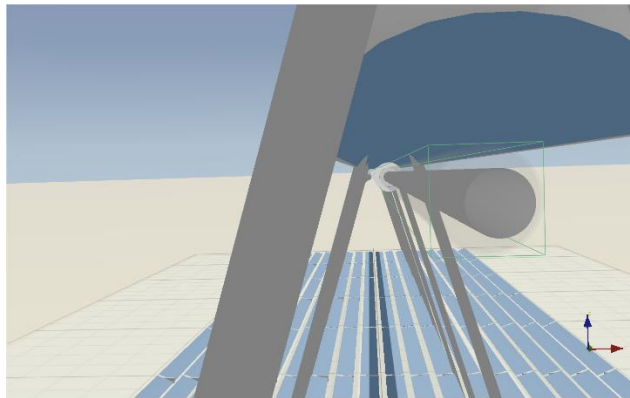


Figure 84: Glass Pipes Node.

The glass pipes are designed in Tonatiuh by an outer and inner surface. Indeed, the shapes designed in Tonatiuh are only surfaces and they do not have thickness. Consequently, the only difference between the inner and outer surfaces is the radius. The Glass Pipes node is





▼ 	Glass_Pipes
▼ 	Pipe_1
> 	Inner
> 	Outer

Figure 83: Glass Pipes Tree.

the parent of equal eight “Pipe_” children nodes, which are placed in different y positions. Due to the rotation performed in the “Receiver” node, to

characterize the position in the y direction the value must be set in the third value of the vector and not in the second. The position of the pipe

Pipe_1	
Parameter	Value
▼ transform	
translation	0 0 2.034
rotation	0 0 1 0
scale	1 1 1

Figure 82: Glass Pipe Parameters.

in the y direction is based on its middle point and evaluated considering a flange length of 0.084 m and a half of 3.9 m of its length, therefore this is leading to 2.034 m. The pipe is composed of an outer and inner cylindrical surface with a radius of 0.0625 m and 0.059 m respectively. Here too, “none” is fixed for “caps”. The material of these two surfaces is the Fresnel (unpolarized) with different values in nFront and nBack considering for radiative reasons.

Parameter	Value
▼ transform	
translation	0 0 0
rotation	0 0 1 0
scale	0.0625 0.0625 3.9

Figure 86: Outer Parameters.

Parameter	Value
▼ transform	
translation	0 0 0
rotation	0 0 1 0
scale	0.059 0.059 3.9

Figure 85: Inner Parameters.




Parameter	Value
▼ shapeRT	 Cylinder
caps	none
▼ profileRT	 Box
uSize	1
vSize	1
▼ materialRT	 Fresnel (unpolarized)
nFront	1.47
nBack	1

Figure 87: Inner/Outer Glass Pipe Shape.

2.1.3 Connections

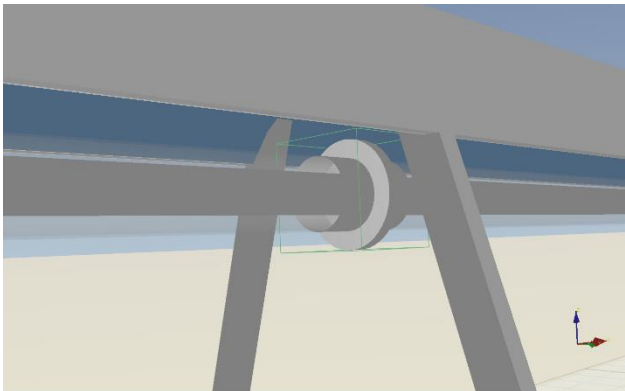


Figure 88: Connections Node.

The connections are designed to attach the two different pipes and they can be easily drawn in Tonatiuh. They are made up of flanges and expansion seals. The former were constructed in the software using two cylinders with a radius of 95 mm and 24 mm long. To complete their

pattern the expansion seals are defined as a cylinder with a radius of 62.5 mm and

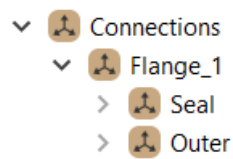


Figure 89: Connections Tree.

168 mm long. A single connection is made up of two child nodes required in order to be projected within Tonatiuh as can be seen in the Figure on the left. The connection component is repeated 9 times due to the eight pipes. After the creating of the first, the other ones could be drawn using

copy & paste and translating them considering the length of a pipe and the length of a connection. As regards their material, they are considered perfect absorbers. The shape of the expansion seals is defined as a cylinder with “none” caps whereas the flanges are set as a cylinder shape with caps in the bottom and top part (“both”):

Parameter	Value
▼ shapeRT	Cylinder
caps	both
▼ profileRT	Box
uSize	1
vSize	1
materialRT	Absorber

Figure 90: Outer Shape.

Parameter	Value
▼ shapeRT	Cylinder
caps	none
▼ profileRT	Box
uSize	1
vSize	1
materialRT	Absorber

Figure 91: Seal Shape.

Considering the middle point of the flange, the parameters for the different child components are defined as follows:

Parameter	Value
▼ transform	
translation	0 0 0
rotation	0 0 1 0
scale	0.0625 0.0625 0.168

Figure 92: Seal Parameters.

Parameter	Value
▼ transform	
translation	0 0 0
rotation	0 0 1 0
scale	0.095 0.095 0.024

Figure 93: Outer Parameters.

2.1.4 Secondary Reflector

As discussed in the descriptive part of this thesis, the secondary optic is required in order to capture the surplus reflected solar radiation coming from the primary reflector. The component in Tonatiuh is composed with only

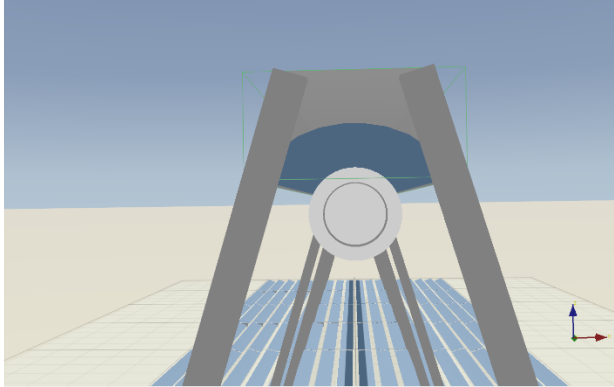


Figure 96: Secondary Reflector Node.

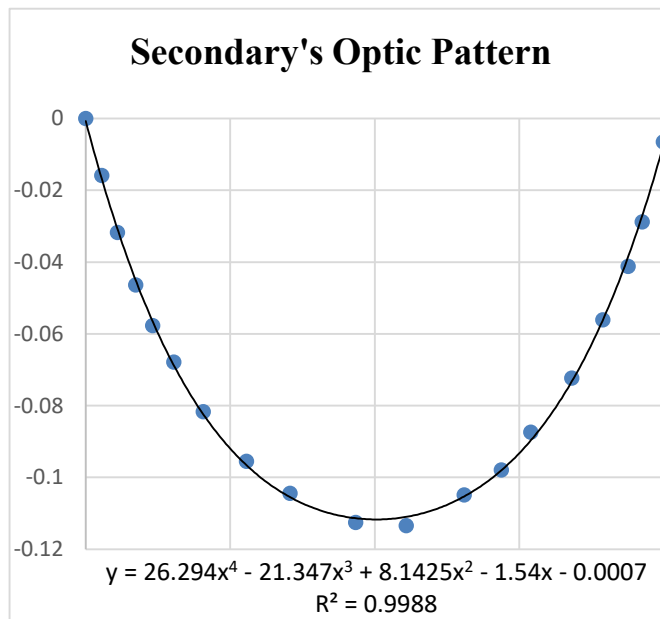


Figure 95: Secondary Optic Pattern with its equation of the fourth order.

account and, with the use of Excel and a pre-processing data phase, the pattern of the mirror is evaluated as shown in the Figure 95. Starting from the definition of the position of the left point of the mirror ([0,0] of the Secondary Optic pattern), it needs to be set, considering the system of the group node of the receiver, with

Secondary_Reflector	
Parameter	Value
▼ transform	
translation	0 0 0
rotation	1 0 0 90
scale	1 1 1

Figure 94: Secondary Reflector Parameters.

the child node “Mirror”, which has a specific shape almost similar to a parabola. Firstly, the parent node “Secondary Reflector” has to be set with a rotation around the x axis in order to express the entire volume in the horizontal plane; therefore, recalling the rotation

of the “Receiver Node”, in this way the axes return with the normal case as visualized in the bottom-right angle of GUI. The mirror is hard to construct because it is not designed with a simple parabola shape but considers the real shape presented in the Cypriot facility. Towards that goal, the different points from the pdf file of that specific shape are taken into

different coordinates in x, y and z. In order to do so, these coordinates compared to the origin of the axes of Receiver are fixed:

Parameter	Value
▼ transform	
translation	-0.20404 -0.0185 0.07265
rotation	1 0 0 180
scale	1 32.544 1

Figure 97: Mirror Parameters.

The first describes the transition into the x axis, evaluated considering the width of lateral edge of the cover, whereas the second defines a transition in the y direction. Therefore, the third value is accounted starting from the height of the Receiver node, defined previously as 4.27541 m. As can be seen, there is a rotation of 180 degrees towards the x axis in order to direct the focus point of the secondary optic towards the absorber. The pattern, previously found using Excel, is set in Tonatiuh in the shape node as in the following figure:




Parameter	Value
▼ shapeRT	 FunctionZ
functionZ	"26.294*x*x*x*x-21.347*x*x*x+8.1..."
dims	100 10
▼ profileRT	 Rectangular
uMin	0
uMax	0.405
vMin	-1
vMax	0
▼ materialRT	 Specular

Figure 98: Mirror Shape.

The equation could be set thanks to the “Function Z” option, where it is possible to fix the borders of the pattern along the x axis with “uMin” and “uMax”.

2.1.5 Cover

The cover is made up of five flat rectangles covering the full length of the facility:

- Top rectangle covering the secondary optic from its upper part for the whole length of the receiver.
- Two rectangles for the eastern and western faces.
- Two for creating the junction between the edges of the bottom of the cover and the secondary optic, at both west and east sides.

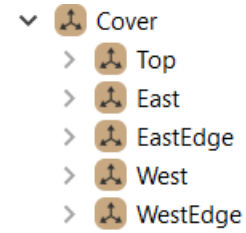


Figure 99: Cover Tree.

Parameter	Value
transform	
translation	0 -0.29347 -0.0185
rotation	1 0 0 90
scale	1 32.581 1

Figure 100: Cover Parameters.

The position of the cover is defined considering as y a value required to cover the first beam (discussed later) and considering a height equal of 0.29347 m above the parent node “Receiver”. They

are put in different positions due to the rotation that is performed in order to keep it in the horizontal plane. The top rectangle (left figure) is defined as a planar shape

Parameter	Value
shapeRT	Planar
profileRT	Rectangular
uMin	-0.15941
uMax	0.15941
vMin	0
vMax	1
materialRT	Absorber

Figure 101: Top Rectangle Shape.

with a rectangular profile with a width of 0.31882 m. For the eastern and western sides, the points used to start their pattern are translated from the initial point of the parent system node with +/-0.15941 m and with a rotation along the y direction with +/- 73.2° respectively. Regarding

their shapes, it is defined in a similar way to the top rectangle taking into account the width.

Parameter	Value
transform	
translation	0.15941 0 0
rotation	0 1 0 73.2
scale	1 1 1

Figure 102: East Rectangle Parameters.




Parameter	Value
shapeRT	 Planar
▼ profileRT	 Rectangular
uMin	0
uMax	0.231362
vMin	0
vMax	1
materialRT	 Absorber

Figure 103: East/West Rectangle Shape.

The eastern and western edge x positions are evaluated starting from the position of the secondary mirror and adding the width of 22.24 mm. In the y direction considering that, the starting point of the mirror is at 4.34806 m and the system of the cover is at 4.56888 m, -0.22082 m must be set. Their shape is evaluated considering a width of 22.24 mm.

Parameter	Value
▼ transform	
translation	0.22628 0 -0.22082
rotation	0 0 1 0
scale	1 1 1

Figure 104: East Edge Parameters.

2.2 Structure

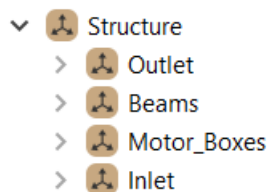


Figure 105: Structure Tree.

The structure node consists of four child nodes representing the inlet tube, outlet tube, beams and motor boxes. Although they are not main components of the facility, in the software design they are very important, because they are source of possible losses, for example in terms of shading or blocking,

and for that reason their construction is fundamental. The “Structure” group node has its origin corresponding to the origin of the system therefore there is no transition or rotation.

2.2.1 Inlet/Outlet tube

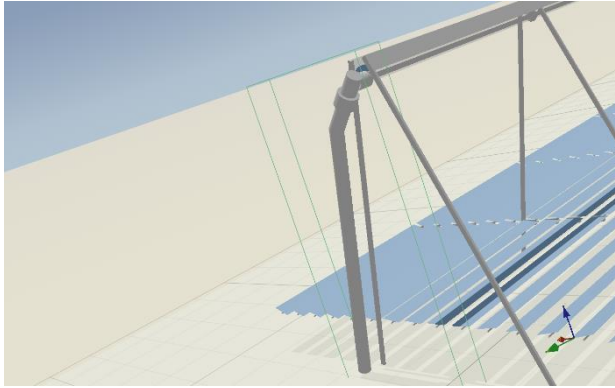


Figure 106: Inlet/Outlet Node.

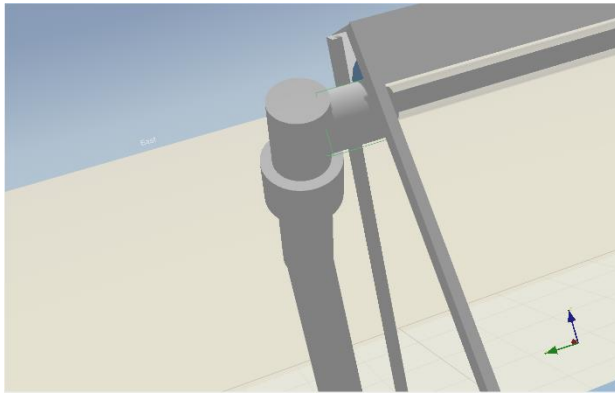


Figure 107: Part1 Node.

The Outlet and Inlet node consists of three child nodes called simply “Part1”, “Part2” and “Part3”. As will be discussed, they are mainly based on cylinders with complex rotations. Part1 consists of a cylinder shape with a box profile with a radius of 0.10663 m and 0.228 m long, and an absorber type material chosen. Because this part must be parallel to the absorber, a vector of rotation is set, as can be seen from its Node parameter view:

Parameter	Value
▼ transform	
translation	0 -0.082 4.27291
rotation	-1 -0 -0 90
scale	0.10663 0.10663 0.228

Figure 108: Part1 Parameters.

As can be seen, there is a very small translation along the y direction. Therefore, considering its shape and material, the Figure on the right explains the choices made. Part2 is more complex. Indeed, its origin (the middle of the cylinder) at first shifts in the x, y and z direction. Then a rotation of 134° is placed around the y

Parameter	Value
▼ shapeRT	Cylinder
caps	none
▼ profileRT	Box
uSize	1
vSize	1
materialRT	Absorber

Figure 109: Part1 Shape.

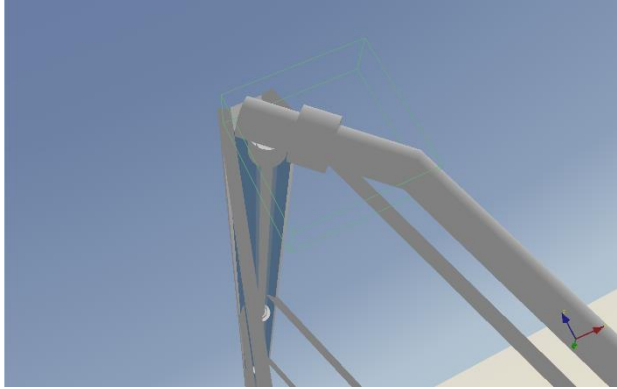


Figure 110: Part2 Node.

Parameter	Value
▼ transform	
translation	-0.1 -0.26 4.37291
rotation	0 1 0 134
scale	1 1 1

Figure 111: Part2 Parameters.

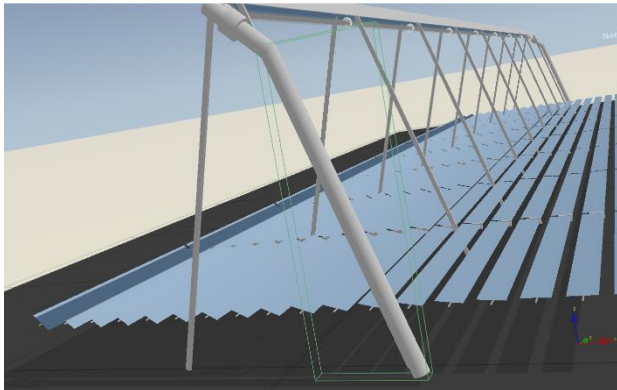


Figure 112: Part3 Node.

direction. The next figures summarize this. The Part2 node is made up of two child nodes: The Main node (the cylinder) and the Flange (near the middle of the cylinder). Considering the cylinder, it must be set at a radius of 0.10663 m and 0.91 m

long, whereas its shape is constructed considering a cylinder shape and a rectangular profile with absorber material and “bottom” selected as caps.

The Flange is constructed like the flanges in the Receiver node considering an absorber material and, in terms of geometrical properties, with a radius of 0.15 m and 0.2 m long. Finally, the Part3 node is needed to complete the Outlet/Inlet parent node. Here a 3.96 m long cylinder shape with a rectangular profile is

constructed with the absorber material. Translation and rotation vectors are introduced for that node as in the following figure.

Parameter	Value
▼ transform	
translation	1.69 -0.26 0
rotation	0 -1 0 16.9639
scale	0.1 0.1 1

Figure 113: Part3 Parameters.

2.2.2 Beams

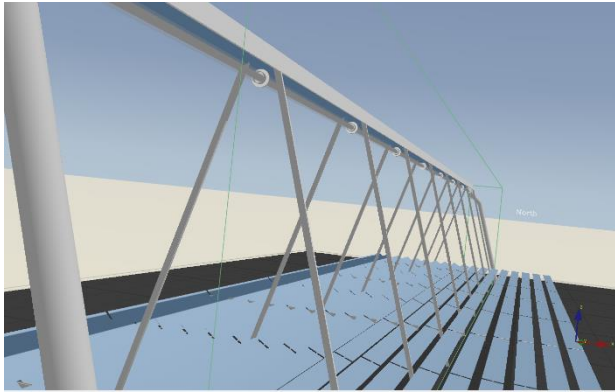


Figure 115: Beams Node.

The beams, needed in real conditions to support the weight of the receiver, are designed in the software by constructing a single one of them and using copy, paste and translating to create the others. There are 18 beams, 9 for both the eastern and

western sides with a shape that is equal for all of them: a Cube shape with a box profile measuring 0.037 m along y and 0.07 m along x. The Beams Node is made up of two nodes for the Eastern and Western sides that differ only in terms of rotation and position in the x direction. Indeed, for the Western side, a rotation of 16.8° around the y direction is fixed and the origin of the child node is placed in the point of junction with the cover, then -0.15941 m and 4.56897 m are defined in the x direction and y direction respectively. For the Eastern Side there are opposite

Parameter	Value
transform	
translation	0.15941 0 4.56897
rotation	-0 -1 -0 16.8
scale	1 1 1

Figure 114: West Beams Node.

values in the x direction and on rotation.

Both the Western and Eastern sides are composed of 8 beams placed in the middle of the space between the different mirrors in the y direction and

-2.385 m in the z direction, considering a half of the 4.77 m length of a single beam, starting from the cover.

2.2.3 Motor Boxes

The Motor Boxes are 72, arranged in rows of 4. The relevant node includes a very simple tree node construction. Indeed, the Boxes are constructed starting from the definition of origin of the group node in the z direction based at 0.67316 m from the ground (it is equal to the height of the mirrors). Its child nodes are the different rows where the x origin for each one is defined considering that the right side of the motor boxes must be set 2 mm away from the mirror. For each row, four motor

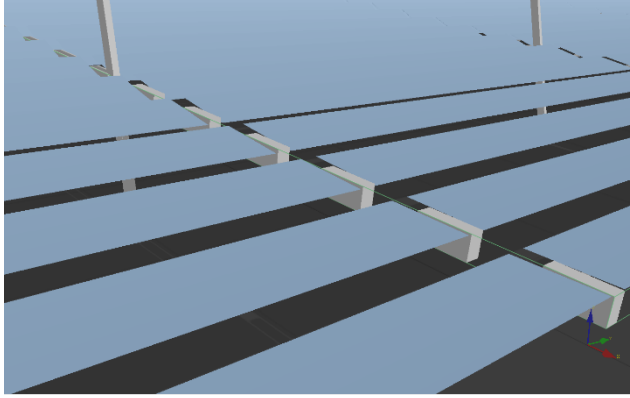


Figure 116: Motor Boxes Node.

boxes are defined with a cube shape and box profile with 0.216 m wide, 0.097 m high and 0.06 m wide. Therefore, considering a single row, every motor box is set 8.136 m away from the previous one in the y direction and corresponding to the centre of the beam.

2.3 Primary Reflector

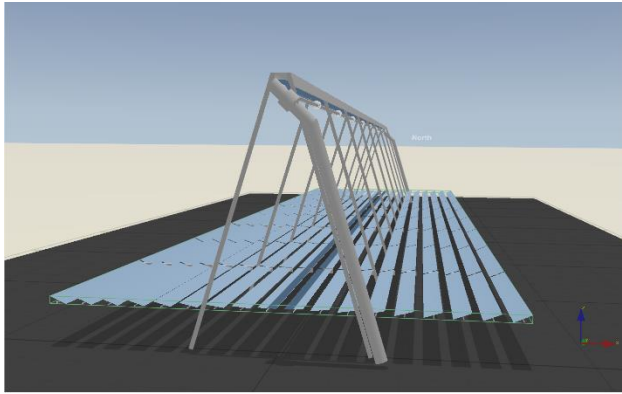


Figure 117: Primary Reflector Node.

It is composed of 18 rows of eight mirrors 4 m long. The positions on the x-axis and y-axis of all the mirrors are set in the “Row_” node and “Mirror_” node respectively. The height of the entire field is defined in the child node “primary” of each group node “Mirror_” at

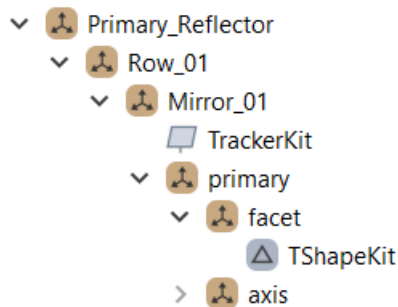


Figure 118: Primary Reflector Tree.

0.67316 m. This height does not correspond to the axis of rotation of the mirrors; in fact, the mirrors are shifted 0.045 m towards the z direction as set in the primary child node “facet”. As discussed before, the “primary” and “Row_” nodes are required in order to define the position in the z and x directions respectively. After the definition of

the position of each mirror in the y direction, a “TrackerKit” is added, where the different properties and characteristics of the tracking movement of the mirror are specified. Indeed, after the selection of the “one-axis” type of tracking, the “primary shift” and “facet shift” are defined at 0.67316 m and 0.045 m in the z direction


Parameter	Value
▼ armature	 one-axis
primaryShift	0 0 0.67316
primaryAxis	0 1 0
primaryAngles	-90 90
facetShift	0 0 0.045
facetNormal	0 0 1
angleDefault	0
▼ target	
aimingFrame	global
aimingPoint	0 0 4.27541

Figure 119: Tracker Setting Parameters.

translation of the “primary” and “facet” nodes are imposed of 0.67316 m and 0.045 m in the z direction respectively. The “facet” node has a shape node in order to define the pattern of the mirrors, which differs from row to row. Indeed, as discussed in the description of an LFR system, the mirrors of different rows are mounted at various distances from the absorber and therefore there is a varied focal length. In order to implement this, a particular shape must be chosen for the mirrors.




Parameter	Value
▼ shapeRT	 Elliptic
aX	10.4
aY	1e+08
aZ	10.4
▼ profileRT	 Rectangular
uMin	-0.16
uMax	0.16
vMin	0
vMax	4
▼ materialRT	 Specular
reflectivity	0.924

Figure 120: Shape Parameters of the mirrors.

respectively. They in turn account for the height of the object and its shift in relation to the axis of rotation. Another important parameter to be modified is the aiming point that must be the position of the receiver; therefore, in this case it is designed at a height of 4.27541 m above the ground level. Considering the values set within tracker node, the values of

The Elliptic shape with a rectangular profile is selected, where the parameters of the equation of the shape are defined in the x and z direction as double the focal length while in the y direction an enormous value is needed to design the flatness of the mirror itself. The material selected is, of course, the specular one, with a reflectivity of 0.924 in order to reflect the solar radiation to the receiver.

After the creation of the first mirror, the other mirrors in the row are created using “copy and paste” and translated 4.068 m away from the previous one, while the other rows are set in the same way after their position has been defined in the x position, being careful to adjust the focal distance of the mirrors, which must obviously vary.

3. *Environment Settings*

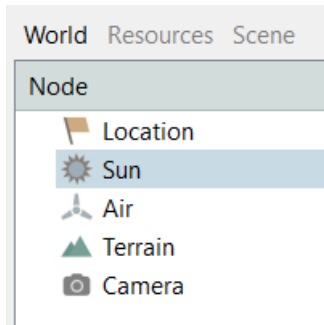


Figure 121: World Tree.

The environment settings are fixed in the “World” menu presented in the upper part of the “Nodes Tree View”.

Here five nodes appear:

- Location, Air, Terrain, Camera: In these nodes it is possible to decide the position of the system, properties of the air, properties of the ground and finally camera options (they are not necessary for our purposes).

- Sun: Here it is possible to define the position of the sun in terms of Azimuth and Elevation, the Irradiance, sun model (in this study the “Pillbox” model is used with a

Parameter	Value
▼ position	
azimuth	90
elevation	90
irradiance	1
▼ shape	
thetaMax	0.00465
▼ aperture	
disabledNodes	"//RootNode/Fresnel_CVI/Ground;//R...

Figure 122: Sun Parameters.

“thetaMax” equal of 0.00465) and, finally it is possible to set the nodes of the plant which would not be targeted by the direct sun rays. All nodes are selected except the mirrors of the primary reflector, so that there are no direct rays lost over the cover, beams, etc.

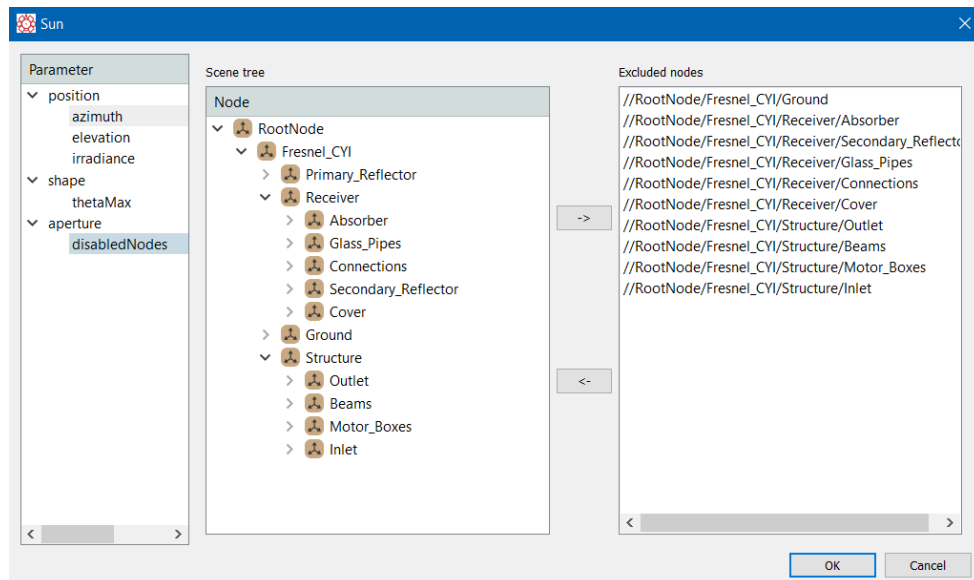


Figure 123: Disabled Nodes.

4. Ray Tracing Simulations

In Toolbar, specifically in “Run”, can be found the “Ray Tracing Analysis”, which offers different tools and settings. Before launching a simulation using its button, different parameters must be set (in Parameters Window and Format Window):

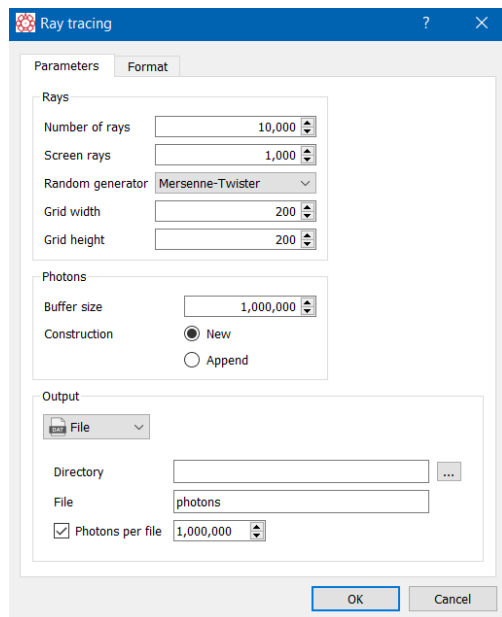


Figure 124: Ray Tracing Setting (1).

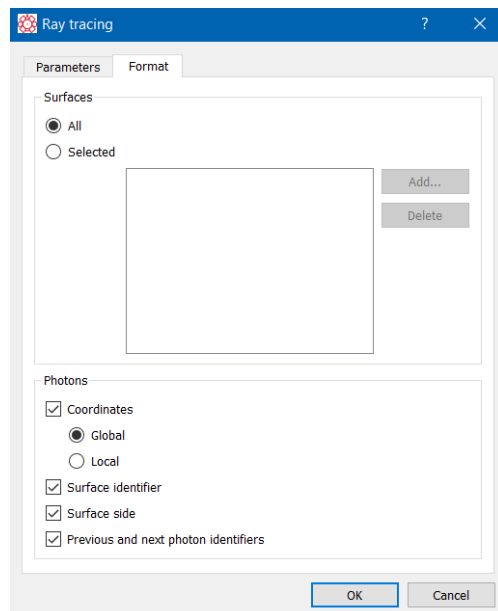


Figure 125: Ray Tracing Setting (2).

- Number of Rays: Setting how many rays have to be tracked during the simulation.
- Screen Rays: Sets the number of rays that could be visualized in the GUI view.
- Random Generator: Here it is possible to define what random generator could be used.
- Grid width/height: These parameters are used in order to decide the dimension of the cells that divide the sun plane from which the solar rays are emitted.
- Output Window: Here it is possible to decide if the results must be exported or not and how this could be done.
- Surfaces Window: it is possible to store the full information or only the information regarding one or more surfaces
- Photons Window: Here it is possible to set what type of information must be included in the export results.

Indeed, the rays will strike various surfaces and for each impact, Tonatiuh could record different data in terms of what

surfaces are hit, on which side, if it is struck by a direct solar photon or by a reflected one. From this point of view, the setting of these properties for the Ray Tracing Analysis is required and fundamental.

5. *Script Tool*

In the “Run” menu, another important option is present for constructing the entire plant. This is the Script tool, where it is possible to write a code to first construct the single components of the facility (Mirrors, Flanges, Glass Pipes, etc.) and finally put them together to construct the macro-parts of the Fresnel (Receiver, Primary Reflector and Structure). All features of the software are present in this menu: designing, setting environmental properties, etc. It permits the use of the common functions for coding, such as the *for*, *if*, *elseif* and *else* loops. From this point of view, the Script tool is another useful pathway to construct the facility. It thus follows that the Script tool and graphical one (described in the paragraph “Description of the design of the Fresnel Facility”) represent two options for achieving the same result. From this point on, the description of the entire script will be made, divided into three parts: i) Definition of position and construction function for each component; ii) Construction of the CYI Fresnel and iii) Scene Settings. The different values present in the script to describe the different components in terms of shape, material, translation, rotation and scale are the same as the values considered for the construction of the facility using the graphical pathway and therefore they are not justified in the following paragraphs.

5.1 Definition of position and construction function for each component

This first part of the script is related to setting the position of the different components, determining the different types of material and defining the functions to construct the different components of the LFR facility. The first two objectives are present in the following part of the script:

```
1 // DEFINITION OF POSITION AND BUILDING FUNCTION FOR EACH COMPONENT //
2
3 //POSITIONS
4 var posX = [-3.900, -3.434, -2.967, -2.501, -2.035, -1.572, -1.114, -0.664, -0.225, 0.225, 0.664, 1.114, 1.572, 2.035, 2.501, 2.967, 3.434, 3.900];
5 var posXM = [-3.845, -3.379, -2.912, -2.446, -1.98, -1.517, -1.059, -0.609, -0.17, 0.28, 0.719, 1.169, 1.627, 2.09, 2.556, 3.022, 3.489, 3.955];
6 var focuses = [5.2, 4.9, 4.8, 4.7, 4.6, 4.5, 4.4, 4.2, 3.9, 4.0, 4.3, 4.4, 4.5, 4.6, 4.7, 4.8, 5.0, 5.5];
7 var posY = [0, 4.068, 8.136, 12.204, 16.272, 20.340, 24.408, 28.476];
8 var flangesY = [0, 4.068, 8.136, 12.204, 16.272, 20.340, 24.408, 28.476, 32.544];
9 var beamsY = [-0.034, 4.034, 8.102, 12.17, 16.238, 20.306, 24.374, 28.442, 32.51];
10
11 //MATERIALS
12 function setMaterialGray(shape)
13 {
14     var mG = shape.getPart("material");
15     mG.setParameter("ambientColor", "0.5 0.5 0.5");
16     mG.setParameter("diffuseColor", "0.3 0.3 0.3");
17     mG.setParameter("specularColor", "0. 0. 0.");
18     mG.setParameter("shininess", "0.1");
19 }
20
21 function setMaterialTransparent(shape)
22 {
23     var mG = shape.getPart("material");
24     mG.setParameter("ambientColor", "0.5 0.5 0.5");
25     mG.setParameter("diffuseColor", "0.3 0.3 0.3");
26     mG.setParameter("specularColor", "0. 0. 0.");
27     mG.setParameter("shininess", "0.1");
28     mG.setParameter("transparency", "0.9");
29 }
```

Figure 126: Position and material script part for CYI LFR facility.

As can be seen, in lines 3 to 9 row vectors are set to establish the position of the different components (such as x position of the mirrors, x position of the motor boxes, y position of the pipes, y position of the flanges and y position of the beams) and the focus length of the mirrors. In lines 11 to 29 two different materials are defined for the absorber and transparent components, setting two different functions, setMaterialGray and setMaterialTransparent respectively. Here different features of the material, such as “ambientColor” or “shininess” are established. Afterwards, (as can be seen in the picture to the left on the next page) the part regarding the construction of the different components concerns the mirrors. This function, called makeFacet, starting from inputs such as the node where it is necessary to construct the mirror and its radius (related to the focus length), is able to build the mirror taking into account its tracking, shape and material. In lines 34 to 43, the tracking movement of the mirror is defined in terms of primary shift, facet shift and aiming point, as discussed in the paragraph regarding the construction of

```

31 //MIRRORS
32 function makeFacet(nodeM, radius)
33 {
34     var t = nodeM.createTracker();
35     var ta = t.insertArmature("one-axis");
36     ta.setParameter("primaryShift", "0 0 0.67316");
37     ta.setParameter("primaryAxis", "0 1 0");
38     ta.setParameter("primaryAngles", "-90 90");
39     ta.setParameter("facetShift", "0 0 0.045");
40     ta.setParameter("facetNormal", "0 0 1");
41     var tt = t.getPart("target");
42     tt.setParameter("aimingFrame", "global");
43     tt.setParameter("aimingPoint", "0 0 4.273");
44
45     var nodeP = nodeM.createNode("primary");
46     var nodeF = nodeP.createNode("facet");
47     nodeF.setParameter("translation", "0 0 0.045");
48     var s = nodeF.createShape();
49     var q = s.insertSurface("Elliptic");
50     q.setParameter("aX", radius);
51     q.setParameter("aY", 1e8);
52     q.setParameter("aZ", radius);
53     var p = s.insertProfile("Rectangular");
54     p.setParameter("uMin", -0.16);
55     p.setParameter("uMax", 0.16);
56     p.setParameter("vMin", 0);
57     p.setParameter("vMax", 4);
58     var m = s.insertMaterial("Specular");
59     m.setParameter("slope", "0.002");
60     m.setParameter("reflectivity", "0.924");
61
62     var nodeA = nodeP.createNode("axis");
63     nodeA.setParameter("rotation", "1 0 0 -90");
64     nodeA.setParameter("scale", "0.01 0.01 1");
65     var s = nodeA.createShape();
66     var q = s.insertSurface("Cylinder");
67     var p = s.insertProfile("Rectangular");
68     p.setParameter("vMin", 0);
69     p.setParameter("vMax", 4);
70     var m = s.insertMaterial("Transparent");
71     setMaterialGray(s);
72 }

```

Figure 127: Mirror Function.

functions in lines 74 to 112, called makeFlange and makePipe respectively. The

```

74 //FLANGES
75 function makeFlange(nodeF)
76 {
77     var node = nodeF.createNode("Seal");
78     node.setParameter("scale", "0.0625 0.0625 0.168");
79     var s = node.createShape();
80     var q = s.insertSurface("Cylinder");
81     setMaterialGray(s);
82
83     node = nodeF.createNode("Outer");
84     node.setParameter("scale", "0.095 0.095 0.024");
85     s = node.createShape();
86     q = s.insertSurface("Cylinder");
87     q.setParameter("caps", "both");
88     setMaterialGray(s);
89 }

```

Figure 128: Flange Function.

constructed considering the same nodes of the graphical one. Therefore, an inner and outer node are required with their scale, shape and material (See the next page for the script regarding the glass pipes).

the mirrors using the graphical pathway, whereas the other parameters are the default ones. In lines 45 to 60, the facet of the mirror is defined by inserting the elliptic surface (taking into account the radius as a value for ax and az dimensions), the rectangular profile (considering 0.32 m width and 4 m length) and as material the specular one with 0.002 of slope and 0.924 of the reflectivity. In lines 62 to 71, the axis of rotation of the mirrors is set, which gives a better visualization of the rotation of the mirror itself.

Following the same structure, the flanges and pipes are set as the flanges function is constructed considering the same structure as the graphical pathway. Therefore, the two nodes required to construct the flanges are necessary: Seal and Outer. For each one the scale and the shape must be set. In the same way, the glass pipes are

```

91 //PIPES
92 function makePipe(nodeP)
93 {
94     var node = nodeP.createNode("Inner");
95     node.setParameter("scale", "0.059 0.059 3.9");
96     var s = node.createShape();
97     var q = s.insertSurface("Cylinder");
98     var m = s.insertMaterial("Fresnel (unpolarized)");
99     m.setParameter("nFront", "1.47");
100     m.setParameter("nBack", "1.");
101     m.setParameter("slope", "0.002");
102     setMaterialTransparent(s);
103
104     node = nodeP.createNode("Outer");
105     node.setParameter("scale", "0.0625 0.0625 3.9");
106     var s = node.createShape();
107     var q = s.insertSurface("Cylinder");
108     var m = s.insertMaterial("Fresnel (unpolarized)");
109     m.setParameter("nFront", "1.");
110     m.setParameter("nBack", "1.47");
111     setMaterialTransparent(s);
112 }

```

Figure 129: Pipe Function.

```

115 function makeOutlet(parent)
116 {
117     var node = parent.createNode("Part1");
118     node.setParameter("translation", "0 -0.082 4.27541");
119     node.setParameter("rotation", "1 0 0 -90");
120     node.setParameter("scale", "0.10663 0.10663 0.228");
121     var s = node.createShape();
122     var q = s.insertSurface("Cylinder");
123     setMaterialGray(s);
124
125     var nodeP = parent.createNode("Part2");
126     nodeP.setParameter("translation", "-0.1 -0.26 4.37591");
127     nodeP.setParameter("rotation", "0 1 0 134");
128
129     var node = nodeP.createNode("Main");
130     node.setParameter("scale", "0.10663 0.10663 1");
131     var s = node.createShape();
132     var q = s.insertSurface("Cylinder");
133     q.setParameter("caps", "bottom");
134     var p = s.insertProfile("Rectangular");
135     p.setParameter("vMin", 0);
136     p.setParameter("vMax", 0.91);
137     setMaterialGray(s);
138
139     var nodeF = nodeP.createNode("Flange");
140     nodeF.setParameter("translation", "0 0 0.385");
141
142     var node = nodeF.createNode("Main");
143     node.setParameter("scale", "0.15 0.15 0.2");
144     var s = node.createShape();
145     var q = s.insertSurface("Cylinder");
146     q.setParameter("caps", "both");
147     setMaterialGray(s);
148
149     var node = parent.createNode("Part3");
150     node.setParameter("translation", "1.69 -0.26 0");
151     node.setParameter("rotation", "0 -1 0 16.9639");
152     node.setParameter("scale", "0.1 0.1 1");
153     var s = node.createShape();
154     var q = s.insertSurface("Cylinder");
155     var p = s.insertProfile("Rectangular");
156     p.setParameter("vMin", 0);
157     p.setParameter("vMax", 3.96);
158     setMaterialGray(s);
159 }

```

Figure 130: Outlet/Inlet Function.

The Outlet Pipe function, called makeOutlet (for the Inlet one, makeInlet) is defined in lines 115 to 159. Here the construction of the pipe is based on three parts with absorber material: Part1, Part2 and Part3. Like for the graphical one, the Part1 (lines 117 to 123) is relied on the construction of a cylinder, whereas the Part2 (lines 125 to 147), as well as rotation and translation vector, is composed of a main cylinder and a flange. Part3 (lines 149 to 159) sets the term of translation, rotation and scaling following the characteristics of how it is constructed in the graphical option. The inlet pipe is defined following the same script but considering different rotation vectors for its parts.

5.2 Construction of the CYI Fresnel

After the construction of the different functions, which, starting from their input (in most of the cases the node where the component is needed), are able to develop the required component, the script continues with the construction of the CYI Fresnel, defining the “nodeFresnel”. This part starts with the construction of motor boxes, inlet, outlet and primary reflector nodes:

```
210 // CONSTRUCTION OF THE CYI FRESNEL //
211
212 tn.Clear();
213 var nodeFresnel = NodeObject();
214 nodeFresnel.setName("Fresnel_CYI");
215
216 //MOTOR BOXES, INLET AND OUTLET NODE
217 var nodeStructure = nodeFresnel.createNode("Structure");
218 var nodeMot = nodeStructure.createNode("Motor_Boxes");
219 nodeMot.setParameter("translation", "0 0 0.67316");
220 var nodeOut = nodeStructure.createNode("Outlet");
221 makeOutlet(nodeOut);
222 var nodeIn = nodeStructure.createNode("Inlet");
223 nodeIn.setParameter("translation", "0 32.54 0");
224 nodeIn.setParameter("rotation", "0 0 1 180");
225 makeInlet(nodeIn);
226
227 //PRIMARYREFLECTOR NODE
228 var nodePR = nodeFresnel.createNode("Primary_Reflector");
229 for (var i = 0; i < posX.length; i++) {
230     var nodeR = nodePR.createNode("Row_" + (i + 1));
231     var nodeRM = nodeMot.createNode("Row_" + (i + 1));
232     nodeR.setParameter("translation", "" + posX[i] + " 0 0");
233     nodeRM.setParameter("translation", "" + posXM[i] + " 0 0");
234     for (var j = 0; j < posY.length; j++) {
235         var nodeM = nodeR.createNode("Mirror_" + (j + 1));
236         nodeM.setParameter("translation", "0 " + posY[j] + " 0");
237         makeFacet(nodeM, 2*focuses[i]);
238         if (j%2 == 0) {
239             var nodeD = nodeRM.createNode("Drive_0" + (j/2 + 1));
240             nodeD.setParameter("translation", "0 " + (posY[j + 1] - 0.034) + " 0");
241             nodeD.setParameter("scale", "0.216 0.060 0.097");
242             var s = nodeD.createShape();
243             var q = s.insertSurface("Cube");
244             setMaterialGray(s); }
245     }
246 }
```

Figure 131: Motor Boxes, Inlet, Outlet and Primary Reflector Node.

Considering that the transition and rotation of the parts of a component have already been inserted in the functions, the component nodes must now be defined in order to fix the position of the entire component. In lines 216 to 225, the Inlet and Outlet Pipe are constructed, starting from the definition of their nodes and finally using their new functions defined in the previous part of the script “makeInlet” and “makeOutput”. In lines 227 to 246, the construction of the primary reflector is a more difficult task because it requires two *for* loops and within this process the motor boxes are also built. Therefore, after the primary reflector node has been defined, the first *for* loop is used to construct the different rows (from 1st to 18th).

After the formation of the nodes for the row of mirrors and row of motor boxes and their positioning by the indices i of the first loop, a second *for* loop is introduced in order to construct the mirrors that compose the specific i^{th} row along the y direction. Care must be taken when describing the inputs of the function `makeFacet` because double the i^{th} focus length must be defined. When the j index is a multiple of two, a motor box is constructed. Therefore, as can be seen, the first loop is used in order to move in the x direction, whereas the second one is used to move towards the y direction, fixing the x one. The receiver node is constructed in lines 248 to 260 line, considering its translation and rotation in relation to the main node “nodeFresnel”.

```

248 //RECEIVER NODE
249 var nodeReceiver = nodeFresnel.createNode("Receiver");
250 nodeReceiver.setParameter("translation", "0 -0.034 4.27541");
251 nodeReceiver.setParameter("rotation", "1 0 0 -90");
252 var nodeA = nodeReceiver.createNode("Absorber");
253 nodeA.setParameter("scale", "0.035 0.035 1");
254 var s = nodeA.createShape();
255 s.setName("Shape");
256 var q = s.insertSurface("Cylinder");
257 var p = s.insertProfile("Rectangular");
258 p.setParameter("vMin", 0);
259 p.setParameter("vMax", 32.544);
260 setMaterialGray(s);

```

Figure 132: Receiver and Absorber Nodes.

Afterwards the node of the absorber is formed as a child node of the “nodeFresnel” and then the different values for scaling the cylinder in three dimensions are introduced. Finally, the

absorber material is set. Two of the Receiver’s child nodes are the Glass Pipes and Connections nodes. These are defined together because a common *for* loop is used. After the Connections and Glass Pipes nodes have been defined as child nodes of the receiver, considering the y position of the flanges defined as a vector at the beginning of the script, the flanges and the glass pipes are created, using the functions “makeFlange” and “makePipe”. Consequently, the positions of the pipe

```

262 //GLASS PIPES and CONNECTIONS NODES
263 var nodeGl = nodeReceiver.createNode("Glass_Pipes");
264 var nodeConn = nodeReceiver.createNode("Connections");
265 for (var j = 0; j < flangesY.length; j++) {
266     var nodeF = nodeConn.createNode("Flange_" + (j + 1));
267     nodeF.setParameter("translation", "0 0 " + flangesY[j]);
268     makeFlange(nodeF);
269     if (j == flangesY.length - 1) continue;
270
271     var nodeP = nodeGl.createNode("Pipe_" + (j + 1));
272     nodeP.setParameter("translation", "0 0 " + (flangesY[j] + 3.9/2 + 0.168/2));
273     makePipe(nodeP);
274 }

```

Figure 133: Glass Pipes and Connections Nodes.

and the flange are correlated.


```

276 //SECONDARY REFLECTOR NODE
277 var nodeSR = nodeReceiver.createNode("Secondary_Reflector");
278 nodeSR.setParameter("rotation", "1 0 0 90");
279 var nodeM = nodeSR.createNode("Mirror");
280 nodeM.setParameter("translation", "-0.20404 -0.0185 0.07265");
281 nodeM.setParameter("rotation", "1 0 0 180");
282 nodeM.setParameter("scale", "1 32.544 1");
283 var s = nodeM.createShape();
284 var q = s.insertSurface("FunctionZ");
285 q.setParameter("functionZ", "\"26.294*x*x*x*x-21.347*x*x*x+8.1425*x*x-1.54*x-0.0007\"");
286 q.setParameter("dims", "10 10");
287 var p = s.insertProfile("Rectangular");
288 p.setParameter("uMin", 0);
289 p.setParameter("uMax", 0.405);
290 p.setParameter("vMin", -1);
291 p.setParameter("vMax", 0);
292 var m = s.insertMaterial("Specular");
293 m.setParameter("slope", "0.002");
294 m.setParameter("reflectivity", "0.883");

```

Figure 135: Secondary Reflector Node.

Another Receiver's child node is the secondary mirror, which is constructed following the dimensions used for its graphical construction. After the creation of the node as a child node of the receiver, a vector of rotation is required. The mirror node is then created taking into account its position in relation to the receiver node. As discussed in the graphical construction, the "Function Z" property is used to fix the shape of the mirror, according to the equation performed in Excel. Finally, the material Specular is used for that component. The cover node is another important

```

296 //COVER NODE
297 var nodeC = nodeReceiver.createNode("Cover");
298 nodeC.setParameter("translation", "0 -0.29347 -0.0185");
299 nodeC.setParameter("rotation", "1 0 0 90");
300 nodeC.setParameter("scale", "1 32.581 1");
301 node = nodeC.createNode("Top");
302 s = node.createShape();
303 p = s.insertProfile("Rectangular");
304 p.setParameter("uMin", -0.15941);
305 p.setParameter("uMax", 0.15941);
306 p.setParameter("vMin", 0);
307 p.setParameter("vMax", 1);
308 setMaterialGray(s);
309 node = nodeC.createNode("East");
310 node.setParameter("translation", "0.15941 0 0");
311 node.setParameter("rotation", "0 1 0 73.2");
312 s = node.createShape();
313 p = s.insertProfile("Rectangular");
314 p.setParameter("uMin", 0);
315 p.setParameter("uMax", 0.231362);
316 p.setParameter("vMin", 0);
317 p.setParameter("vMax", 1);
318 setMaterialGray(s);
319 node = nodeC.createNode("EastEdge");
320 node.setParameter("translation", "0.22628 0 -0.22082");
321 s = node.createShape();
322 p = s.insertProfile("Rectangular");
323 p.setParameter("uMin", -0.02224);
324 p.setParameter("uMax", 0);
325 p.setParameter("vMin", 0);
326 p.setParameter("vMax", 1);
327 setMaterialGray(s);

```

Figure 134: Cover Node.

child node of the receiver.

First, the cover node is created, fixing its position and rotation. Afterwards its child nodes are created as "Top", "East", "East Edge", "West" and "West Edge". As in the cases of the previous components, these nodes are characterized in terms of their position, rotation and shape. The "West" and "West Edge" are constructed in the same way as the "East" and "East Edge" as can be easily read in

the following script:

```
328 node = nodeC.createNode("West");
329 node.setParameter("translation", "-0.15941 0 0");
330 node.setParameter("rotation", "0 1 0 -73.2");
331 s = node.createShape();
332 p = s.insertProfile("Rectangular");
333 p.setParameter("uMin", -0.231362);
334 p.setParameter("uMax", 0);
335 p.setParameter("vMin", 0);
336 p.setParameter("vMax", 1);
337 setMaterialGray(s);
338 node = nodeC.createNode("WestEdge");
339 node.setParameter("translation", "-0.22628 0 -0.22082");
340 s = node.createShape();
341 p = s.insertProfile("Rectangular");
342 p.setParameter("uMin", 0);
343 p.setParameter("uMax", 0.02224);
344 p.setParameter("vMin", 0);
345 p.setParameter("vMax", 1);
346 setMaterialGray(s);
```

Figure 136: West and West Edge Nodes.

```
348 //BEAMS NODE
349 var nodeBeams = nodeStructure.createNode("Beams");
350 var nodeBE = nodeBeams.createNode("East");
351 nodeBE.setParameter("translation", "0.15941 0 4.56897");
352 nodeBE.setParameter("rotation", "0 1 0 -16.8");
353 var nodeBW = nodeBeams.createNode("West");
354 nodeBW.setParameter("translation", "-0.15941 0 4.56897");
355 nodeBW.setParameter("rotation", "0 1 0 16.8");
356 for (var j = 0; j < beamsY.length; j++) {
357     var nodeB = nodeBE.createNode("Beam_0" + j);
358     nodeB.setParameter("translation", "-0.035 " + beamsY[j] + " -2.385");
359     nodeB.setParameter("scale", "0.070 0.037 4.770");
360     var s = nodeB.createShape();
361     var q = s.insertSurface("Cube");
362     setMaterialGray(s);
363     var nodeB = nodeBW.createNode("Beam_0" + j);
364     nodeB.setParameter("translation", "0.035 " + beamsY[j] + " -2.385");
365     nodeB.setParameter("scale", "0.07 0.037 4.77");
366     var s = nodeB.createShape();
367     var q = s.insertSurface("Cube");
368     setMaterialGray(s);
369 }
```

Figure 137: Beams Node.

The last node is the Beams Node, divided into the construction of the East and West Beams child nodes. The different beams are created within a *for* loop working with the vector along the y direction which is defined at the

beginning of the script. Their different characteristics are inserted within the loop.

5.3 Scene Settings

At the end of the script, after the creation of the ground node (not important for our study), the different scene settings are established. The azimuth and elevation angles are defined, and it is possible to disable the nodes which must not be struck by direct solar photons. Finally, the script ends with the construction of the grid in x and y for the ground.

6. *Matlab Scripts*

This paragraph presents and explains the different Matlab scripts and functions used during the work up to this thesis activity to determine the IAM distribution (already discussed in 6.3 *Matlab Processing*), in order to illustrate the energy collectable by LFR over the days of a year compared to the DNI available and to represent the distribution of the DNI during a day or a year. For the first two purposes, a single script was used, and from here on it will be called the “DNI_Energy_YearlyPlot”.

6.1 *DNI Energy Yearly Plot*

To appropriately explain the script developed in Matlab for the purposes described above, it has been divided into five different parts: i) Distribution of the IAM; ii) Relation between Julian Days and DNI; iii) Relation between Julian Days and IAM; iv) Daily and Yearly Energy Analysis of the LFR facility; and v) Daily Average Energy Analysis by Month of the LFR facility. After running this script, the different graphs in Chapters 5 and 6 were plotted.

6.1.1 *Distribution of the IAM*

The following part of the script is used in order to find the IAM distribution with the longitudinal and transversal angles, starting from real data acquired by the Tonatiuh processing:

```
%% Distribution of the IAM.
% Reading of Excel File of the Results
filename = 'IAM_Results____.xls'; %Put the name of the Excel File where the
results of IAM are present.
M=xlsread(filename);
n=length(M);
eta0=M(1,3); %Optical efficiency at zenith
M=M(2:n,:);
% Conversion of the Azimuth and Elevation into Longitudinal and Transversal Angles
and Pre-Allocation in vectors.
x = (atand(cosd(M(:,2)).*cosd(M(:,1))./sind(M(:,2))))); %Theta_L
y = (atand(cosd(M(:,2)).*sind(M(:,1))./sind(M(:,2))))); %Theta_T
z=M(:,3); %IAM
% Definition of the matrix with a Pre-Processing Data phase.
h=[x y z];
h =h( ~any( isnan( h ) | isinf( h ), 2 ),: );
[C,ia,ic]=unique(h(:,1:2),'rows');
h =h(ia,:);
x=h(:,1);
y=h(:,2);
z=h(:,3);
% Definition of the function from the data acquired that correlate the
% angles Theta L and Theta T with the IAMs values.
F = scatteredInterpolant(x,y,z);
```

As discussed in the *6.3 Matlab Processing* paragraph, after reading the Excel file, which presents the results of the Ray Tracing analysis carried by Tonatiuh, the conversion of the azimuth and elevation angles is obtained. With the results of this transformation and the vector of the corresponding IAM, a matrix h is formed and cleaned by Inf, Nan and repeated values. The end of this part is reached when the scatterdInterpolant function is used to determine the relation between the angles (at longitudinal and transversal planes) and the IAMs.

6.1.2 Relation between Julian Days and DNI

The next part of the script is used in order to evaluate the relation between the Julian Days (JD), defined as the continuous count of days (and in our case fraction of days) since the beginning of the Julian Period, and DNI. It is required because the real data from the pyreliometer are incomplete, indeed some seconds (which in certain cases could amount to 1 or 2 minutes) over the total year are missing. Therefore, from the real data a function which correlates JD with DNI is required in order to obtain graphs with complete data. Here is the relevant script:

```
%% %%%%%%%%% Relation between Julian Days and DNI
%% %%%%%%%%%
%% Start the Process
load('DNI_Data_20191231.mat');
%% Import Data in Vectors.
YY= DNI_Data_stored.Year;
MM= DNI_Data_stored.Month;
DD= DNI_Data_stored.Day;
HH= DNI_Data_stored.Hour;
mm= DNI_Data_stored.Minutes;
ss= DNI_Data_stored.Seconds;
DNI=DNI_Data_stored.DNI;
T=[YY MM DD HH mm ss DNI]; %Creation of the matrix.
n=length(YY);
T=unique(T,'rows'); %Delete of identical rows.
K=T(:,1:6);
K = unique(K, 'rows');
DNI=T(:,7);
daysstudied=n/86400;
JD=JulDay(T(:,1:6)); %Conversion in Julian Days
temp = [JD,DNI];
[C,ia,ic] = unique(temp(:,1), 'rows');
temp = temp(ia,:);
JD = temp(:,1);
DNI = temp(:,2);
f = @(z) interp1(JD,DNI,z);
% Definition of the function from the data acquired that correlate
the
% Julian Days with the DNI values.
```

In the first rows, after the loading of the DNI values collected for each second in an entire year, a matrix was constructed with columns indicating the year, month, hour, second of collection and the corresponding DNI measured. After cleaning the repeated time instances of collection, the conversion of a date (specified by the columns that go from the 1st to 6th of the matrix) into a JD value is performed using the “JulDay” function, which is represented in the next script:

```
function [Val1] = JulDay(X)
DD      = X(:,3);
MM      = X(:,2);
YY      = X(:,1);
Hour    = X(:,4);
mm      = X(:,5);
ss      = X(:,6);
%Parameters for the location
Time_zone = 2;
longitude = 33.3808155;
latitude  = 35.1408573;
hh        = Hour - Time_zone;
%%%%%%%%%%%%%%%%%%%%%%%%%%%%%%%%%%%%%%%%%%%%%%%%%%%%%%%%%%%%%%%%%%%%%%%%%%%%%%
%%%%%%%%%%%%%%%%%%%%%%%%%%%%%%%%%%%%%%%%%%%%%%%%%%%%%%%%%%%%%%%%%%%%%%%%%%%%%% Julian Day / Century calculation
a = floor((14-MM)/12);
y = YY + 4800 - a;
m = MM + 12*a - 3;
Julian_Day_Number = DD + floor((153.*m+2)/5) + 365.*y +
floor(y/4) - floor(y/100) + floor(y/400) - 32045;
Julian_Day = Julian_Day_Number + (hh-12)/24 +
mm/(24*60) + ss/(24*60*60);
Val1 = Julian_Day;
End
```

This function was constructed considering the NOAA Methodology Sun Calculator [42]. The date was first defined as inputs and Time zone, Longitude and Latitude of the place of study (in this case Nicosia, Cyprus). After the conversion into JD and the cleaning process, the function f connecting the JD and the DNI was then found via the function “interp1”.

6.1.3 Relation between Julian Day and IAM.

To achieve the aim of this part it is necessary to define the function that expresses the connection between the instance of time of collection and the corresponding IAM evaluated at the facility. This is described below:

```

%% %%%%%%%%% Relations between Julian Days and IAM
%%%%%%%%%%%%
%% Starting the conversion into Azimuth and Elevation Angles.
Angles=Solar_position(K); %The first Coloumn is referred to the
Azimuth, whereas the other one to the Elevation
%% Creation of the Matrix defined by the three coloumns vectors
cointaining Elevation, Azimuth and corresponding DNI
R=[Angles DNI];
R(:,1)=abs(R(:,1));
%% Step for Azimuth Angles higher than 90 degrees from the South
indx1=find(R(:,1)>90);
R(indx1,1)=180-R(indx1,1);
%% Definition of Theta_L and Theta_T and Corresponding IAM with
the use of the Function F
x = (atand(cosd(R(:,2)).*cosd(R(:,1))./sind(R(:,2)))));
%Theta_L
y = (atand(cosd(R(:,2)).*sind(R(:,1))./sind(R(:,2)))));
%Theta_T
L=[x y];
IAM = F(x,y);
g = @(z) interp1(JD,IAM,z);
% Definition of the function from the data acquired that correlate
the
% Julian Days with the IAM values.
L=[L IAM];

```

Firstly, the time of collection is converted into solar angles in terms of azimuth and elevation using the “Solar_Position” function created considering the NOAA Methodology Sun Calculator [42]. Elevation angles presenting a negative value are substituted by zero because they represent night times. Considering that the IAM function F found with scatterInterpolant has as its domain $0-90^\circ$ from the South for the Azimuth, steps to refer the angles into that domain? are required. This is the reason for the use of the “abs” function for Azimuth angles lower than 0° from the South and of the next conversion step for Azimuth angles higher than 90° from the South. In this way, as used in the previous “Distribution of the IAM” part, the transition into longitudinal and transversal angles from azimuth and elevation angles is performed. At this point, the function F must be found before it is possible to find the IAM values for the different angles, and therefore for the positions of the sun during the whole year. Then, after assessing the different IAMs corresponding to the different JD values (and consequently different time and solar positions), the function g linking the IAMs and JDs can be found with the well-known “interp1”.

6.1.4 Daily and Yearly Energy Analysis of the LFR facility

Starting from the functions g and f obtained as above and passing on to the definition of a vector of Julian Day values independent of the real data collected on the basis of the first second in time of the year and its last one, an analysis of the energy concentrated towards the absorber on a daily and annual basis can be performed:

```
% Daily and Yearly Energy Analysis of the LFR facility
a=JulDay([2019 1 1 0 0 0]); %First second of the year
b=JulDay([2019 12 31 23 59 59]); %Last second of the year
x=[a:1/3600/24:b];
SolarPower = f(x)./1000;
IAMappr = g(x);
En=IAMappr.*(SolarPower*eta0/86400*24); %From Power to Energy
Energy_collectedYear=sum(En); %Total energy collected in the year
N=length(SolarPower);
seglen=N/365;
sN=reshape(SolarPower,seglen,365);
avg=mean(sN);
SolarEnergyDay=avg*24/1000;
SolarEnergyYear=sum(SolarEnergyDay);
check1=sum(SolarEnergyDay)/sum(DNI/86400*24/1000);
BB=reshape(En,seglen,365);
EnergyCollectedbyDay=sum(BB);
% Plot Energy Collected by Day and Solar Energy by Day
N=[1:1:365]; %you can input any other number,The day in question
is the 'N'th day of the year
Dt=datetime('1-Jan-2019')+N-1; % This code will give the date of
the 'N'th day.
figure(1)
bar(Dt,SolarEnergyDay,'r');
hold on
bar(Dt,EnergyCollectedbyDay,'b')
ylabel('Solar Energy (kWh/m^2)');
ylim=[0 12];
ylim(ylim)
xlabel('Time')
grid on
legend('DNI by Day','Collected DNI by LFR by Day')
```

Through the functions f and g it is possible to evaluate the solar power expressed in kW/m^2 and the IAM respectively, since the same vector x is based on the JD values of the seconds which formed the year 2019. The amount of energy collected every second (i -th) of the year is obtained from the next formula which considers the daily average power of DNI multiplied by the hours in a day:

$$E_{i-th} = IAM_{i-th} * \eta_0 * \left(\frac{DNI_{i-th} * 24}{86400} \right)$$

Evaluating the sum of the vector calculated in this way, the yearly energy collected is found. With a simple function of data management such as “reshape” and “avg”, the calculation of the solar energy available by day was performed and, therefore with its sum, the yearly one is evaluated. In the same way the quantity of daily energy collected is assessed. (Afterwards, the different plotting options were used to obtain the graphs presented in Chapters 5 and 6).

6.1.5 Daily Average Energy Analysis by Month of the LFR facility

Following the evaluation of the amounts of monthly solar energy available and collected (through a for loop), the daily average energies are analysed dividing the monthly energy vectors by the number of days of each vector:

```
%% Daily Average Energy Analysis by Month of the LFR facility
v=[31 28 31 30 31 30 31 31 30 31 30 31];
s0=1;
SolarEnergyMonth=zeros(1,12);
EnergyCollectedbyMonth=zeros(1,12);
for j=1:12
    s=s0+v(j)-1;
    SolarEnergyMonth(j)=sum(SolarEnergyDay(s0:1:s));
    EnergyCollectedbyMonth(j)=sum(EnergyCollectedbyDay(s0:1:s));
    s0=s+1;
end
% Plot Daily Average Energy Collected by Month and Daily Average
Solar Energy by Month
figure(2)
SolEnMonthDaily=SolarEnergyMonth./v;
EnCollMonthDaily=EnergyCollectedbyMonth./v;
yyaxis left
bar(SolEnMonthDaily,'r')
hold on
bar(EnCollMonthDaily,'b')
limity=[0 10];
ylim(limity)
ylabel('Solar Energy (kWh/m^2/day)')
ETA=EnCollMonthDaily./SolEnMonthDaily;
yyaxis right
plot(ETA,'g--o','LineWidth',2)
limity=[0 0.9];
ylim(limity)
ylabel('Optical Efficiency')
xticklabels({'Jan','Feb','Mar','Apr','May','Jun','Jul','Aug','Sep',
'Oct','Nov','Dec'})
xlabel('Year 2019')
limits=[0.5 12.5];
xlim(limits)
legend('Daily Average by Month','Daily Average by Month
corrected','Optical Efficiency')
grid minor
```


At the same time, the optical efficiency of the LFR is examined and can be plotted over the months.

6.2 *DNI Power Plot*

After the data from the pyrheliometer have been factored in, with this script it is possible to represent the distribution of the DNI during a specific day (here the Summer Solstice is chosen):

```
%% Start the Process
load('DNI_Data_20191231.mat');
%% Import Data in Vectors.
YY= DNI_Data_stored.Year;
MM= DNI_Data_stored.Month;
DD= DNI_Data_stored.Day;
HH= DNI_Data_stored.Hour;
mm= DNI_Data_stored.Minutes;
ss= DNI_Data_stored.Seconds;
DNI=DNI_Data_stored.DNI;
T=[YY MM DD HH mm ss DNI];
K=T(:,1:6);
% Plot DNI during a specific day
m=find(T(:,1)==2019 & T(:,2)==6 & T(:,3)==21);
x=T(m,1:6);
y=T(m,7);
t=datetime(x);
time_datetime=datetime(t,'ConvertFrom','datetime');
figure(1)
plot(time_datetime,y);
ylabel('DNI (W/m^2)');
xlabel('Time')
z=[0 1000];
ylim(z)
grid on
title('DNI plotted during the Summer Solstice day')
```

Ringraziamenti

Questo lungo percorso universitario sta per concludersi. Ancora ricordo il primo giorno di università a Palermo quando tutti i professori spiegavano il lungo e difficoltoso cammino che ci attendeva ed io già temevo di aver fatto la scelta sbagliata. Invece, nonostante il grande pessimismo che avevo, posso dire di avercela fatta! Sono andato oltre le mie previsioni e questo non è stata solo farina del mio sacco. Se sono riuscito ad arrivare qui, è perché accanto a me ci sono state persone che mi hanno saputo sopportare e supportare.

Il primo ringraziamento va fatto a tutti i professori sia della Laurea Triennale, svolta presso l'Università degli Studi di Palermo, sia della Laurea Magistrale, svolta presso il Politecnico di Torino. Un ringraziamento speciale va al Professore Massimo Santarelli che è stato fin dal primo incontro disponibile per lo svolgimento della tesi, nonostante la situazione emergenziale dovuta al Covid 19 e la lontananza dovuta allo svolgimento della tesi a Cipro.

Ringrazio Fabio Maria Montagnino che mi ha permesso di far parte della grande famiglia della “The Cyprus Institute” e che fin dal mio arrivo a Cipro mi ha aiutato nella vita dentro e fuori l'azienda. Ringrazio di cuore Alaric per i due mesi e mezzo passati insieme in cui grazie ai suoi consigli sono cresciuto a livello professionale.

Un ringraziamento speciale va alla mia coinquilina Alessia, con la quale ho iniziato questo percorso universitario. Grazie di essermi stata vicino quando ne avevo di bisogno! Un ringraziamento speciale va “Giustamente..” anche a Vale che per me è una sorella!

Ringrazio Vincenzo che ormai non è più un amico ma un “fratello”. Grazie di tutti quei momenti passati insieme soprattutto a Torino quando tutto sembrava difficile c'eri tu che mi sostenevi e che credevi in me! Grazie anche di avermi fatto ambientare subito nella nuova vita torinese! Ora aspetto te!

Ringrazio Leo, Giovanni, Giorgio, Domenico e Gioacchino che da sempre sono miei fratelli. Nonostante la distanza, ci siamo sempre confrontati a vicenda e non ci

siamo mai perduti di vista anche se detto sinceramente mi mancava bere qualche birretta con voi. Come posso dimenticare i grandissimi Dario T., Dario G., Alessandro, Biagio e Nicola.

Ringrazio Angela che verso la fine di questo percorso universitario mi ha aiutato e supportato in vista della mia esperienza a Cipro che vedevo con ansia e paura.

Ringrazio Peppe De Luca di tutte quelle passeggiate pre-Esame in cui ci giravamo tutto il centro di Torino. Chi se le dimenticherà? Quando vuoi, possiamo rimetterci a fare l'Hazop Analysis a terra davanti il televisore!

Ringrazio di cuore Francesco De Simone per tutte le mozzarelle e sfogliatelle napoletane che mi ha fatto mangiare! Lo ringrazio soprattutto per le *Noches Locas* in quel di Tarragona! Ricordati di metterti la cintura!

Ringrazio Miriana e Cristiano per tutti quei pomeriggi passati per i vari progetti. Senza di voi poteva essere molto noioso! Cri allenati a Fifa che ancora non sei arrivato a battermi seriamente!

Grazie di cuore a tutti i ragazzi di "Energy fighetti" che sono stati fantastici in questi due anni torinesi e per le fantastiche serate passate assieme. Un ringraziamento speciale va a Mariacarla e Davide Coraci. Non posso non ringraziare *Aka Lanz* e Bobbi per tutte quelle serate passate insieme nei vari locali torinesi; spero alla fine di questa pandemia di passare serate come quelle.

Ringrazio con tutto me stesso i miei genitori che hanno reso possibile questo mio traguardo. Questo risultato è tutto merito vostro. Mamma grazie per tutto l'amore che manifesti ogni secondo nei miei confronti! Penso che senza le tue prelibatezze culinarie non ce l'avrei fatta! Babbo grazie di avermi messo sempre i piedi per terra mostrandomi sempre la difficoltà dell'ostacolo che dovevo superare! Ovviamente ti ringrazio per tutti quei momenti passati a distanza tra tristezza e felicità a guardare il nostro amato Palermo!

Un ringraziamento speciale va a tutti i miei zii vicini e lontani e in particolare mio zio Marcello! Frequentavo la prima media quando per la prima volta sono venuto da te in ufficio perché non capivo il *Minimo Comune Multiplo*. E' merito tuo se ho amato la Matematica! Non dimenticherò mai la tua frase "Tanto già lo sapevo" ogni

volta che ti chiamavo per i 9/10 che prendevo nei compiti di matematica ai tempi del Liceo preparati assieme. GRAZIE!

Ringrazio i miei nonni che da lassù mi hanno sempre accompagnato in questa fantastica avventura!

Buon Futuro Lavoro a me!